DETECTING SILICON MONOXIDE IN THE ATMOSPHERE OF ULTRA–HOT JUPITER WASP-178B

DINGDING (ESTHER) WANG

A THESIS SUBMITTED TO
THE FACULTY OF GRADUATE STUDIES
IN PARTIAL FULFILMENT OF THE REQUIREMENTS
FOR THE DEGREE OF
MASTER OF SCIENCE

GRADUATE PROGRAM IN PHYSICS AND ASTRONOMY
YORK UNIVERSITY
TORONTO, ONTARIO

May 2025

ABSTRACT

Ultra-hot Jupiters (UHJs) host unique atmospheric chemistry where refractory species remain gaseous. WASP-178b ($T_{\rm eq} \sim 2470 \pm 60$ K) is a UHJ that exhibits strong near-ultraviolet absorption (0.2–0.28 μm) previously attributed to silicon monoxide (SiO), though direct detection remained elusive. We present the first spectroscopic detection of gaseous SiO in an exoplanet atmosphere through re-analysis of archival HST/STIS E230M observations. Using an in-band/out-of-band technique with theoretical SiO templates from the ExoMol SiOUVenIR line list, we detect excess absorption of $0.647 \pm 0.148\%$ at $> 4.3\sigma$ significance ($p = 7.6 \times 10^{-6}$). This confirms SiO remains in the gas phase at these extreme temperatures, constraining the silicate cloud condensation threshold. Our detection methodology provides a framework for systematic SiO searches across the UHJ population, enabling comparative studies of silicon chemistry and thermal structure in these extreme atmospheres.

ACKNOWLEDGMENTS

So many people made this thesis happen, and I owe them big time.

First up, to my thesis supervisor, Prof. Sarah Rugheimer — you took a gamble on me 2 years ago, and somehow turned me into someone who actually knows what they're talking about (most of the time). You didn't just teach me about exoplanets, but also made sure I remembered to go outside, workout regularly, and be a human being too! Working with you has been the best part of this whole experience.

I am equally grateful to my co-supervisor, Prof. Jason Dittmann from the University of Florida. Thank you for your comprehensive guidance on the technical aspects of my thesis and for your invaluable advice during my PhD application process. You definitely kept this project from going completely off the rails.

To my York crew at office 336 — June, Elisa, and Kevin, you guys made grad school actually fun! Whether we were nerding out about our research or just surviving together, you made everything better. Thanks for all the random conversations that kept me sane.

To my family back home in China, thank you for supporting me through this whole space adventure without really knowing what the heck I'm actually doing up here. You might not get all the technical stuff about SiO and ultra-hot Jupiters, but honestly, this thesis is yours as much as mine. Thanks for believing in my weird dream of studying the wildest planets we'll never visit.

Haze and Haku — you two deserve medals for putting up with me through this whole thing! Haze, you've listened to more rants about atmospheric chemistry than any reasonable person should have to. And Haku, thanks for being the fluffiest mental support & stress relief a grad student could ask for. You both kept me grounded when I was getting too lost in the stars.

Here's to everyone who made this wild ride possible. Couldn't have done it without you.

TABLE OF CONTENTS

Abstract **ii**

Acknowledgments **iii**

TABLE OF CONTENTS **iv**

List of Tables **vii**

List of Figures **viii**

1 Introduction **1**
- 1.1 Background and Theoretical Framework . . . 1
  - 1.1.1 Fundamentals of Transmission Spectroscopy . . . 3
  - 1.1.2 Wavelength-Dependent Atmospheric Signatures . . . 6
  - 1.1.3 Current and Planned Observational Facilities . . . 10
- 1.2 Atmospheric Chemistry and Thermal Structure of Hot Jupiters . . . 15
  - 1.2.1 Key Discoveries in Atmospheric Composition . . . 15
  - 1.2.2 Temperature Variations in Hot Jupiter Atmospheres . . . 17
- 1.3 Ultra-Hot Jupiter WASP-178b . . . 21
  - 1.3.1 Properties of WASP-178b and its Host Star . . . 21
  - 1.3.2 Summary of Observational Campaigns . . . 23
- 1.4 The Role of Silicon Monoxide in Ultra-hot Jupiter Atmospheres . . . 27
  - 1.4.1 Theoretical Significance of SiO in Ultra-hot Jupiter Atmospheres . . . 27
  - 1.4.2 Observational Detections of Refractory Species . . . 28
  - 1.4.3 Challenges in Detecting SiO . . . 30
  - 1.4.4 Exomol SiOUVenIR Line List . . . 31
- 1.5 Scientific Motivation and Research Objectives . . . 33
  - 1.5.1 Current Gaps in Existing Research . . . 33
  - 1.5.2 Research Objectives . . . 34
- 1.6 Thesis Structure and Overview . . . 35

2 Observation and Data Reduction **36**
- 2.1 Observational Data for WASP-178b . . . 36
- 2.2 Systematics correction . . . 38
  - 2.2.1 Jitter Decorrelation . . . 38
  - 2.2.2 White Light Curve Fitting . . . 44
  - 2.2.3 Spectroscopic light curve fitting . . . 46

3 Detecting SiO in Transmission Spectra **49**
- 3.1 Identifying SiO Peak Absorption Features from Line List . . . 49
- 3.2 In-band/Out-of-band Technique from Grant et al. (2023) . . . 51
  - 3.2.1 Overview of Methodology . . . 51
  - 3.2.2 Technique Adaptation to HST/STIS NUV data . . . 54

4 Analysis and Results 57
4.1 Transmission Spectrum of WASP-178b . . . 57
4.1.1 Broadband and Narrowband Analysis . . . 57
4.1.2 Native Resolution Analysis (0.1 Å bin) . . . 57
4.2 Detection and Characterization of SiO Feature . . . 60
4.2.1 Sensitivity Test for Thresholds . . . 62

5 Discussion 66
5.1 Implications of SiO Detection . . . 66
5.2 Limitations and Potential Sources of Error . . . 67
5.3 Application of Methods to Other Ultra-hot Jupiters . . . 68

6 Conclusion and Future Work 70

A Planet Formation Context 72
A.1 Comparison of Gas Giant and Terrestrial Planet Formation . . . 72
A.2 Formation Pathways of Hot Jupiters . . . 72
A.3 The Snow Line and Planetary Composition (C/O Ratios) . . . 74
A.4 Challenges in Measuring Exoplanetary C/O Ratios . . . 76

B Spectral Diagnostics and Atmospheric Radiative Transfer 78
B.1 Absorption vs. Emission Spectra . . . 78
B.2 Molecular Absorption Cross-Sections and Line Broadening . . . 78
B.3 Radiative Transfer in a Stratified Atmosphere . . . 79
B.4 Thermal Inversion and Spectral Signatures . . . 80

C Brown Dwarfs and Giant Exoplanets 82
C.1 Cooling and Evolution of Brown Dwarfs . . . 83
C.2 Comparative Atmospheric Insights from Brown Dwarfs for Exoplanet Studies . . . 84

D Broadband and Narrowband Spectral Analysis 86
D.1 Broadband Analysis (200 Å Bins) . . . 86
D.2 Narrowband Analysis (4 Å Bins) . . . 87

E HST/STIS Data Reduction Procedures 89

F ExoCross Implementation 91

G Glossary 93
G.1 Exoplanet Terminology . . . 93
G.2 Atmospheric Chemistry and Physics . . . 93
G.3 Data Analysis and Statistical Methods . . . 96
G.4 Computational Modeling and Simulations . . . 98
G.5 Molecular Spectroscopy and Line List . . . 100
G.6 Observational Instruments and Techniques . . . 101

References **103**

List of Tables

1 Summary of high-resolution ground-based spectrographs for exoplanet atmosphere studies 14

2 WASP-178 system parameters 22

3 Summary of HST/STIS NUV Observations of WASP-178b 38

4 Details of the jitter engineering parameters used in the study. 40

5 Orbital parameters of WASP-178b used in the fit, table adapted from Lothringer et al. (2021) 44

List of Figures

1.1 Illustration of transit and eclipse geometry. 2
1.2 Transmission spectrum of hot Jupiter WASP-6b 4
1.3 An example of water features in HST WFC3 transmission spectra for WASP-43b . 5
1.4 Schematic of exoplanet atmospheric processes that can be observed in different regions with different spectral ranges 7
1.5 Summary of the current and future space-based telescopes for atmospheric characterization. 12
1.6 CO Isotopologue Opacities at High Temperature and Pressure 13
1.7 Transmission spectra of 10 hot Jupiters with Na, K, and H_2O absorption 18
1.8 Convergence of hot Jupiter atmospheric circulation patterns across independent GCM simulations 20
1.9 WASP-178b NUV-optical transmission spectrum and retrieved P-T profile 24
1.10 Pressure–temperature (P–T) profiles of three ultra-hot Jupiters 24
1.11 Best-fit spectra of WASP-178b from retrievals based on HST and JWST Broadband Spectroscopy 26
1.12 Overview of SiO Absorption Cross-sections 27
1.13 Schematic of the SiO-Driven Thermal Feedback Mechanism 28
1.14 Simulated SiO absorption spectra at 2000 K showing the three main bands of the UV-IR system 32
1.15 Temperature dependence of the SiO spectra using the SiOUVenIR line list 32
1.16 SiO absorption features in the UV domain 33
2.1 WASP-178b Mean Time-Series Spectra and Signal-to-Noise Ratio 37
2.2 Zoom-in Spectra of the Mg II Doublet 37
2.3 Raw white light curve of WASP-178b 39
2.4 Correlation of HST engineering parameters with flux variations 41
2.5 Temporal evolution of HST pointing parameters during transit observation 42

2.6 WASP-178b White Light Fit 45
2.7 Doppler Correction of WASP-178b's Transmission Spectrum 48
3.1 Simulated absorption cross-sections of SiO at 2470 K 50
3.2 In-band/Out-of-band Masking Scheme 53
3.3 Visualization of In-Band, Out-of-Band, and Between-Band Selection 56
4.1 4 Å transmission HST/STIS/E230M of WASP-178b Compared to WASP-121b . . 58
4.2 Native-Resolution NUV Transmission Spectrum of WASP-178b 59
4.3 Quality Filtering of NUV Transmission Spectrum 60
4.4 Gaussian Sampling Distributions for In-/Out-of-Band SiO Transit Depths 61
4.5 Model transit light curves for in-band and out-of-band wavelength regions 62
4.6 Sensitivity Analysis for SiO Detection 63
4.7 Bootstrap Sensitivity Analysis 64
A.1 Schematic depiction of hot Jupiter formation scenarios 73
A.2 Carbon-to-oxygen ratio (C/O) in a typical protoplanetary disk 75
B.1 Transmission spectrum of WASP-96 b showing pressure-broadened Na I 79
C.1 Regime diagram for giant planets and brown dwarfs 82
D.1 Example transit light curve fit (Binsize = 200 Å) 86
D.2 Broadband (binsize = 200 Å) NUV transmission spectrum of WASP-178b 87
D.3 Example transit light curve fit (Binsize = 4 Å) 88
D.4 Narrowband (binsize = 4 Å) NUV transmission spectrum of WASP-178b 88

1 Introduction

1.1 Background and Theoretical Framework

The first confirmed detection of a planet orbiting a Sun-like star in 1995 (Mayor & Queloz, 1995) transformed exoplanetary science from theoretical speculation into observational reality. Over the past three decades, the field has evolved from simply discovering distant worlds to comprehensively characterizing their physical and chemical properties. Atmospheric characterization has emerged as the primary tool for understanding exoplanet diversity: high-precision transmission spectroscopy reveals molecular compositions, emission spectroscopy constrains temperature structures, and phase-curve observations map global circulation patterns and cloud distributions. Together, these observational techniques enable systematic comparisons across the growing exoplanet population and provide crucial constraints on planetary formation and evolutionary histories.

Atmospheric characterization can be conducted through several observational configurations, with transiting systems offering particular advantages due to favorable geometry (Madhusudhan, 2019). In a transiting geometry, the planet periodically passes in front of and behind its host star relative to the observer, as presented in Figure 1.1. During the primary transit (i.e., when the planet crosses the stellar disk), starlight is filtered through the planet's atmosphere, where absorption and scattering by atmospheric constituents create wavelength-dependent signatures that reveal atmospheric composition. During the secondary eclipse (i.e when the planet passes behind the star), measurements of the star's brightness with and without the planet's contribution enable detection of thermal emission and reflected light from the planet's dayside. Non-transiting planets can still be characterized through high-resolution spectroscopy (eg: τ Boötis b in Baliunas et al. (1997)) or direct imaging techniques (Marois et al., 2008; Lagrange et al., 2010; Quanz et al., 2015; Chauvin et al., 2017; Bohn et al., 2020).

A major challenge in atmospheric characterization is the brightness contrast between the star and the orbiting planet, which can exceed several orders of magnitude. Precision photometric and spectroscopic techniques are therefore required to measure the subtle changes in flux that carry

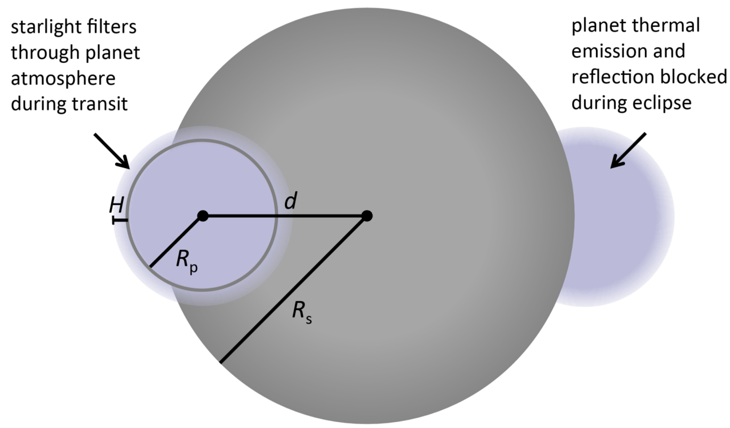

Figure 1.1: Illustration of transit and eclipse geometry. As the planet orbits its host star, it periodically moves in front of the stellar disk (transit) and behind it (eclipse). Key parameters are labeled, including the planetary and stellar radii (R_p and R_*), the atmospheric scale height (H), and the projected separation of their centers in the plane of the sky (d). Figure 2 from Kreidberg 2018.

the signatures of atmospheric processes. Recent advances in instrumentation have dramatically improved our capabilities, with the James Webb Space Telescope (JWST) now providing unprecedented sensitivity for exoplanet spectroscopy (Greene et al., 2016). In the coming years, additional facilities like Ariel (Tinetti et al., 2018) will further expand our capabilities, enabling systematic studies of diverse exoplanet atmospheres across a wide range of physical conditions.

Clouds and hazes—tiny solid or liquid particles suspended in an atmosphere, appear in a wide range of sub-stellar objects, from brown dwarfs to gas giants and possibly even rocky exoplanets (Kreidberg et al., 2014a; Helling & Casewell, 2014; Crossfield & Kreidberg, 2017; Gao et al., 2021). Despite their prevalence, it is still hard to map out how aerosol properties change with temperature. Transmission-spectroscopy surveys often show muted spectral features across many temperatures (Sing et al., 2015; Barstow et al., 2017). These subdued signals point to clouds and hazes as major players and highlight the need for a clearer picture of how aerosols form and evolve.

Between roughly 950 K and 2100 K, microphysical models predict that silicate clouds, mainly enstatite ($MgSiO_3$) and forsterite (Mg_2SiO_4), should dominate (Visscher et al., 2010; Powell et al., 2019; Gao et al., 2020). Observations of wavelength-dependent extinction support this prediction (Fu et al., 2021). Above this window the silicates stay in the gas phase, while below it condensates like ZnS and KCl become stable (Gao & Benneke, 2018).

Ultra-hot Jupiters ($T_{\rm eq} \geq 2200$ K) push these limits. Their daysides are hot enough to keep even the most refractory species gaseous (Lothringer et al., 2018; Kitzmann et al., 2018; Parmentier, Vivien et al., 2018), making them natural testbeds for near cloud-free conditions. Large day–night temperature contrasts, however, can still trigger condensation on the nightside or at the morning terminator (Ehrenreich et al., 2020; Helling et al., 2021). Observational constraints on this cloudy-to-cloud-free transition critically test microphysical cloud formation models and provides insights into high-temperature atmospheric chemistry processes.

1.1.1 Fundamentals of Transmission Spectroscopy

Transmission spectroscopy is the most established and widely implemented technique for probing exoplanet atmospheres (Seager & Sasselov, 2000; Brown, 2001; Charbonneau et al., 2002). During a planetary transit, starlight passes through the planet's atmospheric annulus, where atmospheric constituents selectively absorb and scatter radiation at characteristic wavelengths. This wavelength-dependent feature creates a unique spectral fingerprint that can be analyzed to determine atmospheric composition and physical properties.

When the planet is positioned fully in front of the stellar disk, the measured flux during transit ($F_{\rm in}$) decreases relative to the out-of-transit flux ($F_{\rm out}$). Assuming a uniformly illuminated stellar disk, the transit depth δ can be approximated as:

$$\delta \approx 1 - \frac{F_{\rm in}}{F_{\rm out}} = \left(\frac{R_p}{R_*}\right)^2, \tag{1}$$

where R_p and R_* denote the planetary and stellar radii, respectively. This transit depth exhibits wavelength dependence because the opacity of the planetary atmosphere varies across the electromagnetic spectrum. At wavelengths corresponding to strong atomic or molecular transitions,

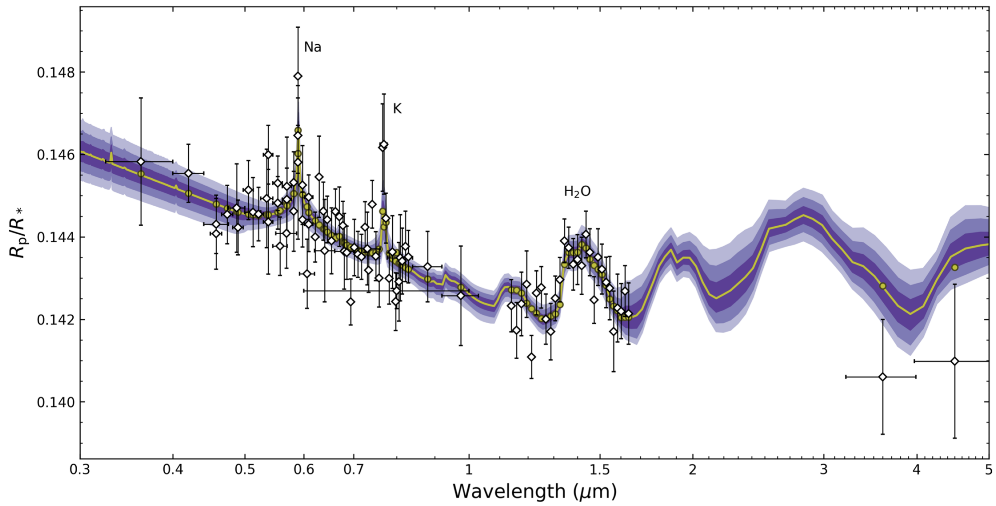

Figure 1.2: Transmission spectrum of hot Jupiter WASP-6b showing atmospheric absorption features due to sodium (Na), potassium (K), and water vapor(H_2O). The yellow line represents the best-fit atmospheric retrieval model, with purple shaded regions indicating the 1, 2, and 3σ confidence intervals. The spectrum reveals both clear atomic and molecular signatures as well as evidence for atmospheric haziness from the sloped optical spectrum. Figure 13 from Carter et al. 2020.

the atmosphere becomes more opaque, causing the planet's effective radius to appear larger in these spectral regions (Seager & Sasselov, 2000). The atmospheric annulus through which stellar light traverses during transit constitutes only a small fraction of the planet's cross-sectional area, approximately 1% of the planetary disk. This translates to roughly $0.01 \times 0.01 = 10^{-4}$ times the stellar area (Brown, 2001; Seager & Sasselov, 2000). Despite this challenging ratio, transmission spectroscopy has successfully revealed numerous atmospheric constituents.

Strong atomic absorption lines, particularly sodium (Na) and potassium (K), were among the first spectral features identified in exoplanet atmospheres (Charbonneau et al., 2002; Snellen et al., 2008; Redfield et al., 2008; Fossati et al., 2010; Lendl et al., 2017). Figure 1.2 shows the transmission spectrum of the inflated hot Jupiter WASP-6b with clear signatures of both atomic species (Na, K) and molecular absorption (H_2O), along with evidence for atmospheric aerosols that partially obscure these features (Carter et al., 2020).

Molecular species have been detected in numerous planetary atmospheres (Tinetti et al., 2007; Birkby et al., 2013; Deming et al., 2013; Kreidberg et al., 2014b; Kreidberg et al., 2015; Evans

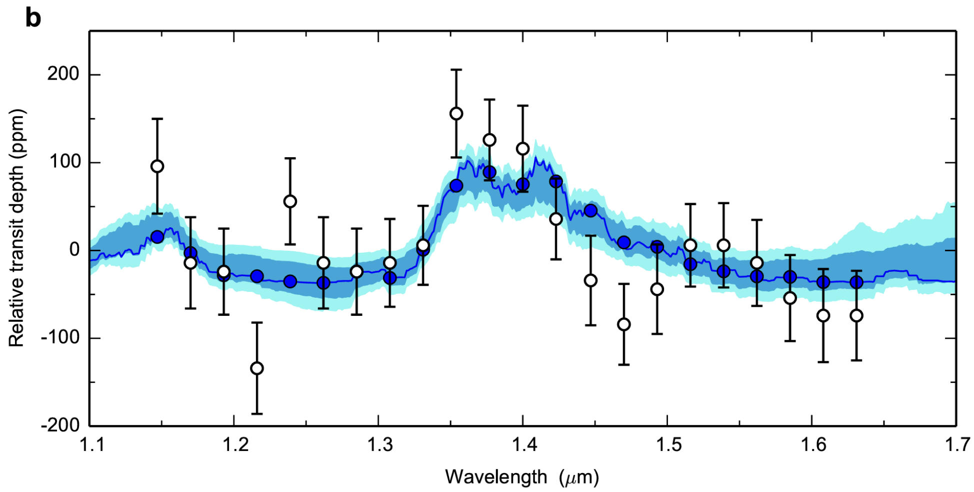

Figure 1.3: Transmission spectrum of the hot Jupiter WASP-43b, compared to best-fit models. Data are from HST/WFC3 (1.1–1.7 μm) and *Spitzer*/IRAC (3.6 and 4.5 μm). The blue line represents the best-fit model, with dark and light blue shading indicating the 1- and 2-σ confidence intervals from atmospheric retrieval. Water absorption at 1.4 μm is detected with >5σ significance, arising from the averaging of 10^4 rotational and vibrational line transitions. Retrieval analysis constrains the water abundance to 0.4–3.5× solar at 1σ confidence. Figure adapted from Kreidberg et al. 2014b.

et al., 2016). Water exhibits a prominent absorption feature at 1.4 μm, making it a primary target for exoplanet atmospheric studies. The HST/WFC3 instrument has successfully detected this feature in numerous hot Jupiters, as the example shown in Figure 1.3 for WASP-43b.

Interpreting a transit spectrum starts with radiative-transfer models that track how starlight is absorbed and scattered as it skims the planet's limb. The calculations include gas absorption lines and continuum scattering by molecules, aerosols, and clouds (Seager & Sasselov, 2000; Mollière et al., 2022). Fitting these models to the data yields constraints on atmospheric composition, temperature, and particle loading (Tinetti et al., 2007; Waldmann et al., 2015; Sing et al., 2015). The expected amplitude of spectral features scales with the atmospheric pressure scale height H, the altitude over which the pressure drops by a factor of e. Under hydrostatic equilibrium and assuming an ideal gas, the scale height is given by:

$$H = \frac{k_b T_{\rm eq}}{\mu g}, \tag{2}$$

where k_b is the Boltzmann constant, $T_{\rm eq}$ is the planet's equilibrium temperature, μ is the mean molecular mass, and g is the surface gravity.

The wavelength-dependent transit depth, δ_λ, can be expressed as:

$$\delta_\lambda = \frac{(R_p + nH)^2}{R_s^2} - \frac{R_p^2}{R_s^2}, \tag{3}$$

which can be simplified to

$$\delta_\lambda \approx 2nR_pH/R_s^2. \tag{4}$$

where n represents the number of scale heights contributing to increased opacity. For clear atmospheres observed at moderate spectral resolution, $n \approx 2$ is typically assumed (Stevenson et al., 2016).

This relationship reveals that planets with large atmospheric scale heights—set by high temperatures and low mean–molecular weights, produce the strongest transmission signatures. These signals grow even larger when the planet also has low surface gravity and orbits a small host star, which together increase the fraction of starlight intercepted by the atmosphere. With their elevated temperatures, hot Jupiters are ideal candidates for transmission spectroscopy, and their expanded atmospheres yield transit depth variations of roughly 0.1 %. By contrast, Earth-size planets around Sun-like stars show features two to three orders of magnitude weaker, highlighting the difficulty of probing terrestrial atmospheres with present instruments (Kreidberg, 2018).

1.1.2 Wavelength-Dependent Atmospheric Signatures

Transmission spectroscopy relies on its wavelength-dependent nature, which allows different atmospheric layers to be probed simultaneously. Each spectral range interacts with specific atmospheric constituents at various altitudes, and create a detailed vertical profile of the exoplanet's atmosphere. Figure 1.4 from Madhusudhan (2019) maps the electromagnetic spectrum to specific pressure levels and the corresponding atmospheric processes.

The vertical structure of exoplanet atmospheres can be stratified into distinct pressure regions,

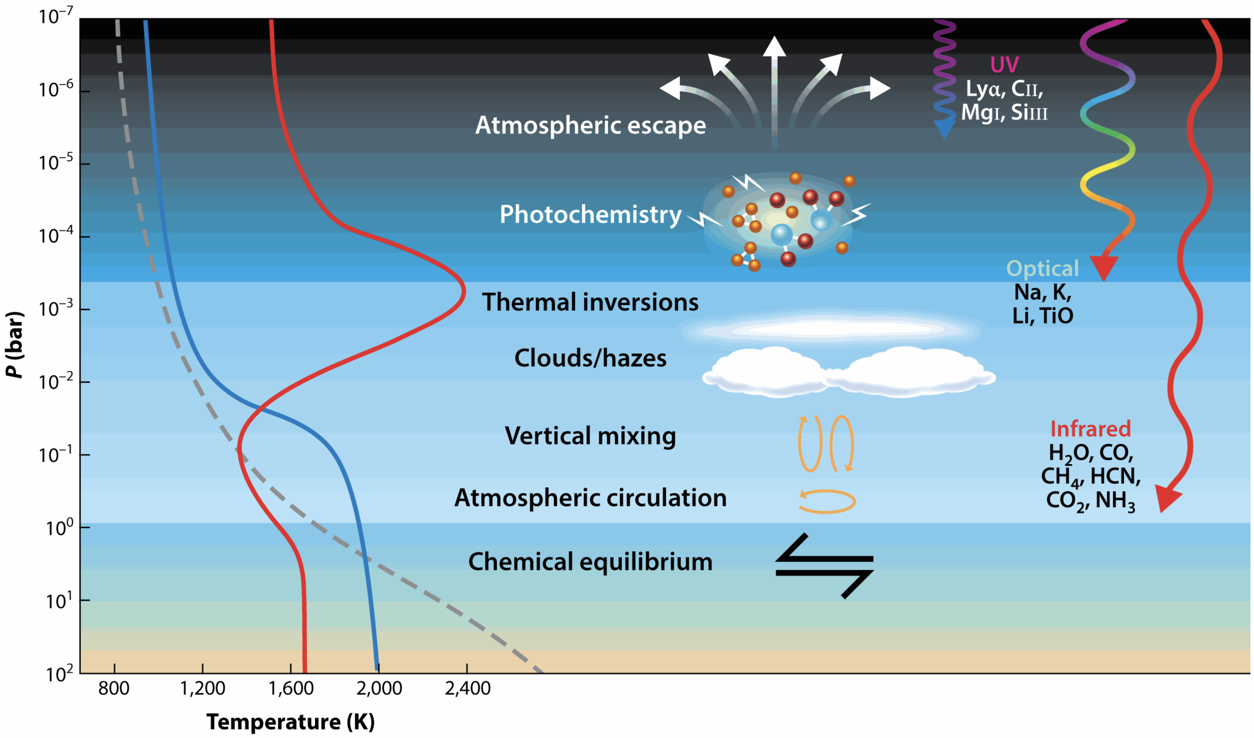

Figure 1.4: Schematic representation of major atmospheric processes in exoplanets and how different spectral ranges probe various atmospheric layers. The right side indicates the penetration depths of UV, optical, and IR radiation, along with the chemical species detectable in each range. The left side shows three possible temperature profiles: a highly irradiated planet with a thermal inversion (red), an irradiated planet without inversion (blue), and a less-irradiated planet (gray dashed). Figure from Madhusudhan 2019.

each characterized by unique physical and chemical processes:

- **Deep Atmosphere (**$P \geq 1$**) bars):** Thermochemical equilibrium and radiative–convective equilibrium dominates at these region due to high pressures, temperature, opacity and density. Compositions are determined by minimization of Gibbs free energy.

- **Mid-Atmosphere (**$P \sim 0.01$ **to** 1 **bar):** Vertical mixing and atmospheric circulation transport gas and heat throughout this layer. Cloud and haze formation occurs here through condensation or photochemical processes, influencing atmospheric opacity. Both IR and visible observations probe this region, allowing for the detection of molecular signatures and cloud/haze scattering.

- **Upper Atmosphere (**$P \sim 0.001$ **to** 0.01 **bar):** Thermal inversions may form due to absorption of stellar radiation by species like TiO, SiO and VO. Heavy metal species and certain atomic species predominate. Visible-light observations are used to study this region.

- **Upper-to-Outermost Atmosphere (**$P \sim 10^{-3}$ **to** 10^{-6} **bar):** Photochemical processes drive molecular dissociation and formation of new species. Atomic species and photochemical signatures are observed using optical and UV observations.

- **Outermost Atmosphere (**$P < 10^{-6}$ **bar):** Atomic species can escape the planet's gravitational field at these extremely low pressures. UV, extreme UV (EUV), and X-ray observations are critical for detecting these escape processes, as atomic species strongly absorb in these high-energy wavelength regimes.

Different wavelength regimes serve as windows to specific atmospheric constituents and processes. Near-infrared (NIR) and infrared (IR) observations (typically 0.8-5 μm) access vibrational-rotational bands of molecules such as H_2O, CO, CO_2 and CH_4, which have been detected in various hot Jupiters and warm Neptunes (Tinetti et al., 2007; Swain et al., 2008; Deming et al., 2013; Kreidberg et al., 2014b; Madhusudhan, 2019).

Optical to near-ultraviolet (NUV) wavelengths (approximately 0.3-0.8 μm) probe higher atmospheric layers where heavy metal oxides such as TiO and VO can absorb strongly, depending on temperature conditions (Knutson et al., 2008; Charbonneau et al., 2008; Todorov et al., 2010; Schwarz et al., 2015). This spectral range also captures absorption from atomic species including Na, K, Fe, Mg, and Si, whose presence depends on the excitation and ionization states within the atmosphere (Redfield et al., 2008; Fossati et al., 2010; Wyttenbach et al., 2015). HST STIS observations of WASP-12b, for example, revealed that optical absorption was dominated by aerosol opacity rather than TiO, suggesting the prevalence of haze formation (Sing et al., 2013). In ultra-hot Jupiters like WASP-76b, sodium absorption is particularly prominent accompanied by a scattering slope indicative of aerosol presence (von Essen, C. et al., 2020).

Ultraviolet (UV) observations (0.115-0.3 μm) provide a unique opportunity to study the outermost regions of exoplanet atmospheres where atmospheric escape processes occur. HST STIS UV observations have been widely used in detecting these phenomena; for instance, studies of WASP-12b revealed an early ingress in the near-UV transit light curve, suggesting significant mass loss from the planet's atmosphere (Fossati et al., 2010); Sing et al. (2019) identified the presence of Mg II and Fe II in the exosphere of WASP-121b, reaching altitudes beyond the Roche lobe.

In hot Jupiters ($T_{\mathrm{eq}} \sim 1000-2500$K), equilibrium chemistry dictates that carbon predominantly exists as CO rather than CH_4, while oxygen appears primarily as H_2O and CO. Consequently, the detection of species like CO_2 formed through the reaction of CO and H_2O becomes a useful diagnostic tool for atmospheric metallicity and C/O ratios (Moses et al., 2012). The presence or absence of refractory elements such as Na, K, Fe, Ti, and Si in the gas phase reflects condensation temperatures and can indicate whether these species have rained out of the atmosphere, adding to the constraints of day-night temperature gradients (Lothringer et al., 2020).

Recent advances with JWST have dramatically improved our ability to observe multiple spectral features simultaneously across a wide wavelength range, enabling more comprehensive atmospheric characterization. The NIRSpec and MIRI instruments, covering $\sim 0.6-28$ μm, capture the signatures of numerous molecular species (e.g., CO, H_2O, CO_2, H_2S, SO_2), allowing for new constraints on atmospheric composition, thermal structure, and potentially formation mechanisms (Greene et al., 2016; Ahrer et al., 2023; Fu et al., 2024).

1.1.3 Current and Planned Observational Facilities

Following the first exoplanet discoveries around main-sequence stars in the 1990s (Mayor & Queloz, 1995; Marcy & Butler, 1998; Marcy et al., 1998), atmospheric characterization techniques have developed through a dual approach using both ground- and space-based observatories. Each platform provides specific advantages and confronts distinct challenges when studying exoplanetary atmospheres.

Space-Based Observatories

Space-based telescopes operate above Earth's atmosphere, eliminating telluric absorption and enabling observations in spectral regions inaccessible from the ground (Madhusudhan, 2019). Figure 1.5 summarizes current and planned space-based telescopes for exoplanet atmospheric characterization.

The Hubble Space Telescope (HST) has pioneered exoplanet atmospheric characterization since 1990. HST's Space Telescope Imaging Spectrograph (STIS, 0.115-1.03 μm) provides optical and UV spectroscopy, which enables detections of alkali metals, atmospheric escape signatures, and Rayleigh scattering slopes (Lecavelier Des Etangs et al., 2008; Fossati et al., 2010; Pont et al., 2013). The Wide Field Camera 3 (WFC3, 0.8-1.7 μm) has advanced exoplanet atmospheric science by measuring the 1.4 μm water (H_2O) band, leading to water detections in many exoplanets (Deming et al., 2013; Kreidberg et al., 2014b; Sing et al., 2015). Despite these contributions, HST's wavelength coverage excludes several important molecular features, including CO and CO_2 absorption bands beyond 2 μm.

The UV wavelength range (115–400 nm) is critical for probing exoplanetary upper atmospheres and characterizing atmospheric escape, hazes, and photochemical processes (Linsky et al., 2010; Ehrenreich et al., 2015). However, UV radiation from astrophysical sources is strongly absorbed by Earth's atmosphere, primarily by ozone (O_3) below $\sim$300 nm, but also significantly by carbon dioxide (CO_2) and water vapor (H_2O) (France et al., 2013), severely restricting ground-based UV observations (France et al., 2013). This atmospheric opacity blocks UV observations from the ground, making space-based telescopes like HST/STIS essential for UV characterization of exoplanets.

The James Webb Space Telescope (JWST) launched in December 2021 is a paradigm shift in exoplanet atmospheric characterization capabilities. With its 6.5 m primary mirror and broad wavelength range (0.6 to 28 μm), JWST provides exoplanetary spectra in unprecedented quality, dramatically improving our understanding of these distant worlds (Greene et al., 2016; Madhusudhan, 2019). JWST's suite of instruments offers complementary capabilities: NIRSpec (0.6–5.3 μm) delivers multiple spectroscopic modes with resolutions from $R \sim 100-2700$, ideal for detecting molecular features of H_2O, CO, CO_2 and CH_4; NIRISS (0.6–2.8 μm) employs Single Object Slitless Spectroscopy optimized for time-series observations (TSO); NIRCam (0.6–5.0 μm) provides high-precision photometry and grism spectroscopy; while MIRI (5–28 μm) extends coverage to mid-infrared wavelengths, accessing additional molecular features and thermal emission from cooler planets.

Initial JWST observations have already yielded revolutionary results, including the first detection of CO_2 in an exoplanet atmosphere (Ahrer et al., 2022), observation of photochemically produced SO_2 (Tsai et al., 2023), and more precise constraints on metallicity and C/O ratios than previously achievable (Ahrer et al., 2023). This wealth of high-quality data presents new challenges for data interpretation, as more complex atmospheric models incorporating three-dimensional effects, disequilibrium chemistry, and comprehensive opacity databases will be required to fully leverage JWST's unprecedented observational capabilities (Barstow & Heng, 2020).

Looking ahead, the Atmospheric Remote-sensing Infrared Exoplanet Large-survey (ARIEL) scheduled for launch in 2029 will conduct a statistical survey of approximately 1000 exoplanet atmospheres (Tinetti et al., 2018; Edwards et al., 2019). Operating in the 0.5-7.8 μm range, ARIEL is specifically designed to efficiently characterize the chemical composition and thermal structure of diverse exoplanetary atmospheres, complementing JWST's more detailed but time-intensive

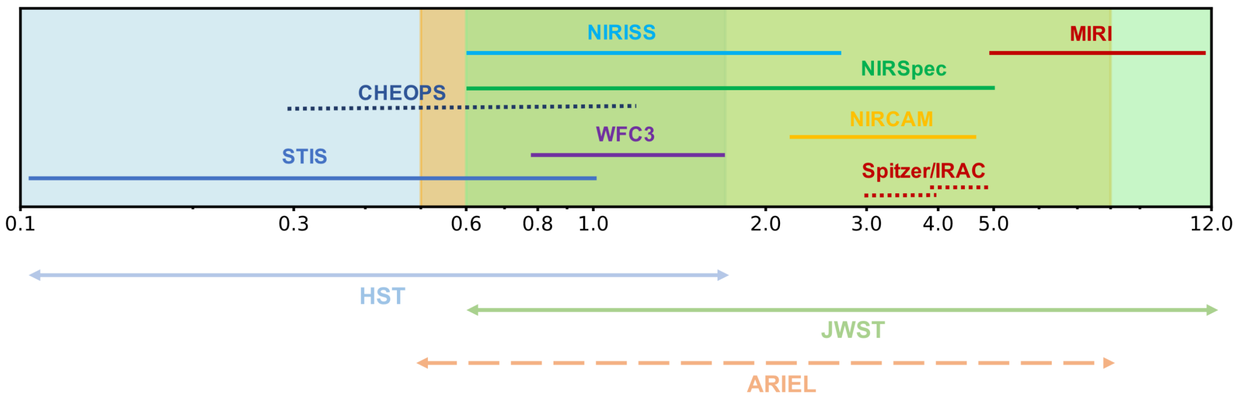

Figure 1.5: Summary of the current and future space-based telescopes for atmospheric characterization. The figure shows the wavelength coverage of HST instruments (STIS and WFC3, spanning 0.1-1.7 µm), JWST's four instruments (NIRISS, NIRCam, NIRSpec, and MIRI, collectively covering 0.6-28 µm), and the future ARIEL mission (0.5-8 µm). These spectroscopic instruments operate at resolving powers between R 20-1000. Also indicated are the photometric channels of Spitzer/IRAC (now retired) and CHEOPS (shown with dotted lines). Each mission provides complementary capabilities for exoplanet atmospheric studies across different wavelength regimes. Figure 1.5 from Gressier 2022.

observations of individual targets. ARIEL will employ three photometric channels (0.5-0.6, 0.6-0.8, and 0.8-1.1 µm) and two spectrometers with moderate resolving power of $R \sim 30\tilde{}200$ (Pascale et al., 2018). The primary science goals ARIEL intend to achieve include creating the first large-scale comparative survey of exoplanet atmospheres, investigating atmospheric chemistry across diverse planetary types, and establishing correlations between atmospheric properties and key planetary and stellar parameters (Edwards et al., 2019).

Ground-Based Observatories

Ground-based facilities offer complementary capabilities to space-based telescopes, primarily through their capacity for high-resolution spectroscopy ($R \sim 50,000 - 100,000$). Current major observatories include the Very Large Telescope (VLT), Keck, Gemini, and Subaru, with next-generation facilities under construction such as the European Extremely Large Telescope (E-ELT), the Thirty Meter Telescope (TMT), and the Giant Magellan Telescope (GMT) (Johns et al., 2012; Skidmore et al., 2015; Tamai et al., 2016). Recent work by Rukdee et al. (2020) shows that even higher resolution spectroscopy (R$\sim 300,000$) can resolve the fine structure of key biosignatures

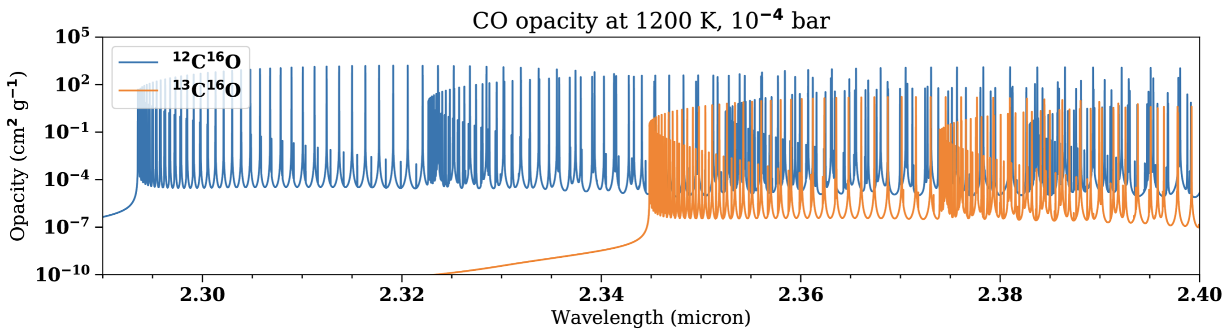

Figure 1.6: Opacity comparison of $^{12}C^{16}O$ and $^{13}C^{16}O$ at $T = 1200$ K and $P = 10^{-4}$ bar. Opacities are shown across the 2.29–2.40 μm range, where the $^{13}C^{16}O$ band head near 2.345 μm is distinctly visible. Abundances are scaled assuming $^{12}C^{16}O$ comprises 98.7% and $^{13}C^{16}O$ 1.1% of all CO molecules, reflecting typical conditions probed in hot Jupiter atmospheres through high-resolution spectroscopy (e.g., HD 179949b). Figure 2 from Mollière & Snellen 2019.

like O_2 lines, significantly enhancing detection capabilities for potentially habitable worlds. High spectral resolution ground-based observatories enables:

- Detection of molecular species through cross-correlation techniques that combine the signal from many spectral lines, allowing identification of molecules when individual lines are too weak to detect [1].
- Separation of planetary spectral features from telluric contamination based on their Doppler shifts due to the planet's orbital motion (Cabot et al., 2018).
- Detection of planetary winds and rotation through spectral line broadening (Snellen et al., 2010; Brogi et al., 2016).
- Differentiation of isotopologues through slight wavelength shifts in absorption features (see Figure 1.6 from Mollière & Snellen (2019))

Table 1 summarizes the specifications of several high-resolution spectrographs currently employed in exoplanet atmospheric studies. The Echelle SPectrograph for Rocky Exoplanets and Stable Spectroscopic Observations (ESPRESSO) at the Very Large Telescope (VLT) provides high

[1] For an accessible introduction to high-resolution spectroscopy and cross-correlation methods, see Hoeijmakers, J. (2020). *Introduction to high-resolution spectroscopy and application of the cross-correlation technique.* https://www.youtube.com/watch?v=S9aXndF73wE

stability with a design goal of 10 cm/s precision for radial velocity measurements (Pepe et al., 2021). This instrument has contributed to several significant discoveries, including the detection of barium(Ba^+) in the atmospheres of ultra-hot Jupiters WASP-76b and WASP-121b (Azevedo et al., 2022). The original High Accuracy Radial Velocity Planet Searcher (HARPS, Mayor et al. (2003)) on the ESO 3.6m telescope has been a workhorse for exoplanet detection and characterization for nearly two decades, while newer instruments like NEID aim to achieve similar precision levels (Schwab et al., 2016).

Spectrograph	**Telescope**	**Wavelength Range**	**Resolution**
ESPRESSO	VLT (4 × 8.2m UTs)	0.38–0.78 µm	140,000–190,000
HARPS	ESO (3.6m)	0.378–0.691 µm	115,000
HARPS-N	TNG (3.58m)	0.383–0.693 µm	115,000
CARMENES	Calar Alto (3.5m)	0.52–1.71 µm	80,000–100,000
UVES	VLT (8.2m)	0.3–1.1 µm	up to 110,000
NEID	WIYN (3.5m)	0.38–0.93 µm	100,000
GIANO-B	TNG (3.58m)	0.95–2.45 µm	∼50,000
ANDES (planned)	ELT (39m)	0.4–2.5 µm	up to 1,000,000

Table 1: Summary of high-resolution ground-based spectrographs for exoplanet atmosphere studies

Despite their advantages in high spectral resolution, ground-based telescopes face several hard limits. Telluric absorption confines useful data to the clear optical and near-infrared windows, and at high resolution the main residual systematic is stellar activity that masks or mimics planetary lines (Cauley et al., 2018). Turbulence, clouds, and changing water-vapor columns further blur or dim the signal; adaptive optics and differential analysis reduce but do not remove these effects. Since the Earth's atmosphere blocks nearly all ultraviolet light, ground-based UV spectroscopy remains unattainable.

The next generation of 30–40 m observatories—the 39 m European Extremely Large Telescope (ELT), the 30 m Thirty Meter Telescope (TMT), and the 24.5 m Giant Magellan Telescope (GMT)—is expected to enter service in the early 2030s and will significantly sharpen constraints on exoplanet atmospheres (Tamai et al., 2016). On the ELT, the high-dispersion spectrograph ANDES (formerly ELT-HIRES) will span 0.4–2.5 µm at resolving power up to $R \sim 1,000,000$. Simulations show that such resolution and collecting area can isolate individual lines of oxygen (O_2), water (H_2O), and methane (CH_4) in Earth-size planets transiting nearby M dwarfs, measure atmospheric escape from hot Neptunes, and potentially search for biosignature gases in habitable-zone worlds (Snellen et al., 2015; Lopez-Morales et al., 2019).

Synergies Between Observational Platforms

A combination of observations with space- and ground-based facilities gives a depth of atmospheric coverage impossible for any single instrument. HST's UV spectra constrain upper-atmosphere escape and photochemistry; JWST supplies near- and mid-infrared spectra that probe molecular bands and the temperature–pressure profile; and high-resolution optical/infrared spectrographs on large ground-based telescopes isolate individual lines, measure winds, and map atmospheric composition. Joint campaigns (e.g., HST/STIS + JWST/NIRSpec + VLT/ESPRESSO) thus track the same atmosphere from the thermosphere to the deep photosphere. The payoff is clear: combined HST and *Spitzer* spectra for 10 hot Jupiters revealed a trend of lower cloud opacity with higher equilibrium temperature and exposed wide variation in water-band strengths (see Figure 1.7 from Sing et al. (2015)); merging VLT/CRIRES cross-correlation data with HST/WFC3 spectra for HD 209458b cut the uncertainties on CO and H_2O abundances by a factor of 3–5 by breaking temperature–composition degeneracies (Brogi & Line, 2019). Multi-wavelength synergy is now essential for accurate, self-consistent atmospheric retrievals.

1.2 Atmospheric Chemistry and Thermal Structure of Hot Jupiters

1.2.1 Key Discoveries in Atmospheric Composition

Hot Jupiter atmospheres show distinctive chemical signatures shaped by their extreme thermal environments, with temperatures ranging from 1000 K in warm gas giants to over 2500 K in Ultra-Hot Jupiters (UHJs). The chemical inventory of these worlds has been progressively revealed since the landmark detection of sodium in HD 209458b Charbonneau et al. (2002), which provided the first direct evidence of an exoplanet atmosphere.

Atmospheric composition in hot Jupiters follows clear temperature-dependent patterns. Alkali metals (Na, K) produce strong resonance lines at optical wavelengths, detected across numerous systems (Sing et al., 2011b; Wyttenbach et al., 2015; Nikolov et al., 2018; Feinstein et al., 2023). The pressure-broadened profiles of these lines constrain atmospheric structure and reveal both pressure levels and temperature gradients. High-resolution spectroscopy has further characterized these features, showing variations in line depths, widths, and asymmetries that indicate atmospheric dynamics and escape processes (Louden & Wheatley, 2015; Wyttenbach et al., 2017).

Water vapor (H_2O) appears nearly ubiquitously in hot Jupiter spectra, although its detected abundance varies significantly (see Figure 1.7). HST/WFC3 observations consistently reveal H_2O absorption at 1.4 μm, with strength varying from prominent features in planets like WASP-19b to weak or undetectable signals in others like WASP-31b. These variations correlate with overall atmospheric metallicity and the presence of clouds or hazes that mask spectral features (Sing et al., 2015; Wakeford et al., 2018; Pinhas et al., 2019).

Carbon chemistry shows strong temperature dependence across the hot Jupiter population. Carbon monoxide (CO) dominates in atmospheres above approximately 1200 K due to its strong molecular bond (Parmentier, Vivien et al., 2018; Yan et al., 2022; van Sluijs et al., 2023), with clear detections in high-resolution spectra of planets like WASP-33b and HD 189733b. At cooler temperatures ($T_{eq} \lesssim 1000$ K), methane (CH_4) becomes thermochemically favored, as recently confirmed in the warm Jupiter WASP-80b (Bell et al., 2023). Carbon dioxide (CO_2), formed through the reaction of CO and OH radicals, serves as a sensitive metallicity indicator (Madhusudhan & Seager, 2009) and has been definitively detected by JWST in multiple planets (Ahrer et al., 2023; Rustamkulov et al., 2023; Fu et al., 2024).

In Ultra-Hot Jupiters ($T_{eq} \geq 2200$ K), thermal dissociation dramatically alters atmospheric chemistry. Water molecules partially dissociate in upper atmospheric layers while CO largely remains intact. This creates distinctive pressure-dependent abundance profiles and modifies observed spectral features. JWST observations are now directly measuring these dissociation effects through precise abundance constraints at different atmospheric pressures (Coulombe et al., 2023).

Measurements of carbon-to-oxygen (C/O) ratios provide crucial insights into formation histories.

Planets with super-stellar C/O values may have formed beyond the CO_2 or CO ice lines, accreting carbon-enriched gas after the condensation of oxygen-bearing species like water. However, atmospheric processing and interior-atmosphere exchange can complicate these interpretations, thus multi-species abundance measurements are required for robust conclusions about formation pathways (Madhusudhan, 2012).

1.2.2 Temperature Variations in Hot Jupiter Atmospheres

Hot Jupiters exhibit complex three-dimensional temperature structures that deviate significantly from simple equilibrium temperature estimates. While equilibrium temperature (T_{eq}) provides a useful first approximation of a planet's global radiative balance, observations reveal substantial spatial temperature variations across these tidally-locked worlds (Parmentier, Vivien et al., 2018). These variations shape atmospheric chemistry, dynamics, and observable properties.

Phase curve observations directly map these temperature variations by measuring thermal emission as a function of orbital phase. For example, Knutson et al. (2007) measured the first detailed thermal map of HD 189733b, revealing a day-night temperature contrast of approximately 300 K, as shown in the top left panel of Figure 1.8). Subsequent observations of other hot Jupiters have shown day-night temperature differentials ranging from a few hundred to over 1000 K (Schwartz et al., 2017). These temperature gradients steepen with increasing equilibrium temperature, as radiative timescales shorten relative to advective timescales (Komacek et al., 2017).

Three-dimensional general circulation models (GCMs) successfully reproduce these observed temperature structures, including the eastward jet, hot spot offset, and day-night temperature gradients (Showman & Guillot, 2002; Showman et al., 2009; Rauscher & Menou, 2010; Rauscher & Kempton, 2014; Amundsen et al., 2016; Parmentier, Vivien et al., 2018). The temperature maps displayed in Figure 1.8 show the agreement between different modeling approaches in predicting these features. These models show that the ratio of radiative to advective timescales largely determines the efficiency of heat redistribution; hotter planets develop steeper temperature gradients as radiation dominates over advection, while cooler planets maintain more uniform temperatures

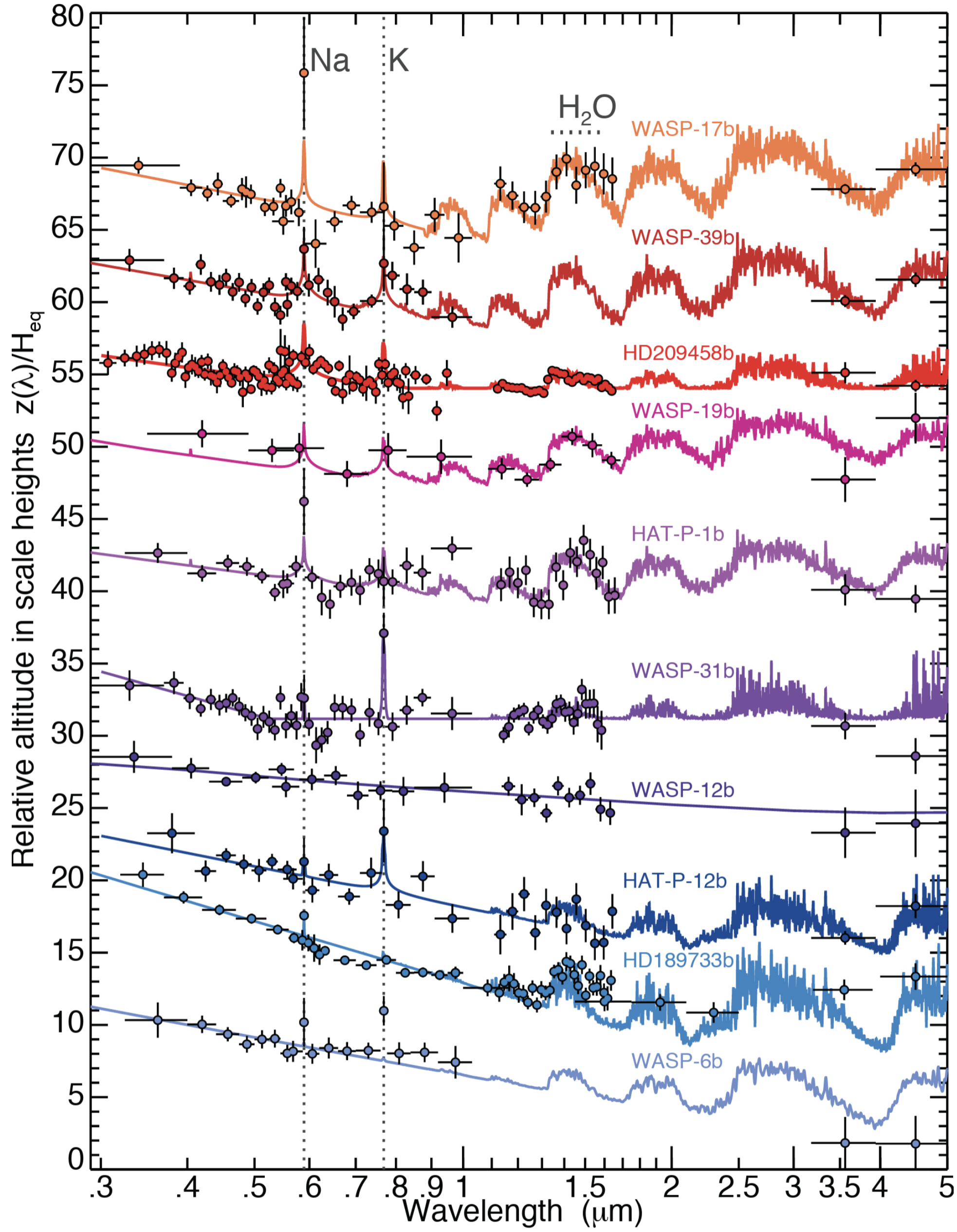

Figure 1.7: Transmission spectra of hot Jupiters, highlighting absorption features from Na, K, and H_2O, as well as optical scattering slopes (e.g., WASP-6b, HAT-P-12b). The planets are arranged vertically from those with clear atmospheres and prominent spectral features (top) to those with cloudy/hazy atmospheres and flatter spectra (bottom). H_2O vapor is detected in five of eight planets observed with WFC3, though its absorption strength varies significantly—from strong features (WASP-19b) to weak (HD 209458b) or undetectable (WASP-31b). Solid lines represent best-fit atmospheric models. Figure from Sing et al. 2015.

through atmospheric circulation (Komacek et al., 2017; Parmentier et al., 2021).

A key feature in these thermal maps is the eastward-shifted hot spot, the region of maximum temperature displaced from the substellar point in the direction of planetary rotation. This offset results from interactions between radiative forcing and superrotating equatorial jets (Showman & Guillot, 2002; Showman et al., 2009; Rauscher & Menou, 2010; Rauscher & Kempton, 2014; Amundsen et al., 2016; Parmentier, Vivien et al., 2018). Measurements of hot spot offsets range from $\sim 5°$ to $40°$ eastward, with the magnitude inversely correlating with equilibrium temperature (Knutson et al., 2007; Stevenson et al., 2014; Komacek et al., 2017). WASP-43b exhibits a modest offset of $12.3 \pm 1.0°$ despite its strong day-night temperature contrast (Stevenson et al., 2014), while cooler HD 189733b show larger offsets of 30-40°and more efficient heat redistribution (Knutson et al., 2007). These patterns provide direct evidence of atmospheric circulation and heat transport efficiency across the hot Jupiter population.

Beyond these horizontal temperature variations, vertical thermal structure is also complicated. Thermal inversions (where temperature increases with altitude) occur at microbar pressures in ultra-hot Jupiters due to shortwave radiation absorption. While TiO and VO were initially proposed as primary inversion-causing agents due to their visible-light absorption properties (Hubeny et al., 2003; Fortney et al., 2008), observational evidence has been complex. Early TiO detections in HD 209458b were later refuted (Désert et al., 2008; Diamond-Lowe et al., 2014), and studies of WASP-19b and WASP-12b produced contradictory results (Sing et al., 2013; Huitson et al., 2013). Recent high-resolution spectroscopy has better confirmed TiO in WASP-33b and WASP-121b, though at lower abundances than predicted (Nugroho et al., 2017; Merritt et al., 2021). In addition, recent works show that alternative opacity sources including atomic metals (Fe, Ni), metal hydrides, and SiO appear to be significant contributors to thermal inversions in UHJs (Lothringer et al., 2018; Gandhi & Madhusudhan, 2019).

Aerosols also modify atmospheric dynamics through radiative feedback. Clouds form on cooler nightsides and morning terminators where temperatures fall below condensation thresholds for silicates (e.g., $MgSiO_3$, Mg_2SiO_4), titanium, and iron (Powell et al., 2018; Gao et al., 2021; Roman

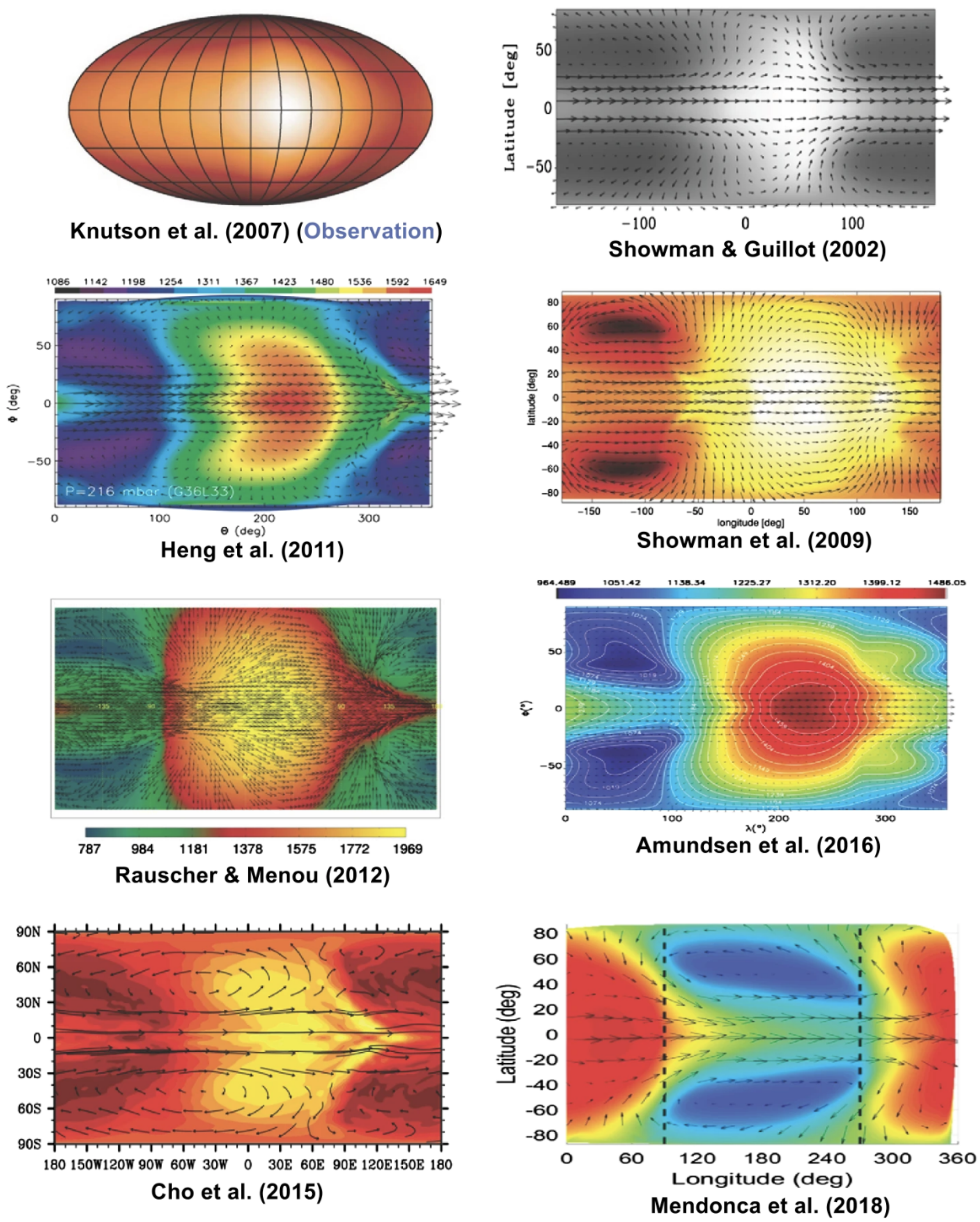

Figure 1.8: Convergence of hot Jupiter atmospheric circulation patterns across independent GCM simulations. Despite using different numerical approaches and physical approximations, all models produce consistent circulation regimes characterized by: (1) eastward equatorial jets with speeds of several km/s, (2) eastward-shifted hotspots relative to the substellar point, and (3) significant day-night temperature contrasts. Top left: Spitzer phase curve observations of HD 189733b showing the eastward hotspot offset (Knutson et al., 2007). Remaining panels display temperature maps (colors) and wind patterns (arrows) from seven independent GCM simulations of HD 209458b, HD 189733b, and WASP-43b, showing the robustness of hot Jupiter circulation patterns across different modeling frameworks (Showman & Guillot, 2002; Showman et al., 2009; Heng et al., 2011; Rauscher & Menou, 2012; Cho et al., 2015; Amundsen et al., 2016; Mendonça et al., 2018). For most panels, the substellar point is at the center, except for Mendonça et al. (2018) (bottom right) where the antistellar point is centered. Figure adapted from Showman et al. (2020).

et al., 2021). This creates observable day-night asymmetries in transmission spectra, as seen in WASP-121b (clear evening terminator, cloudy morning) and WASP-76b (Mikal-Evans et al., 2019; Ehrenreich et al., 2020). These findings validate 3D models predicting longitudinal cloud gradients (Parmentier et al., 2021). Cloud radiative effects can alter atmospheric temperatures by up to 200 K, modifying circulation and chemistry (Roman et al., 2021; Helling et al., 2021). In ultra-hot Jupiters, temperatures often exceed condensation thresholds across the dayside, producing clear atmospheres with atmospheric constituents remaining gaseous (Parmentier et al., 2016; Lothringer et al., 2018).

1.3 Ultra-Hot Jupiter WASP-178b

WASP-178b (also known as KELT-26b) is a highly inflated ultra-hot Jupiter (UHJ) with an equilibrium temperature of $T_{\rm eq} \sim 2470 \pm 60$ K, orbiting the chemically peculiar A-type star (Hellier et al., 2019; Martínez et al., 2020). The high-temperature conditions on UHJs like WASP-178b prevent the condensation of refractory species on the dayside, allowing refractory elements (e.g., Si, Fe, Mg) and volatile molecules (e.g., H_2O, CO) to remain in the gas phase, and atmospheric chemistry transitions from molecule-dominated to atom- and ion-dominated regimes due to intense stellar irradiation (Lothringer et al., 2018; Parmentier, Vivien et al., 2018).

Recent observations spanning from the near-ultraviolet (NUV) to the infrared (IR) have revealed a complex chemical inventory in WASP-178b's atmosphere, including the first evidence of gas-phase silicates (SiO) alongside atomic metals and molecular volatiles (Lothringer et al., 2021; Damasceno et al., 2024; Lothringer et al., 2025). These findings reveal high-temperature atmospheric processes (e.g., thermal dissociation, cloud formation) and provide clues to the planet's formation environment. In this section, we review the recent observational and modeling advances in characterizing WASP-178b's atmosphere.

1.3.1 Properties of WASP-178b and its Host Star

WASP-178b was identified independently by the Wide Angle Search for Planets (WASP) survey (Pollacco et al., 2006; Hellier et al., 2019) and the Kilodegree Extremely Little Telescope (KELT) survey (Pepper et al., 2007; Martínez et al., 2020). The planet orbits WASP-178 every 3.34 days at a distance of approximately 0.0558 AU. Table 2 summarizes the measured and inferred physical properties of the WASP-178 system.

Parameter	Value
Planetary Parameters	
Orbital period, P (days)[a]	3.3448285 ± 0.0000012
Transit epoch, T_0 (BJD_{TDB})[a]	$2456927.06839 \pm 0.00018$
Planet mass, M_p (M_J)[a]	1.66 ± 0.12
Planet radius, R_p (R_J)[a]	1.81 ± 0.09
Density, ρ_p ($g\,cm^{-3}$)[a]	0.35 ± 0.07
Surface gravity, $\log g_p$ (cgs)[a]	3.17 ± 0.06
Equilibrium temperature, T_{eq} (K)[a]	2470 ± 60
Spin-orbit alignment, λ (deg)[b]	$105^{+3.6}_{-4.2}$
Stellar Parameters	
Spectral type[a]	A1V (chemically peculiar)
Stellar mass, $M_\star$ ($M_\odot$)[a]	1.97 ± 0.10
Stellar radius, $R_\star$ ($R_\odot$)[a]	1.81 ± 0.09
Effective temperature, T_{eff} (K)[a]	9350 ± 150
Surface gravity, $\log g_\star$ (cgs)[a]	4.25 ± 0.05
Stellar metallicity, [Fe/H] (dex)[a]	$+0.21 \pm 0.16$
Projected rotation, $v \sin i$ ($km\,s^{-1}$)[a]	8.2 ± 0.6
Microturbulence velocity, v_{turb} ($km\,s^{-1}$)[a]	2.9 ± 0.2
Age (Myr)[a]	200^{+100}_{-50}
Distance, d (pc)[a]	408 ± 3

Table 2: WASP-178 system parameters. [a]Values from Hellier et al. (2019), [b]from Damasceno et al. (2024).

WASP-178b is notable for its substantial size and extreme temperature regime. With a radius of $1.81 \pm 0.09\ R_J$ and a mass of $1.66 \pm 0.12\ M_J$, it has a low bulk density of 0.35 g cm^{-3}. The host star, WASP-178, is an A1 IV-V type star with an effective temperature of 9350 ± 150 K, making it the second-hottest known planet-hosting star after KELT-9 (Gaudi et al., 2017). The star has $1.97 \pm 0.10 M_\odot$ and $1.81 \pm 0.09 R_\odot$, and its photosphere shows the metal enhancements typical of chemically peculiar Am stars (Hellier et al., 2019).

The extreme stellar radiation environment and proximity of WASP-178b to its host star create unique atmospheric conditions. The planet's high equilibrium temperature is expected to prevent silicate cloud formation on the dayside, while the misaligned orbit ($\lambda = 105^{+3.6}_{-4.2}$ degrees) indicates a complex dynamical history (Damasceno et al., 2024). This combination of properties makes WASP-178b an excellent laboratory for studying atmospheric chemistry at extreme temperatures and investigating the processes that shape ultra-hot Jupiter atmospheres.

1.3.2 Summary of Observational Campaigns

NUV Transmission Spectrum and SiO Detection

Lothringer et al. (2021) presented the NUV-Optical transmission spectrum of WASP-178b obtained with HST/WFC3/UVIS using the G280 grism (0.2-0.8 µm, $R \sim 70$) as part of Program 16086, and their observations revealed an enormous short-wavelength absorption feature between $\sim$ 0.2–0.4 µm. This near-ultraviolet (NUV) absorption is one of the largest spectral features observed in any exoplanet atmosphere (on the order of tens of scale heights). Bayesian retrievals attribute the NUV opacity to gas-phase refractory species, with silicon monoxide (SiO) providing the best fit and representing the first candidate detection of this molecule in an exoplanet atmosphere. The observed transmission spectrum and retrievals of WASP-178b are shown in Figure 1.9, showing a steep increase in transit depth at wavelengths shorter than 0.35 µm. The NUV transit depth between 0.2–0.28 µm is $2,500 \pm 138$ ppm higher than the optical continuum (0.35–0.8µm), representing a highly significant detection at the 18σ level. The retrieved pressure-temperature profile confirms that these wavelengths probe pressures $\lesssim 1$ micro bar, reaching into the planet's upper atmosphere.

The presence of SiO at such high temperatures is theoretically expected, as SiO should be the dominant Si-bearing gas in equilibrium above ~2000 K. Lothringer et al. (2021) inferred that WASP-178b's lack of condensate cloud signatures is consistent with a scenario where silicate clouds "burn off" at $T_{\rm eq} \geq 2000$K, and suggested that the onset of silicate cloud formation occurs in planets cooler than roughly 1950–2450K. The NUV absorption was thus interpreted as arising from gas-phase silicate precursors—SiO and Mg-bearing species, which are the major constituents of common silicate condensates like enstatite ($MgSiO_3$) and forsterite (Mg_2SiO_4) that remain in gaseous form in WASP-178b's intensely irradiated atmosphere.

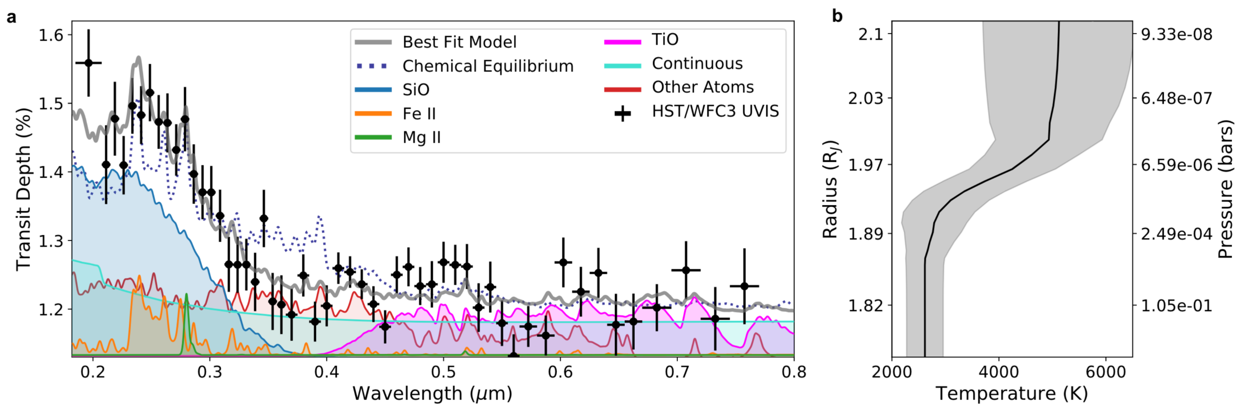

Figure 1.9: (a) HST/WFC3 G280 transmission spectrum of WASP-178b with 1σ uncertainties, overlaid with the contributions of dominant opacity sources from the best-fit atmospheric model. SiO dominates the opacity at short wavelengths. (b) Retrieved pressure-temperature profile, showing the 1σ confidence region (shaded) and the median profile (solid line), plotted on the same radius scale as panel (a). The data indicate that the minimum pressures probed are below 1 micro bar. Figure 1 from Lothringer et al. 2021.

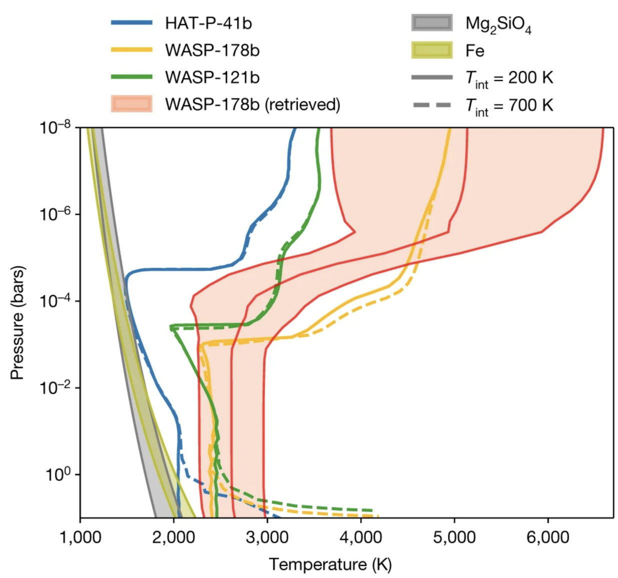

Figure 1.10: Pressure–temperature (P–T) profiles of three ultra-hot Jupiters—HAT-P-41b, WASP-121b, and WASP-178b compared with condensation curves for Fe and Mg_2SiO_4 assuming 1–10× solar metallicity. Cloud formation is expected where a planet's P–T profile intersects a condensation curve, as seen for HAT-P-41b. The plot also includes the retrieved median and 1σ confidence region for WASP-178b's atmospheric profile, consistent with theoretical models. Figure from Lothringer et al. 2021.

This discovery motivated the re-examination of other hot Jupiter spectra where SiO had not been previously considered. Figure 1.10 compares 1D pressure–temperature profiles of HAT-P-41b, WASP-121b, and WASP-178b with equilibrium condensation curves for silicate and iron. In atmospheres with 1–10× solar metallicity, these species condense between roughly 1500-2000 K at pressures from 1 millibar (mbar) to 10 bar. As the coolest in the sample, HAT-P-41b's profile intersect the curves and are expected to form silicate clouds. In contrast, WASP-121b and WASP-178b remain well above the condensation region, supporting a cloud-free limb and the presence of gaseous SiO. These results link the strong NUV absorption to high-temperature silicate precursors and define a temperature threshold for cloud formation in ultra-hot Jupiters.

Optical High-Resolution Spectroscopy (ESPRESSO)

Complementary to the space-based NUV observations, two VLT/ESPRESSO transits provide a complementary, ground-based view of WASP-178b's atmosphere (Damasceno et al., 2024). Narrow-band analysis resolves Na I (5.5–5.4σ in two separate nights), Hα (13σ), Hβ (7.1σ), and a tentative Hγ signal, while cross-correlation recovers Mg I (5.8–7.8σ) and strong signals of Fe I and Fe II, each at $\sim$10–12σ confidence.

The metal lines show no net Doppler shift, implying negligible day-to-night winds at the terminator, but exhibit moderate broadening ($\sim$16 km s^{-1} for Fe I, $\sim$11 km s^{-1} for Fe II). In contrast, Hα and Hβ are broadened to 30–40 km s^{-1}, consistent with an extended, possibly escaping hydrogen layer. These results confirm abundant neutral and ionised metals in the middle atmosphere and complement the NUV SiO absorption, building a coherent picture of a metal-rich, highly irradiated atmosphere with modest winds and ongoing mass loss.

HST and JWST Broadband Spectroscopy

More recently, Lothringer et al. (2025) combined HST/WFC3 G280 (0.2–0.4 µm), HST/WFC3 IR (1.1–1.7 µm), and *JWST*/NIRSpec G395H (2.8–5.1 µm) transit data to produce a 0.2–5.1 µm transmission spectrum of WASP-178b. Retrievals with `petitRADTRANS` and `ATMO` recover strong NUV opacity from SiO, Fe^+, and Mg^+ and weaker IR features from H_2O and CO. Best-fit chemical-equilibrium models yield $X_{\rm SiO} \sim 10^{-4.8}$, $X_{\rm H_2O} \sim 10^{-4}$–$10^{-3}$, and $X_{\rm CO} \sim 10^{-5.4}$, corresponding to

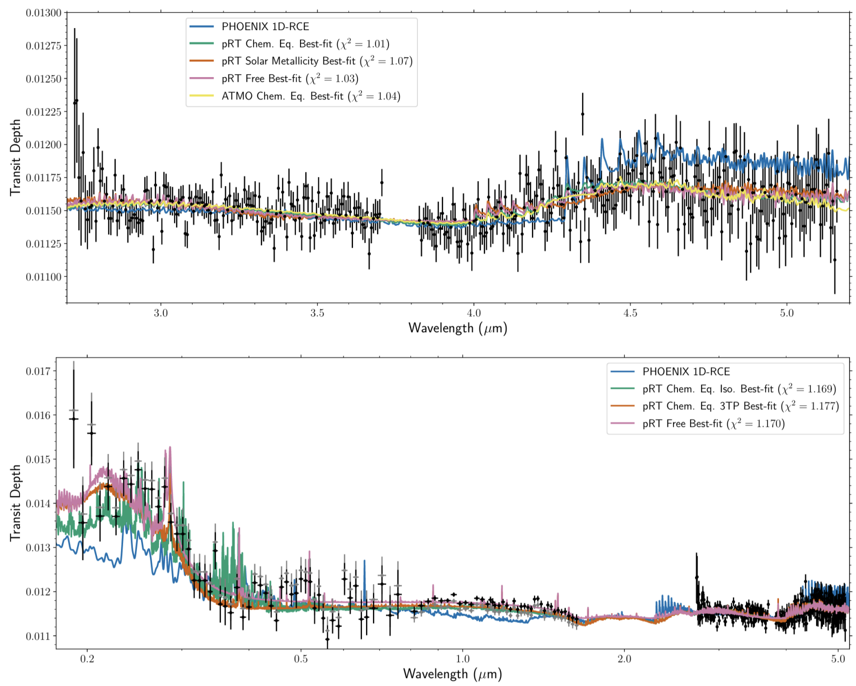

Figure 1.11: Atmospheric retrieval results for WASP-178b's transmission spectrum. **Top panel:** Best-fit spectra from independent modeling frameworks (`petitRADTRANS` and `ATMO`) assuming chemical equilibrium and using only JWST/NIRSpec G395H data (2.8–5.1 μm). **Bottom panel:** Best-fit models from `petitRADTRANS` applied to the combined HST + JWST observations (0.2–5.1 μm). Black points show the spectrum with offsets fitted in the free chemistry retrieval, while gray points indicate offsets from the chemical equilibrium retrieval. The combined dataset reveals both the strong NUV absorption (likely from SiO, Fe^+ and Mg) and the more moderate infrared molecular features from H_2O and CO. This multi-wavelength approach provides more robust constraints on atmospheric composition than infrared data alone. Figure from Lothringer et al. (2025).

[Si/H] $\sim -0.1 - 0.2$ and C/O ~ 0.01. Self-consistent radiative–convective profiles using `PHOENIX` show a thermal inversion reaching $\sim$3200 K at 10^{-3}–10^{-2} bar, driven by SiO and metal absorption. Because SiO's UV cross section is $\gtrsim 10^4$ times larger than its IR cross section, IR-only retrievals cannot constrain its abundance; multi-wavelength coverage is therefore essential (Fig. 1.11).

WASP-178b thus represents an archetype for highly irradiated gas giants that challenge existing atmospheric models. The evidence of SiO alongside the other refractory and atomic species expands our understanding of molecular inventories in UHJ atmospheres and, if robustly confirmed, would offer new insights into exoplanet atmospheric characterization under extreme conditions.

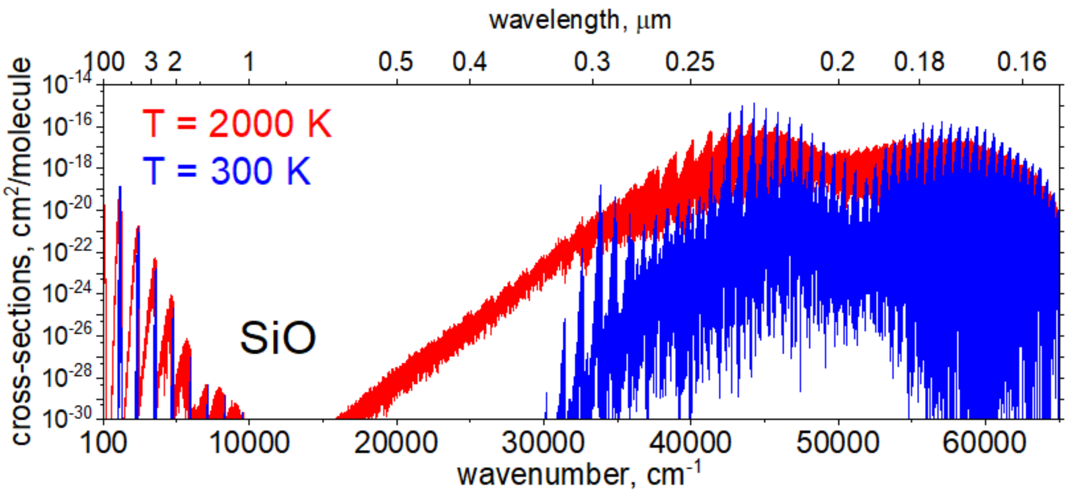

Figure 1.12: Absorption cross-sections of SiO across a broad wavelength range (0.16-100 μm) computed using the SiOUVenIR line list (Yurchenko et al., 2021). The spectra are shown at two temperatures: 2000 K (red line), representative of ultra-hot Jupiter conditions, and 300 K (blue line), shown for comparison. Note the strong enhancement in absorption at ultraviolet wavelengths (30,000 - 60,000 cm^{-1}) where electronic transitions dominate, compared to the infrared vibrational bands below 10,000 cm^{-1} (>1 μm). The higher temperature significantly increases the overall opacity and populates higher rotational and vibrational levels, broadening the absorption features.

1.4 The Role of Silicon Monoxide in Ultra-hot Jupiter Atmospheres

1.4.1 Theoretical Significance of SiO in Ultra-hot Jupiter Atmospheres

Silicon monoxide (SiO) is expected to be a dominant atmospheric constituent in ultra-hot Jupiters (UHJs) due to its high-temperature stability and strong near-ultraviolet (NUV) opacity (Lothringer et al., 2018; Helling et al., 2019; Lothringer et al., 2020). Figure 1.12 shows SiO's distinctive opacity characteristics: strong absorption in the near-UV (0.2-0.4 μm) with comparatively weak features at visible wavelengths (Yurchenko et al., 2021). This wavelength-dependent opacity allows SiO to produce significant atmospheric absorption at short wavelengths and influence atmospheric energy balance.

The absorption of stellar UV/visible flux by SiO in the upper atmosphere leads to localized heating, which can potentially create temperature inversions similar to those originally attributed to TiO/VO in hot Jupiters (Hubeny et al., 2003; Fortney et al., 2008). Recent observational non-detections of TiO and VO in several UHJs suggest that alternative absorbers, including SiO, may

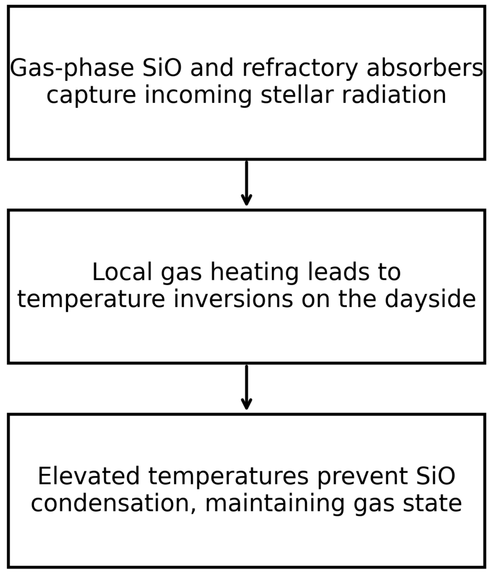

Figure 1.13: Schematic of the SiO-Driven Thermal Feedback Mechanism. The diagram outlines the feedback loop in ultra-hot Jupiter atmospheres where gas-phase SiO and other refractory absorbers capture stellar radiation, triggering localized heating and stratospheric temperature inversions. This results in higher temperatures inhibit SiO condensation to keep it in gaseous state.

be the primary contributors to these inversions (Yang et al., 2023; Nugroho et al., 2020; Johnson et al., 2022). This creates a feedback mechanism (see Figure 1.13) where SiO absorption heats the atmosphere, further preventing silicate condensation and maintaining gaseous SiO (Lothringer et al., 2018; Cont et al., 2021; Lee et al., 2022).

Conversely, if temperatures are cool enough for SiO to condense into silicate clouds, this high-altitude heating source is removed, potentially triggering a cooling feedback effect. Thus, SiO abundance acts as a diagnostic indicator of whether silicate cloud formation is active in the atmosphere. Detection of SiO (or lack thereof) at the terminator can reveal whether the atmosphere is above the thermal threshold for silicate condensation (Lothringer et al., 2021; Lothringer et al., 2025).

1.4.2 Observational Detections of Refractory Species

Over the past decade, numerous refractory species have been identified in UHJ atmospheres, confirming that heavy elements ordinarily sequestered in condensates remain vaporized. Transit and emission spectroscopy (especially at high resolution) of UHJs have revealed a diverse array of metal atoms and ions – e.g., Fe I, Fe II, Mg I, Ca II, Ti I, Na I, V I (Hoeijmakers et al., 2018, 2019; Sing et al., 2019; Ben-Yami et al., 2020; Stangret et al., 2020; Merritt et al., 2021; Silva et al., 2022; Yang et al., 2023; Borsato et al., 2023).

These detections established that UHJs can indeed be "ultra-hot" enough to sustain metals in gaseous form. Until recently, however, molecular refractory species like SiO had proven elusive. Past HST observations of UHJs showed hints of unexplained near-UV absorption, but studies often attributed these features to continuum haze or atomic species, since SiO was not included in earlier spectral models. HST/STIS and WFC3 spectra of HJs like WASP-121b and HAT-P-41b revealed excess absorption at $\sim$0.3–0.4 µm that could not be fully explained, until theoretical predictions identified SiO as the dominant high-temperature Si carrier (Lothringer et al., 2021). As discussed earlier, the first evidence for SiO came from HST/WFC3 G280 observations of WASP-178b, where atmospheric retrievals indicated that the strong NUV absorption required the presence of Si-bearing species. This finding helped establish an empirical temperature threshold for silicate condensation between approximately 1950 and 2450 K.

In parallel with space-based observations, ground-based high-resolution spectroscopy has independently detected silicon in UHJ atmospheres. Neutral silicon (Si I) was detected at 4.8–5.4σ significance in the dayside emission spectra of WASP-33b and KELT-20b via cross-correlation techniques (Cont et al., 2021). This represented the first direct identification of atomic silicon in an exoplanet atmosphere, observed as Si I emission lines originating from thermally inverted daysides. These emission features confirmed both silicon's presence in gaseous form and the existence of stratospheric inversions (since emission lines imply a hot layer above a cooler deeper atmosphere). Together, these discoveries in transmission and emission spectroscopy have supported the view that refractory elements like silicon are accessible in UHJ spectra.

1.4.3 Challenges in Detecting SiO

Identifying SiO in exoplanet spectra has proven difficult due to both observational and modeling constraints, particularly in the near-ultraviolet (NUV) where SiO's strongest features reside. From an observational perspective, accessing the NUV is intrinsically challenging. The Earth's atmosphere becomes opaque below $\sim$300 nm because of strong ozone (O_3) absorption, alongside Rayleigh scattering and absorption by O_2 and N_2 (Meier, 1991). Even from space, NUV measurements rely almost exclusively on the Hubble Space Telescope, whose STIS and COS instruments provide limited spectral coverage and often modest signal-to-noise ratios due to technological constraints and finite exposure times (Woodgate et al., 1998; Green et al., 2012).

Stellar flux in the near-UV is also relatively low (particularly for cooler host stars), which makes it challenging to extract precise transit depths in this regime. Even for an A-type star like WASP-178, the UV flux can be orders of magnitude lower than optical flux, increasing photon noise and measurement uncertainties. Precisely isolating SiO's contribution in this regime demands broad spectral coverage and high-quality data to disentangle it from other potential opacity sources.

The modeling hurdle arises from degeneracies among multiple species that absorb in the NUV and blue optical regions (Fossati et al., 2010; Sing et al., 2019). Metal ions (e.g., Fe^+, Mg^+, Ti^+) can produce resonance lines or photoionization continuum absorption, creating opacity slopes or cutoffs that can mimic SiO signatures. Early retrievals often attributed excess NUV absorption to these metal ions or Rayleigh-like slopes from hazes, since SiO was not initially considered a candidate opacity source (Sing et al., 2011a; Sing et al., 2019). As a result, any true SiO signal could be blended or misidentified. For instance, until 2022, the large NUV absorption in WASP-121b's spectrum was unexplained by models that neglected SiO, leading to speculation about extreme haze or unidentified ions (Evans et al., 2018).

SiO's unique spectral features also complicate detection efforts. Its strongest UV transitions stem from electronic excitations that appear as broad band-like absorptions rather than discrete, narrow lines. These broad depressions in the transit spectrum can be difficult to distinguish from instrumental systematics or stellar activity, requiring sophisticated detrending methods (Wakeford et al., 2016). In contrast, SiO's vibrational-rotational transitions at optical and infrared wavelengths are much weaker—its UV opacity can exceed IR opacity by a factor of 10^4 under typical hot-Jupiter conditions (Sharp & Burrows, 2007; Barton et al., 2013; Lothringer et al., 2025). Consequently, SiO can be prominent in the NUV yet remain undetected in IR observations of the same planet (Lothringer et al., 2025).

1.4.4 Exomol SiOUVenIR Line List

Accurate molecular line lists are critical for interpreting high-temperature exoplanet spectra. Older rovibronic dataset for SiO, such as the Kurucz line list (Kurucz, 2011), omit many high-energy transitions and lack the wavelength precision needed for modern high-resolution work. The newly published SiOUVenIR database (Yurchenko et al., 2021) overcomes these gaps by treating an expanded set of electronic states of $^{28}Si^{16}O$; it includes both radiatively active levels and additional states that influence the spectrum through electronic coupling. The line list was validated against 2617 experimentally measured energy levels and includes numerous transitions previously omitted from spectroscopic databases.

SiOUVenIR extends SiO opacity data down to 140 nm, which is well into the UV regime that shapes UHJ thermal profiles. It includes additional electronic states and rovibronic couplings absent from earlier ExoMol releases such as EBJT (Barton et al., 2013), yielding stronger and more accurate band-head predictions. This improved accuracy and completeness enable robust cross-correlation and retrieval analyses of SiO in high-temperature exoplanet spectra.

The advancements of this new line list are evident in Figure 1.14: the SiOUVenIR spectrum matches laboratory data across the UV and shows much finer details. Figure 1.15 presents the temperature dependence of SiO spectral features, with higher temperatures populating additional energy levels and broadening absorption features. Finally, Figure 1.16 compares individual SiOUVenIR lines with fluorescence and shock-tube measurements, confirming that the new wavelengths and intensities fall within experimental uncertainties.

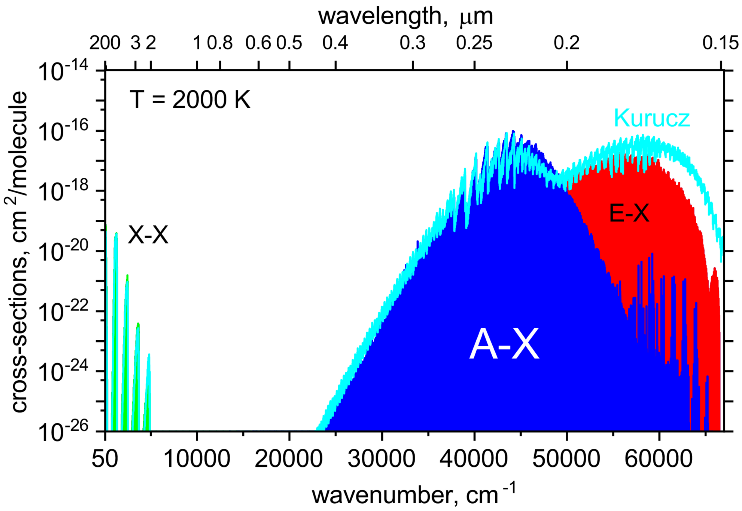

Figure 1.14: Absorption cross-sections of SiO at 2000 K across a broad wavelength range. The spectrum computed using the SiOUVenIR line list is shown in three colors representing different electronic transitions: blue (A-X band, dominant in the UV/visible range), red (E-X band, at higher wavenumbers), and green (X-X band, at lowest wavenumbers). The cyan line shows data from Kurucz (2011) for comparison. Note the significant differences in the ultraviolet region (wavenumbers > 30,000 cm^{-1}), where the SiOUVenIR data shows stronger and more structured absorption features. Both spectra were computed using a Gaussian profile with an HWHM of 1 cm^{-1}. Figure from Yurchenko et al. (2021).

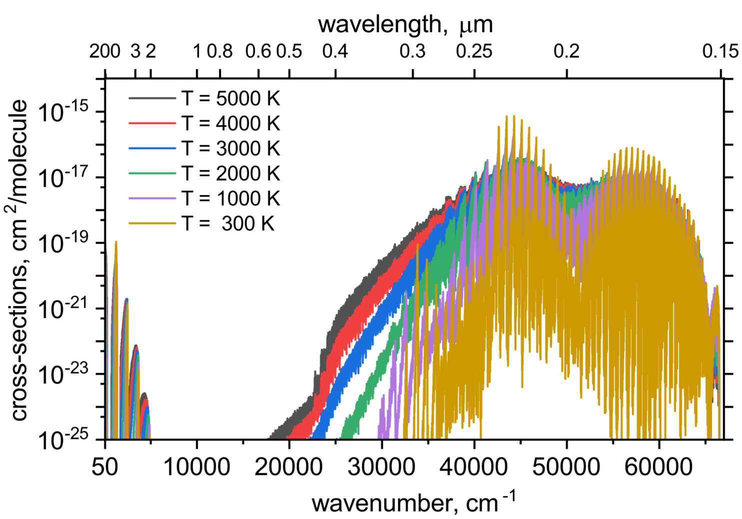

Figure 1.15: Temperature evolution of SiO absorption cross-sections from 300 K (blue) to 2000 K (red) as modeled by the SiOUVenIR line list. Higher temperatures lead to increased population of excited vibrational and rotational states, resulting in broader absorption features and enhanced opacity at shorter wavelengths. The spectra were generated with a Gaussian line shape (HWHM = 1 cm^{-1}). Figure from Yurchenko et al. (2021).

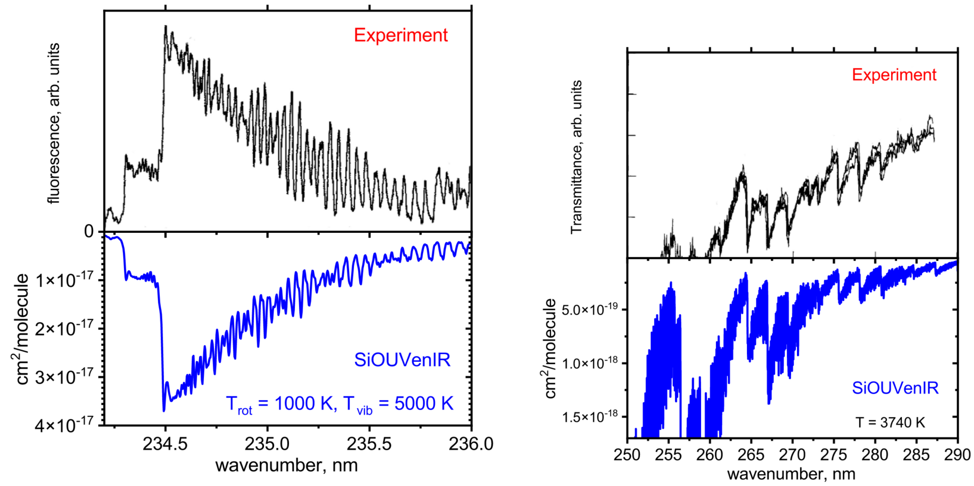

Figure 1.16: Validation of SiOUVenIR UV absorption features against experimental data. **Left panel:** Comparison of calculated SiO absorption (at $T_{rot} = 1000\,K$ and $T_{vib} = 5000\,K$) with fluorescence measurements from Coursimault et al. (2003). **Right panel:** Comparison of calculated SiO spectrum (at T = 3740 K) with shock-tube absorption data from Park & Arnold (1978). Both calculated spectra use Voigt profiles with appropriate line widths. The good agreement between modeled and measured spectra confirms the reliability of the line list for ultraviolet applications. Figure from Yurchenko et al. (2021).

The SiOUVenIR line list is available through the ExoMol project[2] and the CDS database[3]. Its extended 140 wavelength coverage and high-temperature line data supply the near-UV SiO opacities missing from older catalogues, making it possible for us to detect high resolution SiO features in the spectrum of WASP-178b with high accuracy.

1.5 Scientific Motivation and Research Objectives

1.5.1 Current Gaps in Existing Research

Previous evidence for SiO in WASP-178b's atmosphere comes only from broad UV absorption features in low-resolution HST/STIS/WFC3 data (Lothringer et al., 2021). This detection remains tentative as other atmospheric constituents (e.g., Fe II, Mg II, or metal oxides) could produce similar broad absorption patterns. The distinctive molecular bandhead structure of SiO which would provide conclusive evidence cannot be resolved at these low resolutions, leaving the identification

[2] https://www.exomol.com
[3] https://cdsarc.u-strasbg.fr/viz-bin/qcat?J/MNRAS/

ambiguous.

Current high-resolution spectroscopic techniques that have revolutionized exoplanet atmosphere characterization remain underutilized for SiO detection. Cross-correlation methods have successfully identified numerous atomic and molecular species in UHJ atmospheres, including Fe, Ti, Mg, Ca, Cr, V, and OH (Hoeijmakers et al., 2019; Stangret et al., 2020; Mollière et al., 2022; Yang et al., 2023). These techniques excel at isolating specific spectral features from complex atmospheric signals and distinguishing them from telluric and stellar contamination. More recently, statistical approaches like the in-band / out-of-band technique (detailed in Section 3.2) have been developed to detect molecular absorption features at medium resolution (Grant et al., 2023). This method provides a powerful statistical framework for direct detection of molecular species by comparing wavelengths containing strong absorption features with adjacent continuum regions. However, application of these techniques to SiO in the challenging near-UV spectral region has not been systematically attempted, which leaves a significant methodological gap in the literature.

The lack of high-resolution SiO cross-sections optimized for the extreme temperature of UHJ also presents a challenge, as robust detection of a molecule relies on accurate molecular opacity data. Until the recent publication of comprehensive SiO line lists from ExoMol (Yurchenko et al., 2021), atmospheric models relied the older rovibronic data from Kurucz (2011) which was not optimized for ultra-hot conditions or near-UV transitions.

1.5.2 Research Objectives

This thesis aims to develop a robust framework for detecting silicon monoxide (SiO) in ultra-hot Jupiter (UHJ) atmospheres, providing the first systematic methodology for identifying this important molecular absorber in near-UV transmission spectra. Our approach integrates advanced spectroscopic techniques (Sing et al., 2019), state-of-the-art SiO opacity data from the ExoMol SiOUVenIR line list (Yurchenko et al., 2021), and in-band/out-of-band statistical analysis methods adapted from high-resolution CO detection studies (Grant et al., 2023). We benchmark this methodology using archival HST/STIS/E230M observations of the ultra-hot Jupiter WASP-178b.

Detecting SiO at $T_{eq} \geq 2200$K will clarify whether silicate vapors significantly contribute to stratospheric temperature inversions in UHJs. Our statistical pipeline for detrending visit-long systematics in HST/STIS near-UV data maximizes signal-to-noise ratios and provides a framework adaptable to similar archival datasets of other UHJs. This methodology can be extended to detect both SiO and additional refractory species in UHJ atmospheres, and will complement upcoming JWST and ELT observational campaigns targeting the atmospheres of the hottest known exoplanets. Ultimately, this work will enable more systematic comparisons of thermal profiles and chemical abundances across a range of UHJs, adding to our understanding of these extreme planetary environments.

1.6 Thesis Structure and Overview

This thesis is organized as follows. Section 2 describes the HST STIS observations and the data reduction pipeline, including the application of the jitter decorrelation method to correct systematic errors. In Section 3, we explain our approach for identifying SiO spectral features in high-resolution data, including the adaptation of the in-band/out-of-band statistical technique. We present our transmission spectrum analysis in Section 4, where we apply this methodology to identify SiO absorption features with high statistical confidence. Section 5 discusses the broader implications of our findings for WASP-178b's atmospheric composition and thermal structure, comparing results with theoretical models. Finally, Section 6 summarizes our key results and suggests directions for future research.

2 Observation and Data Reduction

2.1 Observational Data for WASP-178b

The transit observations of WASP-178b were conducted on 30 July 2020 using HST/STIS E230M (program 16086, PI: Lothringer). The NUV-Multi-Anode Microchannel Array (NUV-MAMA) detector with E230M echelle grating (centered at 2707 Å) and 0.2" × 0.2" aperture provided spectra with $R = \frac{\lambda}{\Delta\lambda} = 30{,}000$ across 2280-3070 Å. The 23 spectral orders have a dispersion of 0.049 Å per pixel (∼2 pixels per resolution element). The data used in this study are publicly available through the Mikulski Archive for Space Telescopes (MAST)[4].

The observational sequence consisted of five consecutive HST orbits, capturing the entire transit with additional baseline before and after. The first orbit provided seven sub-exposures, while subsequent orbits yielded ten each, totaling 47 sub-exposures. Target acquisition used STIS ACQUIRE mode to center the star in the aperture.

Initial data reduction employed `calstis` pipeline v3.4.2, which performed standard calibration steps: data quality checks, dark subtraction, flat-fielding, wavelength calibration, 1D extraction, background removal, heliocentric correction (25.32 km/s), and flux calibration. Additional echelle-specific processing included scattered light removal and ripple correction. A detailed description of all calibration steps is provided in Appendix E. The pipeline produced wavelength and flux-calibrated 1D spectra for each order.

Figure 2.1 shows the mean time-series spectra and the corresponding mean signal-to-noise ratio (S/N) for the observations. The fully reduced spectra shows decreasing flux toward shorter wavelengths, accompanied by a clear reduction in S/N at both the blue and red extremes of the spectral coverage. The stellar spectrum of WASP-178 shows prominent features of the Mg II doublet around 2800 Å, as shown in Figure 2.2.

[4] https://mast.stsci.edu/portal/Mashup/Clients/Mast/Portal.html

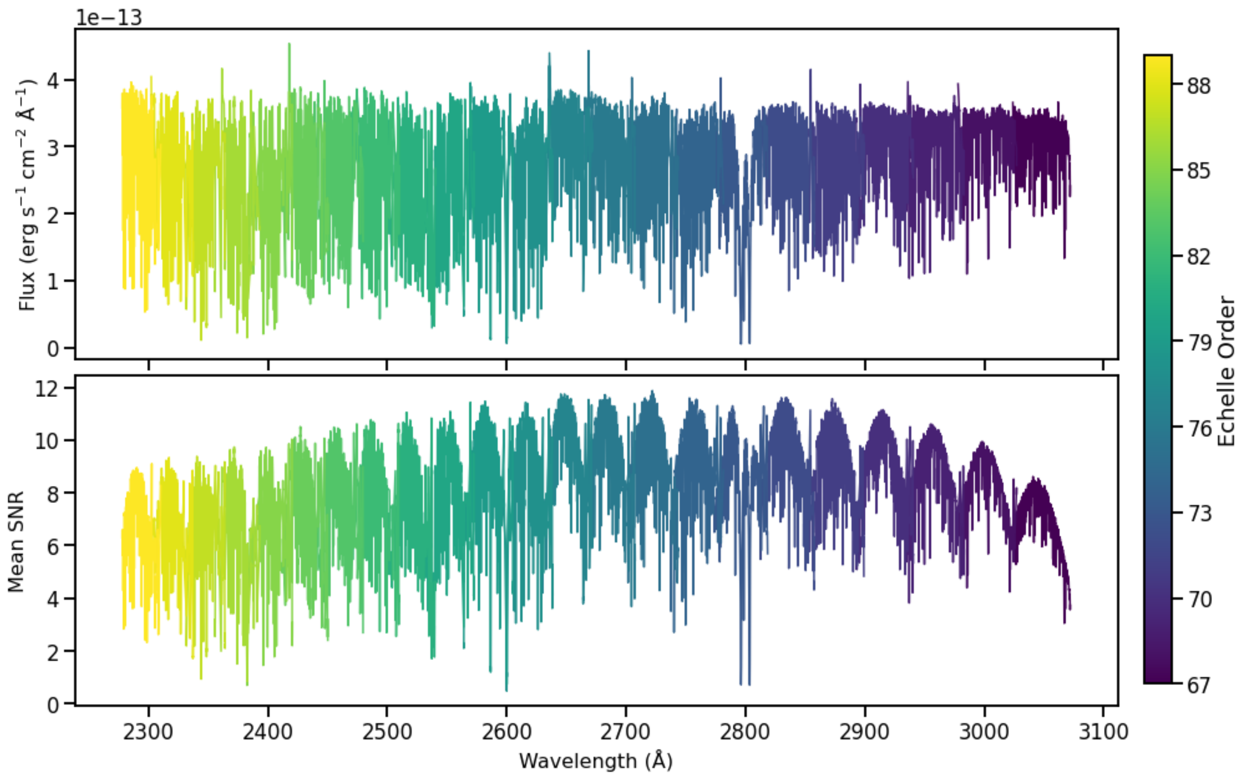

Figure 2.1: **Top panel:** Mean time-series spectra of WASP-178b observed with HST/STIS E230M, constructed after bad pixel removal. The spectrum is color-coded by echelle order (see color bar). **Bottom panel:** Corresponding mean signal-to-noise ratio (S/N) by echelle order. The S/N is influenced by both instrumental sensitivity and the stellar flux distribution, resulting in decreased S/N toward both the blue and red edges of the detector.

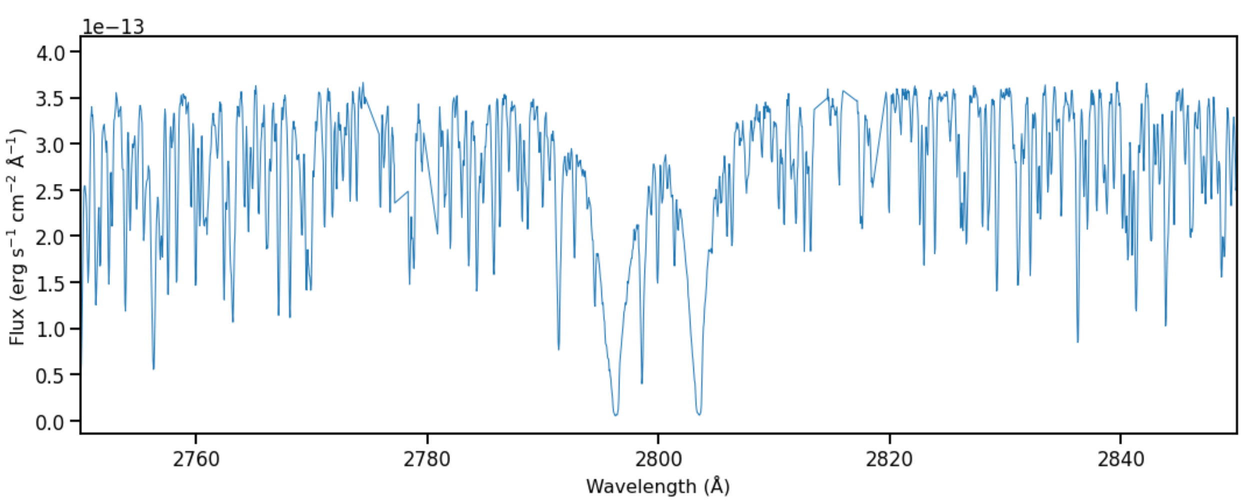

Figure 2.2: Zoom-in of the mean spectrum (Figure 2.1, top panel) around the Mg II doublet region (∼2800 Å).

Parameter	Value
Observation Details	
Target	WASP-178b
Observation date	July 30, 2020 (PI: Lothringer)
Instrument	HST/STIS E230M, NUV-MAMA
Aperture	0.2" × 0.2"
Grating setting	2707 Å
Wavelength range	2280–3070 Å
Resolving power	∼30,000
Number of echelle orders	23
Observation orbits	5 consecutive orbits
Exposure time	268s per frame
Sub-exposures	First orbit: 7, Others: 10 each, Total: 47
Data Reduction	
Data reduction pipeline	`calstis` version 3.4.2
Calibration steps	Dark/flat-field correction, 1D extraction
	background subtraction, flux calibration
Output units	$\mathrm{erg\,s^{-1}\,cm^{-2}\,\AA^{-1}}$

Table 3: Summary of HST/STIS NUV Observations of WASP-178b

2.2 Systematics correction

Our data analysis closely follows Sing et al. (2019). First, we created a white light curve by integrating flux across all echelle orders to characterize instrumental systematics using jitter decorrelation. We then applied this systematics model to spectroscopic light curves at different wavelength bin sizes through common-mode analysis. This approach uses the white light systematics (with higher signal-to-noise) as a template to correct wavelength-dependent light curves, allowing us to extract clean transmission spectra at desired resolutions.

2.2.1 Jitter Decorrelation

HST/STIS spectroscopic observations suffer from instrumental systematics caused by telescope pointing fluctuations, or "jitter". These instabilities introduce correlated noise into light curves that can mask astrophysical signals during transit or eclipse observations. Raw light curves typically show both long-term trends across entire visits and short-term variations matching HST's orbital period (Brown et al., 2001). The significant ramping effects visible in Fig. 2.3 result primarily from telescope thermal "breathing", the cyclical expansion and contraction of components due to temperature changes and slight drifts in Fine Guidance Sensor (FGS) alignment.

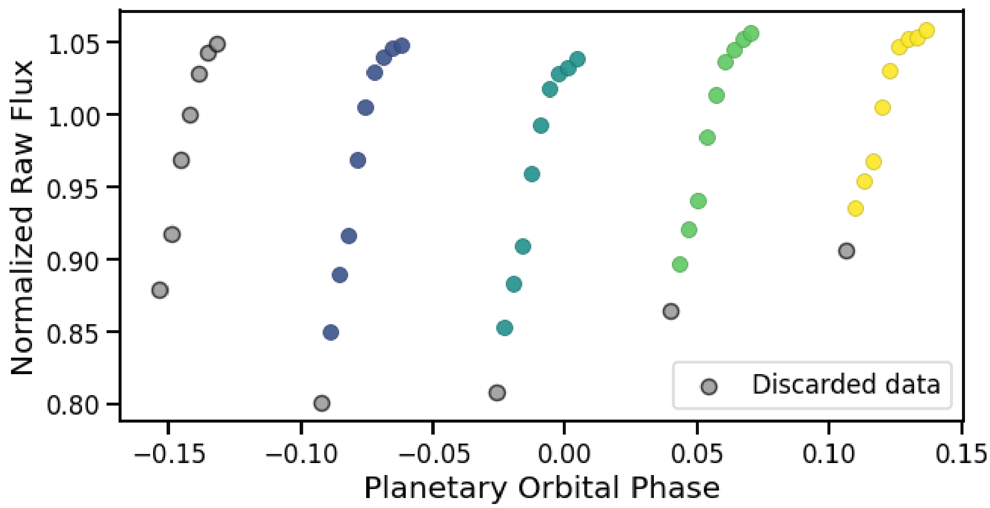

Figure 2.3: Raw white light curve of WASP-178b observed with HST/STIS/E230M. Points are color-coded by HST orbit, with gray markers indicating discarded exposures not included in the final light curve fitting (the first orbit and first sub-exposures of each orbit).

To monitor and quantify these pointing variations, the HST Engineering Data Processing System (EDPS) produces "jitter files" for each observation. These files consist of 3-second averaged records of key spacecraft parameters, including roll angle variations, pointing offsets, and guide star alignment metrics. Those engineering data provide a detailed account of the telescope's pointing behavior, thereby can be used as a foundation for the identification and correction of systematic errors.

Following Sing et al. (2019), we incorporate selected jitter parameters as regressors within a polynomial decorrelation framework to mitigate flux variations induced by pointing fluctuations. For example, slight drifts in pointing can result in slit losses or shifts in the instrument's point-spread function (PSF), producing time-correlated flux variations. In addition to the 20 jitter parameters provided by the EDPS (see Table 4), we include the HST orbital phase (ϕ_{HST}) as part of the full set of detrending regressors.

Parameters	Meaning
v2_dom	Dominant guide star V2 coordinate
v3_dom	Dominant guide star V3 coordinate
v2_roll	Roll FGS V2 coordinate
v3_roll	Roll FGS V3 coordinate
si_v2_avg	Mean of jitter in V2 over 3 s
si_v2_rms	RMS of jitter in V2 over 3 s
si_v2_p2p	Peak-to-peak jitter in V2 over 3 s
si_v3_avg	Mean of jitter in V3 over 3 s
si_v3_rms	RMS of jitter in V3 over 3 s
si_v3_p2p	Peak-to-peak jitter in V3 over 3 s
ra	Right Ascension of aperture reference
dec	Declination of aperture reference
roll	Position angle between north and +V3 axis
limbang	Angle between V1 axis and Earth limb
los_zenith	Angle between HST zenith and target
mag_v1	Magnetic field along V1
mag_v2	Magnetic field along V2
mag_v3	Magnetic field along V3
lat	HST's latitude
long	HST's longitude

Table 4: Details of the jitter engineering parameters used in the study.

Detrending parameter and degree selection To robustly determine the optimal systematic correction model while avoiding overfitting, we iteratively introduce potential detrending parameters into our white light curve fit. We start by analyzing the correlation between HST engineering parameters (jitters) and the STIS white-light-curve photometry using the out-of-transit data (see Figure 2.4). This analysis allows us to identify the parameters most strongly correlated with flux variations, which become candidates for our systematics model.

Based on the correlation analysis, the parameter `Mag_V3` (magnetic field along the V3 axis) exhibits the highest positive correlation, with a coefficient of approximately 0.9, indicating that increases in this parameter are strongly associated with higher out-of-transit flux. Conversely, `Longitude` shows the strongest negative correlation suggesting that longitudinal drift of HST's position reduces the observed flux, likely due to misalignment of the target within the narrow slit.

Further inspection of the telescope pointing over time (Figure 2.5) reveals significant drifts in multiple pointing parameters across the five HST orbits covering the transit event. Particularly concerning are the large drifts in right ascension (RA) and declination (DEC), which show marked differences between in-transit positions and out-of-transit positions (first and last orbits). These positional shifts relative to the small 0.2"×0.2" slit likely induce substantial slit light losses that correlate with the transit event itself, potentially contaminating the astrophysical signal. Additional concerns include rotational drifts in `V2_roll` and `V3_roll`, which may alter the target's orientation within the slit, further contributing to systematic flux variations.

Based on this analysis, we exclude the first orbit and the initial exposure of each subsequent orbit from our analysis, following standard practice for HST/STIS exoplanet transit observations (Sing et al., 2011b). These discarded exposures consistently display lower flux levels symptomatic of pronounced systematic errors, likely due to thermal settling or initial pointing inaccuracies following telescope repointing.

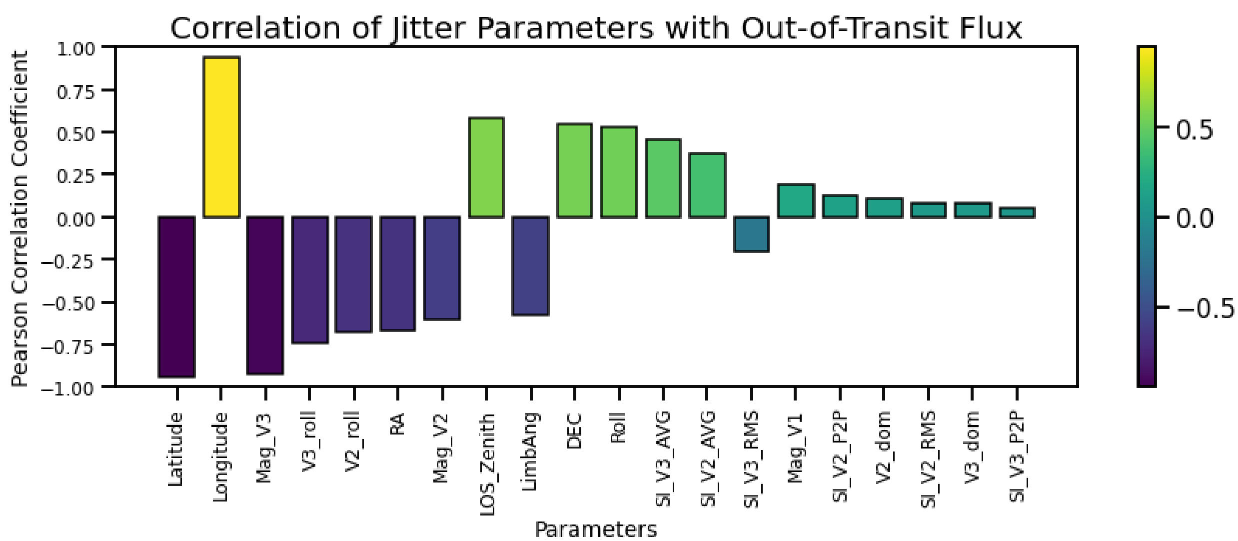

Figure 2.4: Pearson correlation coefficients between HST engineering (jitter) parameters and out-of-transit flux measurements for WASP-178b. The color scale indicates correlation strength, with yellow representing strong positive correlations and dark purple representing strong negative correlations. Notable parameters include `Mag_V3` (strongest positive correlation, ∼0.9) and `Longitude` (strongest negative correlation, ∼-0.9), indicating that telescope position and orientation significantly impact the measured flux through the narrow slit. These highly correlated parameters are primary candidates for detrending.

Each selected jitter parameter is then modeled using a first-degree polynomial to assess its ability to reduce the residuals. To quantitatively evaluate the improvement in the model, we compute the

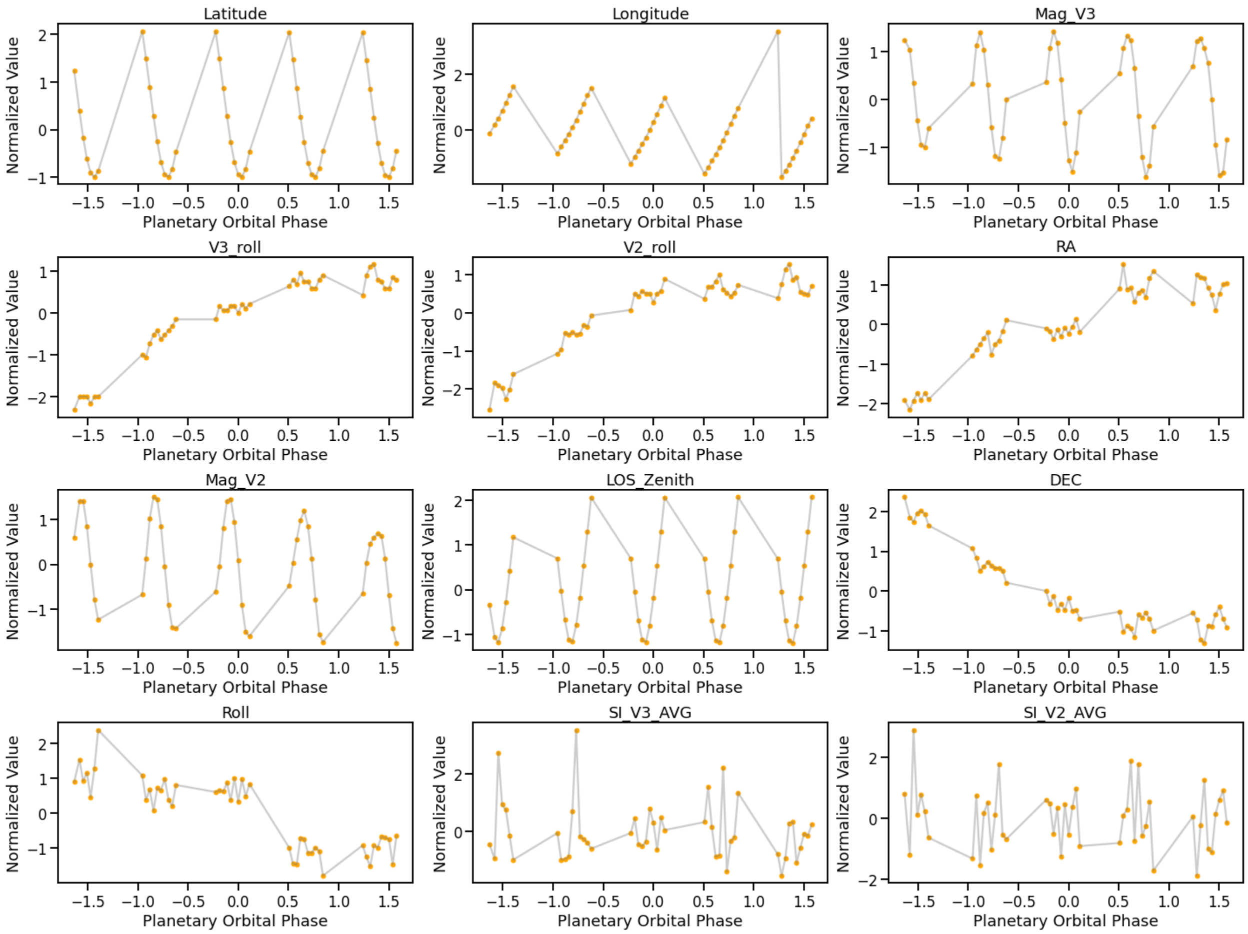

Figure 2.5: Temporal evolution of key HST pointing parameters as a function of planetary orbital phase during the WASP-178b transit observation. Each panel shows a different engineering parameter (normalized to zero mean and unit variance) plotted against orbital phase, with negative phases corresponding to pre-transit observations and positive phases to post-transit observations. Several parameters (`V3_roll`, `V2_roll`, `RA`, `DEC`) show significant drift trends across the observation, while others (`Latitude`, `Longitude`, `Mag_V3`) display periodic variations with HST's 96-minute orbital cycle. The systematic differences between pre-transit, in-transit, and post-transit pointing highlights the need for careful detrending to separate instrumental effects from the planetary signal.

corrected Akaike Information Criterion (AICc), defined as:

$$\mathrm{AIC_c} = \mathrm{AIC} + \frac{2k^2 + 2k}{n - k - 1}, \tag{5}$$

$$\mathrm{AIC} = \chi^2 + 2 \times k, \tag{6}$$

where k is the number of free parameters, n is the number of data points (exposures), and χ^2 is the chi-squared statistic of the fit measuring how well observed data matches the model. Due to our small effective sample size of only 36 exposures, the use of AICc instead of the classical AIC or BIC is preferred as it includes a correction for small sample sizes.

A parameter is incorporated into the systematic correction model only if its inclusion results in a decrease in AICc relative to the baseline fit. Once a parameter is tested to be significant, we further refine its representation by fitting its correlation with the residuals using an incremental polynomial expansion. The systematic correction term is modeled as

$$S(X) = \prod_{i=1}^{N} S_i(x_i), \tag{7}$$

$$S_i(x_i) = 1 + a_1 x_i + a_2 x_i^2 + \cdots + a_n x_i^n. \tag{8}$$

where x_i denotes the detrending variable and the coefficients $a_1, a_2, \ldots, a_n$ are fitted parameters. For each candidate jitter parameter, we incrementally increase the polynomial degree n and re-assess the model's AICc. If an increase in polynomial degree continues to lower the AICc, the higher degree is retained; however, if no further improvement is observed (or if a subsequent increase yields a worse AICc), the lower degree is preferred. In some cases, even if an intermediate degree does not result in an AICc improvement, we may test higher degrees (i.e., $n+1$) as an alternative to ensure that the global minimum of the AICc is reached.

This procedure is applied sequentially: each time a parameter (and its optimal polynomial degree) is confirmed to improve the model, it is incorporated into the overall systematic correction, and the remaining candidate parameters are re-evaluated. The process is iterated until no further AICc improvement is observed. The WASP-178b NUV data requires a complex systematics model with 10 detrenders: polynomial degree of 3 for $\phi_{\rm HST}$, a linear time trend, and first-order corrections for 6 jitter parameters including Latitude, Longitude, Mag_v2, Mag_v3, LOS_Zenith, and LimbAng.

2.2.2 White Light Curve Fitting

We construct the white light curve by integrating the stellar flux over the entire observed wavelength range and subsequently normalizing each visit's light curve with respect to its median flux. The transit was modeled using the `batman` package (Kreidberg, 2015). Following Sing et al. (2019), the observed flux $f(t)$ is represented as

$$f(t) = T(t,\theta) \times F_0 \times S(X), \tag{9}$$

where $T(t,\theta)$ is the theoretical transit model characterized by the transit parameters θ, F_0 is the total baseline flux, and $S(X)$ is the systematic error correction model. The free parameters in the fitting procedure included the planet-to-star radius ratio (R_p/R_*), the polynomial coefficients encapsulating the systematic trends, and the baseline flux F_0. We employed a linear limb-darkening law with the coefficient fixed at $u = 0.7758$, as predicted by the PHOENIX models (Lothringer et al., 2021). The mid-transit time, orbital inclination, and the scaled semi-major axis were held fixed to the values from literature (Table 5) since the HST NUV data did not adequately sample the ingress and egress, limiting the precision with which these parameters could be constrained.

Orbital Parameters	
Inclination (i)	$84.41 \pm 0.20^\circ$
$a/R_\star$	6.588 ± 0.091
Transit Center (T_0)	$2459097.869279 \pm 0.00014$ days
Orbital Period (P)	3.3448285 ± 0.0000012 days
Planet Radius ($R_p/R_\star$)	0.11295150 ± 0.00041

Table 5: Orbital parameters of WASP-178b used in the fit, table adapted from Lothringer et al. (2021)

Following (Sing et al., 2019), we initially set the errors on each data point to the pipeline values, which are predominantly photon noise. We determined the best-fitting parameters simultaneously using a Levenberg-Marquardt least-squares algorithm (Markwardt, 2009). After the initial fit, we rescaled the uncertainties for each data point to match the standard deviation of the residuals. The final white light curve fit yielded a planet-to-star radius ratio of $R_p/R_\star = 0.123^{+0.0113}_{-0.0100}$. This light curve fitting process improves the precision by a factor of 10.8 (residual RMS lowered from 0.061 to 0.0056) and is consistent with the value 0.1244 ± 0.0050 reported by Lothringer et al. (2021). The uncertainties on the fitted parameters were calculated using the covariance matrix from the Levenberg-Marquardt algorithm, which assumes the probability space around the best-fit solution follows a multivariate Gaussian distribution.

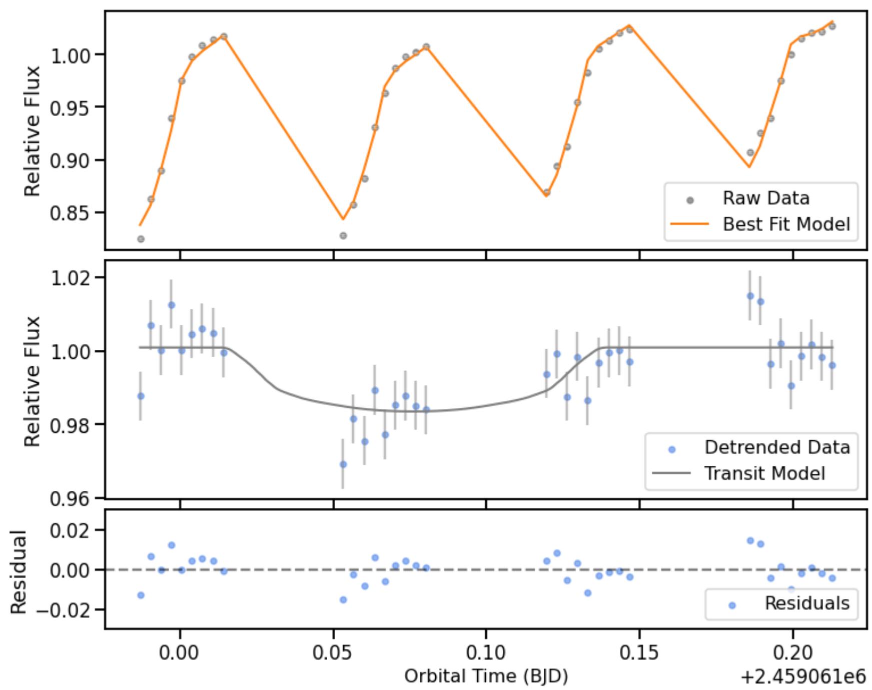

Figure 2.6: WASP-178b White Light Fit: Top: normalized raw light curves(grey) and best fit model(orange). Middle: flux corrected from systematic errors and fitted with a `batman` transit model. Bottom: residuals between the corrected flux and the best-fit model

Figure 2.6 presents the final results of the white light curve fitting. The top panel shows the raw, normalized light curve (plotted in grey) along with the best-fit model (in orange). The middle panel shows the detrended light curve with the transit model overlaid, and the bottom panel shows the residuals of the fit.

2.2.3 Spectroscopic light curve fitting

To extract the transmission spectrum, we fixed the system parameters that are not expected to vary with wavelength (e.g., mid-transit time, orbital period, scaled semi-major axis, and inclination) to their values used in the white light curve analysis. A common-mode correction is constructed by dividing the best-fit analytic white light curve model by a polynomial constructed from selected jitter correlation parameters. This correction model, $S(X)$, is subsequently applied as a multiplicative factor to all individual spectroscopic light curves to remove common-mode systematics.

Each spectroscopic light curve is then modeled similar to the process described in Section 2.2.2. The planet-to-star radius ratio, $R_p/R_\star$, is treated as a free parameter, while the remaining transit parameters are held fixed. The final fit yields both the best-fit value of $R_p/R_\star$ for each wavelength channel and the associated uncertainties.

Binning and Error Propagation To balance signal-to-noise with spectral resolution, we binned our data at three scales: broadband (200 Å) and narrowband (4 Å) following the selection criteria of Sing et al. (2019), and native resolution (0.1 Å) for detecting SiO absorption features.

Within each bin we average the flux:

$$\bar{f} = \frac{1}{N}\sum_{i=1}^{N} f_i, \tag{10}$$

and propagate the uncertainties by summing the variances and scaling by the number of points:

$$\sigma_{\bar{f}} = \frac{\sqrt{\sum_{i=1}^{N}\sigma_i^2}}{N}. \tag{11}$$

This procedure ensures that the uncertainties reflect both the intrinsic noise of the individual measurements and the effects of binning. Bins containing no in-transit signal are discarded, ensuring that the final transmission spectrum is built only from statistically meaningful data. The binned fluxes and errors are then modeled with the same transit formalism applied to the white-light curve.

Doppler Shift Correction To analyze spectral features in an exoplanet's rest frame, we account for Doppler shifts from both spacecraft motion and stellar systemic velocity. The Doppler effect shifts observed wavelengths $\lambda_{\rm obs}$)according to:

$$\lambda_{\rm obs} = \lambda_{\rm rest}\left(1 + \frac{v_\star}{c}\right), \tag{12}$$

where v is the radial velocity (positive for redshift, negative for blueshift) and c is the speed of light. For small velocities ($v \ll c$), the wavelength shift ($\Delta\lambda$) can be approximated as:

$$\Delta\lambda \approx \frac{v}{c}\lambda. \tag{13}$$

The STIS data reduction pipeline automatically applies heliocentric correction (`HELCORR`) using the provided velocity of +25.32 km/s, shifting the spectrum to the heliocentric frame. It also accounts for HST's orbital motion ($\pm 7.5\,$km/s) through the `DOPPCORR` step, which corrects Doppler smearing in 2D spectral calibration using dynamic darks and flats. The only correction we need to make is WASP-178's systemic velocity of $v_\star \approx -23.9\,$km/s (Hellier et al., 2019), which blueshifts its spectral features relative to the heliocentric frame. At 2400Å, this corresponds to:

$$\Delta\lambda \approx \left(\frac{23.9}{3\times 10^5}\right) \times 2400 \approx 0.19\,\text{Å}. \tag{14}$$

As $\Delta\lambda$ scales linearly with λ, the required correction grows across the bandpass. At the native HST/STIS/E230M sampling of 0.10 Å pixel^{-1}, a 0.19 Å shift spans almost 2 detector pixels, which is more than enough to blur or misplace narrow atmospheric features (shown in Figure 2.7. We therefore apply this Doppler correction to every spectral channel before further analysis.

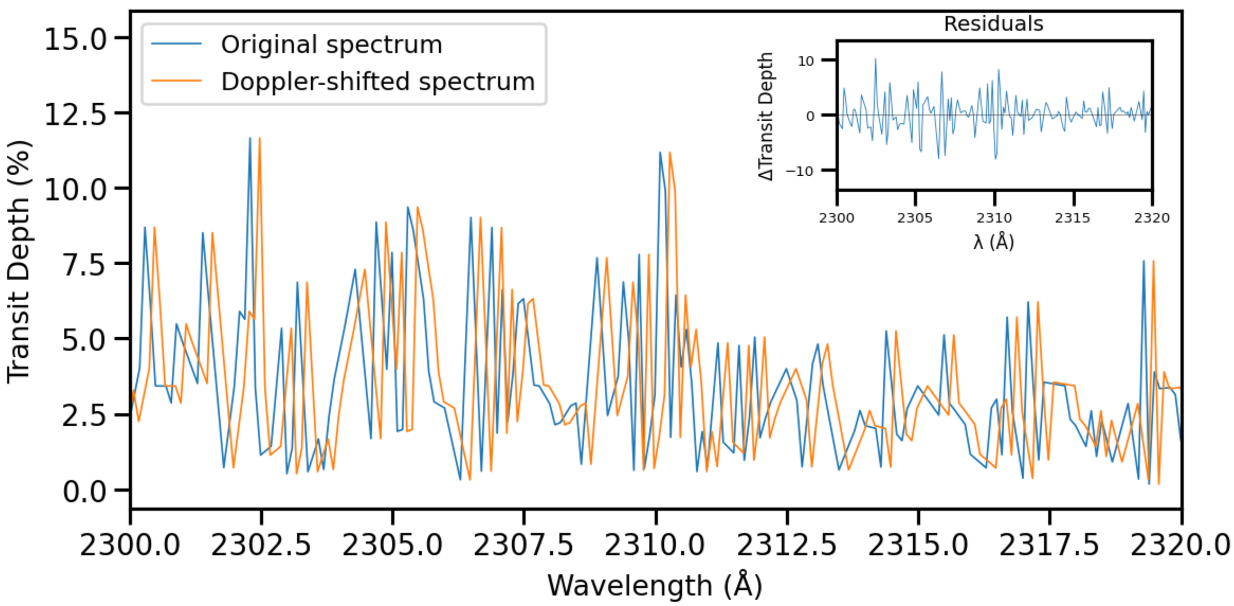

Figure 2.7: Comparison of WASP-178b's transmission spectrum before (blue) and after (orange) applying the doppler shift correction. The inset shows residuals between the original and corrected spectra in the selected region.

3 Detecting SiO in Transmission Spectra

To target SiO absorption in WASP-178b's atmosphere, we first examine the high-resolution line list for SiO (Yurchenko et al., 2021) to identify candidate absorption features, then carefully select in-band and out-of-band regions in the transmission spectrum for statistical comparison. The goal is to contrast wavelengths where strong SiO absorption is predicted against those with minimal SiO absorption, based on theoretical molecular cross-sections. We adapt the in-band/out-of-band methodology developed by Grant et al. (2023) for CO detection in JWST/NIRSpec data, and apply it here to search for SiO features in HST/STIS observations.

The methodology breaks down as follows. First in Section 3.1, we identify the peak absorption features of SiO by processing the line list into high-resolution cross-sections at WASP-178b's equilibrium temperature. Next, in Section 3.2, we classify spectral regions as either "in-band" (strong SiO absorption) or "out-of-band" (adjacent continuum), with adjustments for our data resolution and wavelength coverage. We then apply these spectral masks to our observed data and calculate the statistical properties of each sample. Finally, we employ Welch's one-tailed t-test to determine whether the mean transit depth in SiO in-band regions significantly exceeds that of out-of-band regions, which would indicate a detection of SiO absorption.

3.1 Identifying SiO Peak Absorption Features from Line List

We use `ExoCross` (Yurchenko et al., 2018), a Fortran computational tool to generate high-resolution SiO absorption cross-sections under the atmospheric condition of WASP-178b. Our approach involves preparing input parameters matching HST/STIS wavelength coverage and resolution, computing theoretical SiO cross-sections at WASP-178b's equilibrium temperature, and identifying the strongest absorption features.

We focus on the wavelength window of 2280-3000 Å, corresponding to our STIS E230M data coverage except the very edge regions. Using equation 15, we convert this to the wavenumber range required by `ExoCross` (32573–43860 cm^{-1}).

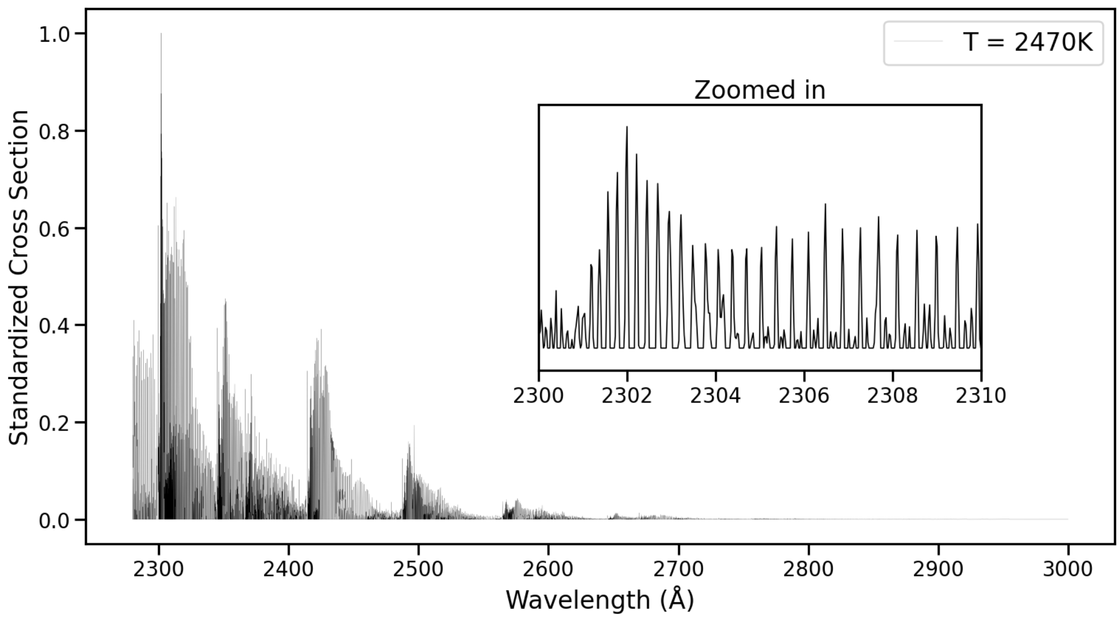

Figure 3.1: Simulated absorption spectrum of SiO at 2470 K (WASP-178b's equilibrium temperature) generated from the SiOUVenIR line list. The main panel shows the full wavelength range covered by our HST/STIS observations (2280–3000 Å), with cross-sections normalized to the maximum value. The strongest absorption features are concentrated at shorter wavelengths (<2500 Å), with diminishing strength toward longer wavelengths. The inset provides a high-resolution view of the 2300–2310 Å region, showing the dense forest of individual rotational-vibrational lines that create the distinctive band structure. These detailed spectral features would be partially resolved in high-resolution observations and provide a unique fingerprint for SiO detection.

$$\lambda\,(\text{Å}) = \frac{10^8}{\tilde{\nu}\,(\text{cm}^{-1})}. \tag{15}$$

where $\tilde{\nu}$ is the wavenumber in cm^{-1}. The SiO absorption cross-section was generated at $T = 2470$ K (WASP-178b's equilibrium temperature) with a spectral resolution matching the instrument ($R \sim 30,000$). Detailed information about the input file structure, compilation commands, and technical parameters used is provided in Appendix F.

Figure 3.1 shows the resulting spectrum. The strongest SiO bands lie shortward of 2500 Å and consist of thousands of closely spaced lines that HST/STIS partially resolves. These model cross-sections form the templates against which we match the observed transmission spectrum in the subsequent in-band/out-band analysis.

3.2 In-band/Out-of-band Technique from Grant et al. (2023)

3.2.1 Overview of Methodology

We adapt the statistical method developed by Grant et al. (2023), which successfully detected carbon monoxide in WASP-39b using JWST data by leveraging molecular band-head patterns. This approach amplifies the collective signal from multiple spectral lines, enabling detection even when individual features are too weak to isolate.

The method categorizes spectral wavelength bins into two groups: "in-band" regions where molecular absorption is predicted to be strongest, and "out-of-band" regions representing adjacent continuum areas. By comparing average transit depths between these wavelength sets, we can statistically test whether SiO produces significant absorption. The approach consists of four main steps.

First, a theoretical high-resolution template for the molecule (CO in their case) was generated to locate specific absorption features. Grant et al. (2023) produced a “CO-only” model spectrum and a comparative model with CO removed, then removed the continuum from each using a Savitzky–Golay smoothing filter to isolate the fine spectral features. Wavelength points in the CO-only model showing strong CO absorption (above a chosen normalized threshold) were marked as in-band, provided the same wavelengths showed negligible absorption in the CO-removed model. This step ensured that the in-band mask captured only CO-specific sub-band features and not spurious overlaps with other species. Conversely, wavelengths where the CO-only model’s absorption lay below a low threshold (essentially continuum regions) and had no other species’ signals were designated as out-of-band. In this way, a set of CO sub-bands (clusters of CO absorption lines at the instrument’s resolution) was defined for in-band, and the intervening continuum-like regions were defined as out-of-band.

The high-resolution template mask was then aligned to the observed JWST spectrum. Grant et al. (2023) convolved the CO model to the NIRSpec G395H line-spread function and rebinned it onto the observed wavelength grid. This interpolation step ensured that the in-band and out-of-band wavelength ranges corresponded exactly to the bins of the observed medium-resolution spectrum. By doing so, each observed spectral data point could be unambiguously classified as either in-band or out-of-band according to the generated template.

Using these masks, they computed the mean measured transit depth for all in-band wavelength bins and compared it to the mean transit depth of all out-of-band bins. In practice, this involved averaging the planet's transit depth across all wavelengths where CO was predicted to absorb, and separately averaging across the nearby continuum points.

Finally, to assess whether the in-band average transit depth was significantly greater than the out-of-band average (as expected if CO is present), Grant et al. (2023) performed a two-sample Welch's t-test. The null hypothesis (H_0) assumed no difference between the in-band and out-of-band depth means, while the one-sided alternative (H_1) posited that the in-band mean is larger. This approach accounts for unequal variances and sample sizes in the two categories. In the WASP-39b CO analysis, the t-test returned $t \approx 3.90$ with $p \approx 6 \times 10^{-5}$, allowing the null hypothesis to be rejected with high confidence. Thus, the data showed a statistically significant deeper transit in the CO in-band wavelengths compared to the out-of-band wavelengths.

Figure 3.2 presents the overall design of this approach. The top panel shows a high-resolution model spectrum (originally for CO) at both its simulated native resolution (gray) and after convolution with the observed point-spread function and rebinning (black). The middle panel provides a schematic of the mask construction, with red indicating wavelengths classified as in-band and blue representing out-of-band regions. The bottom panel displays the contribution of different molecules, highlighting that, in the original study, CO was the dominant absorber while other species contributed less significantly.

Using this in-band/out-of-band method, Grant et al. (2023) found in-band transit depth approximately 264 ± 68 ppm deeper than the out-of-band regions, with this contrast closely matching model predictions. Their statistical framework provided an objective metric for detection significance rather than relying on visual identification of spectral features.

In summary, this method effectively "stacks" the signal from many absorption lines into a single

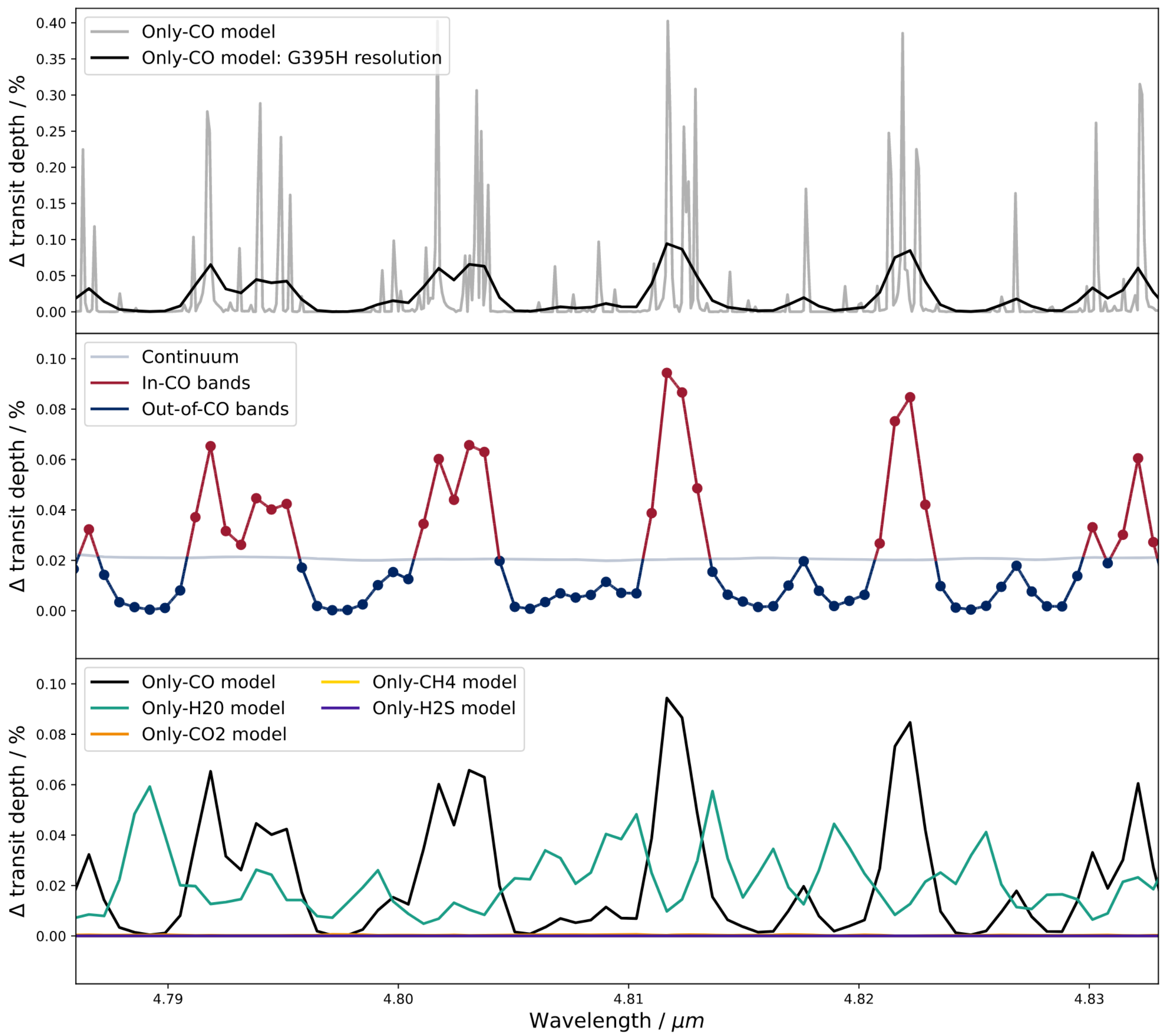

Figure 3.2: Illustration of in-band/out-of-band masking scheme. **Top panel:** the theoretical high-resolution template for CO (gray line) is shown at its native sampling and after convolution with the instrument point-spread function and rebinning (black line). **Middle panel:** the mask construction is presented, where the red regions denote in-band wavelengths and blue regions denote out-of-band wavelengths. **Bottom panel:** the contributions of different molecules to the model, with CO being the primary absorber and other species contributing minimally. The figure is adapted from Grant et al. (2023).

statistical test, creating a sensitive technique for molecular detection that we apply to search for SiO in WASP-178b's atmosphere.

3.2.2 Technique Adaptation to HST/STIS NUV data

Before we adapt the in-band/out-of-band technique to detect SiO in WASP-178b's HST/STIS NUV transmission spectrum, we account for several differences from the original JWST/CO application:

Molecular Complexity and Wavelength Coverage JWST/NIRSpec G395H provided a broad 4.4–5.0 µm coverage, where the CO fundamental band overlaps with other species' features (e.g., H_2O and CO_2). Given such case, Grant et al. (2023) had to carefully exclude wavelengths where H_2O contributed appreciably, to isolate CO's signal. In our NUV spectrum, the situation is cleaner as SiO is expected to be the dominant absorber in this range, with minimal contribution from other molecules or clouds (Lothringer et al., 2020, 2021). This allows us to use a single SiO template without needing a "SiO-removed" control model.

Spectral Resolution and Line Blending HST/STIS offers much higher spectral resolution ($R \sim 30,000$) than JWST/NIRSpec ($R \sim 2700$). At this resolution, many SiO absorption lines appear as distinct features rather than blended bands. We define in-band regions around individual SiO line centers where possible, but merge lines that fall within 0.05 Å of each other (approximately one STIS resolution element) to avoid artificially splitting observed features.

Using the normalized SiO cross-section template from Section 3.1, we classify spectral wavelengths into three categories:

- SiO In-Band: Wavelengths where the SiO cross-section exceeds a chosen threshold, representing regions of significant SiO absorption.

- SiO Out-of-Band: Wavelengths where the SiO cross-section is essentially zero, representing continuum regions. We constrain these to wavelengths ≥ 2500 Å to avoid potential contamination from strong features at shorter wavelengths.

- Between-Band: Intermediate regions with moderate SiO absorption, typically line wings, which we exclude from the primary statistical comparison. We mark such points separately to avoid diluting the out-of-band sample with slight absorption or, conversely, to avoid expanding the in-band mask too far into the continuum.

To test for the presence of SiO, we compare the average transit depths in in-band versus out-of-band regions. Here, Λ represents the set of wavelengths, with $\Lambda_{\text{SiO-in}}$ denoting wavelengths where strong SiO absorption is expected and $\Lambda_{\text{SiO-out}}$ denoting wavelengths with minimal SiO absorption. The mean transit depth within each set is distributed as normal distribution ($\mathscr{N}$):

$$\overline{\delta(\Lambda_{\text{SiO-in}})} \sim \mathscr{N}\left(\mu_{\text{in}}, \frac{\sigma_{\text{in}}^2}{n_{\text{in}}}\right), \tag{16}$$

$$\overline{\delta(\Lambda_{\text{SiO-out}})} \sim \mathscr{N}\left(\mu_{\text{out}}, \frac{\sigma_{\text{out}}^2}{n_{\text{out}}}\right), \tag{17}$$

where μ_{in} and μ_{out} represent the mean transit depths in the respective wavelength regions, and $\sigma_{\text{in}}^2/n_{\text{in}}$ and $\sigma_{\text{out}}^2/n_{\text{out}}$ are the variances of the sample means, with n_{in} and n_{out} representing the number of data points in each region.

We then test statistically if the in-band sample displays greater SiO absorption than the out-of-band sample using a hypothesis test. The detection of SiO is evaluated by testing the null hypothesis $H_0 : \mu_{\text{in}} \leq \mu_{\text{out}}$ against the alternative hypothesis $H_1 : \mu_{\text{in}} > \mu_{\text{out}}$ using Welch's one-tailed t-test, which accounts for potentially unequal variances between the two groups.

To establish the statistical significance of any difference, we perform this test where H_0 assumes the mean in-band depth equals the mean out-of-band depth (no SiO signal), and H_1 assumes the in-band mean is greater (consistent with an SiO absorption signal):

$$H_0 : \mu_{\text{in}} \leq \mu_{\text{out}} \quad | \quad H_1 : \mu_{\text{in}} > \mu_{\text{out}} \tag{18}$$

This two-sample test provides a p-value to assess how unlikely such a difference would be if SiO were absent. A very low p-value (e.g., < 0.001) would indicate a robust detection of SiO, analogous

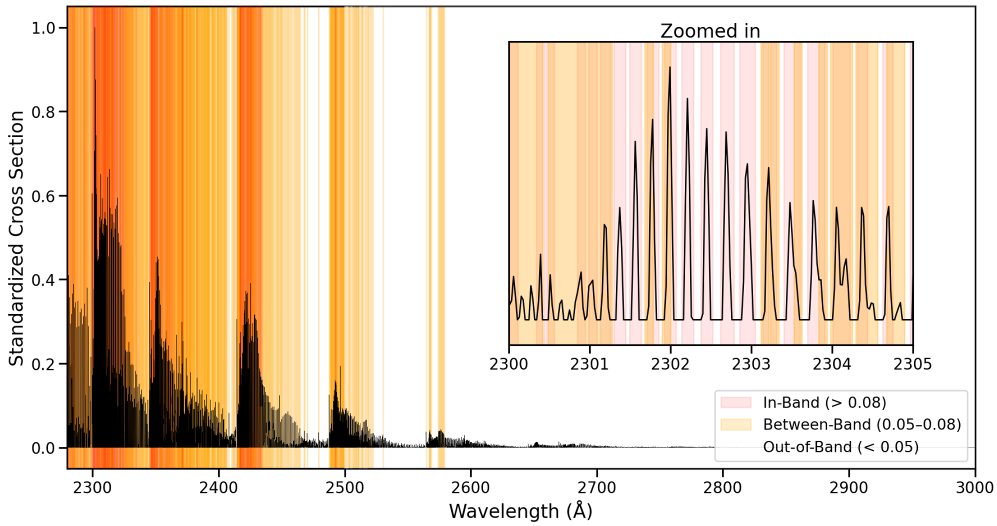

Figure 3.3: Visualization of In-Band, Out-of-Band, and Between-Band Selection

to the CO case.

Figure 3.3 shows the in-band/out-of-band masking approach as applied to the SiO analysis. The normalized SiO cross-section from ExoMol SiO linelist after continuum removal is shown in black. Several sharp SiO absorption lines are evident as spikes in this theoretical spectrum. Based on our threshold criteria (detailed in Section 4.2), we classify wavelengths where the normalized SiO cross-section exceeds 0.08 as in-band regions (highlighted as red shaded bands), representing the strongest SiO absorption features. The flat baseline between the spikes represents the continuum level where the cross-section is near zero; those intervals correspond to the out-of-band regions (in white). Areas with intermediate cross-section values between 0.05 and 0.08 (the flanks of the spikes) are classified as between-band zones (in orange) and excluded from our statistical comparison to avoid diluting the signal contrast between clear absorption and continuum regions.

4 Analysis and Results

4.1 Transmission Spectrum of WASP-178b

We apply the systematic correction model derived from jitter correlation parameters across various spectral bin sizes to generate WASP-178b's transmission spectrum. This approach ensures that wavelength-dependent variations in the observed light curves can be attributed primarily to atmospheric absorption rather than instrumental systematics. We compute the transmission spectrum at three different binning scales — broadband (200 Å), narrowband (4 Å), and native resolution (0.1 Å), which allows us to balance signal-to-noise considerations against fine spectral detail.

4.1.1 Broadband and Narrowband Analysis

We start by analyzing the data at broad wavelength bins. The broadband analysis (200 Å bins) revealed a generally flat profile across the NUV wavelength range, with a notable increase in $R_p(\lambda)/R_\star$ at wavelengths shorter than 2500 Å, consistent with excess NUV absorption. This finding aligns with theoretical predictions and previous studies of ultra-hot Jupiters.

When re-binned to 4 Å resolution, the transmission spectrum exhibited increased scatter as expected, due to reduced photon counts per bin, but maintained the pattern of systematically higher transit depths at shorter wavelengths (<2500 Å). This trend supports the prediction of wavelength-dependent molecular absorption. Like Lothringer et al. (2021), our analysis confirms that WASP-178b shows no significant Fe II or Mg II absorption features, in contrast to WASP-121b (Figure 4.1). This spectral difference between these two ultra-hot Jupiters provides important context for interpreting our SiO detection. Detailed light curve fits and additional diagnostic plots for both binning scales are presented in Appendix D.

4.1.2 Native Resolution Analysis (0.1 Å bin)

To maximize sensitivity for detecting SiO absorption bandheads, we generated a transmission spectrum at native resolution with 0.1 Å bins (~ 2 pixels per bin in the STIS E230M mode). This

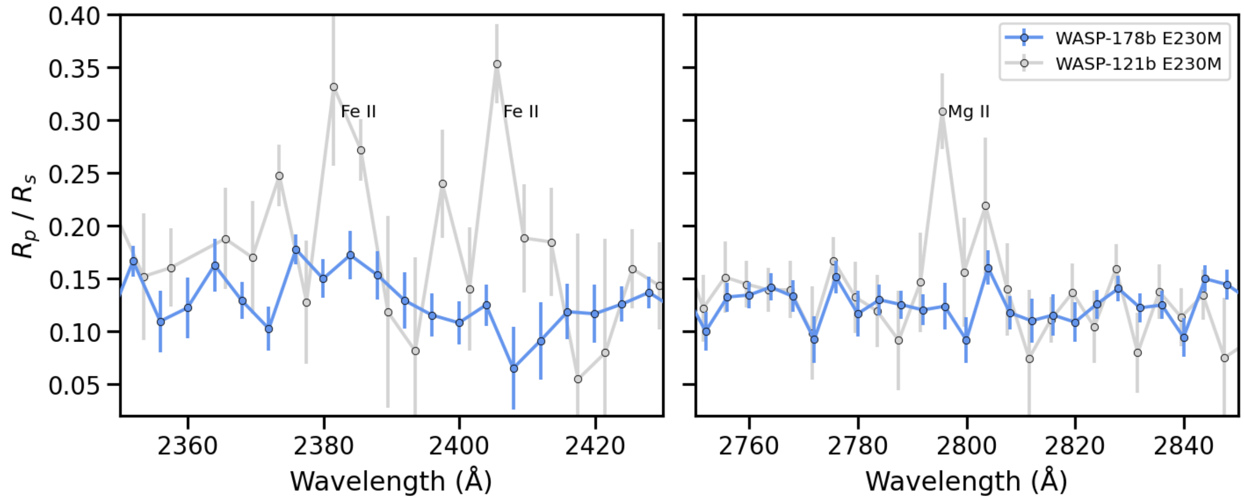

Figure 4.1: Comparison of HST/STIS/E230M spectra for WASP-178b (blue) and WASP-121b (grey, data from Sing et al. (2019)). While WASP-121b shows prominent Fe II and Mg II absorption features, WASP-178b's spectrum is consistent with a broadband NUV continuum lacking these specific metal signatures. This confirms the findings of Lothringer et al. (2021) and highlights the distinct atmospheric chemistry of these two ultra-hot Jupiters.

fine sampling resolves narrow molecular features, though at the expense of higher photon noise due to the inherently low stellar flux in the NUV region.

The raw spectroscopic data contained 7942 wavelength bins spanning 2277.94 to 3072.15 Å. We implemented a robust outlier filtering approach based on statistical analysis of the spectrum. First, we calculated the percentile distributions of transit depth, error, and signal-to-noise ratio to establish appropriate filtering thresholds. We set transit depth limits to 0.01-15.12% (corresponding to physically plausible values while allowing for the higher scatter expected in NUV spectra), error limits with a maximum threshold of 13.04% (based on the 99th percentile of the error distribution), and a minimum SNR threshold of 0.05 (derived from the 5th percentile of the SNR distribution scaled by a conservative factor).

This filtering process removed 2405 data points ($\sim$ 30% of the original dataset), resulting in 5537 measurements in the final transmission spectrum. An additional sigma-clipping stage with a threshold of 7.0σ was applied as a final quality control measure, though it removed no additional points, indicating our initial filtering criteria had successfully eliminated the most severe outliers.

Figure 4.2 shows our cleaned high-resolution transmission spectrum with a smoothing window

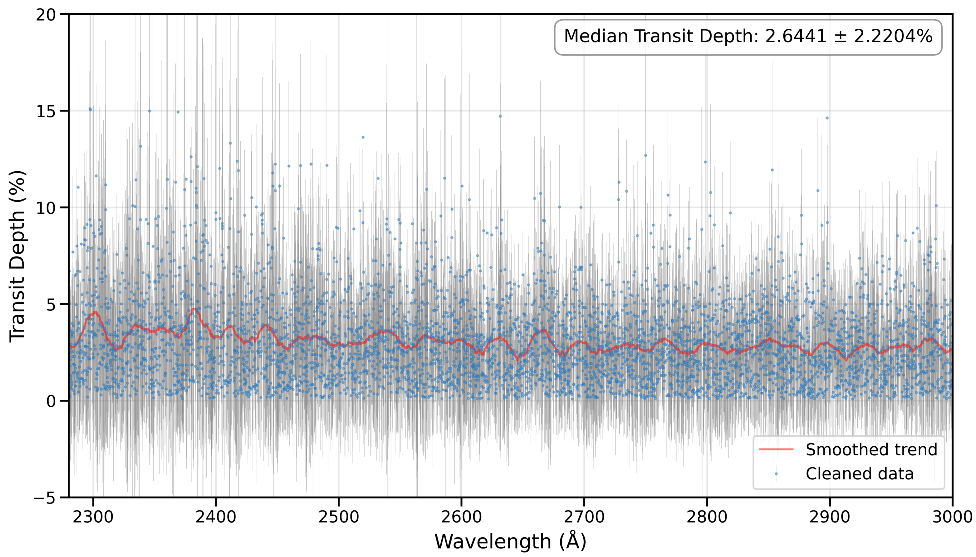

Figure 4.2: Native resolution (0.1 Å) transmission spectrum of WASP-178b in the near-ultraviolet region after quality filtering. Blue points represent individual measurements with their associated uncertainties (gray vertical lines). The red curve shows the smoothed trend calculated using a Savitzky-Golay filter(window size=200 points). The spectrum reveals increased absorption at wavelengths below 2500 Å, with notable peaks near 2280 Å and 2380 Å.

of 200 points. The filtered data has a median transit depth of $2.64 \pm 2.22\%$. This median depth is notably larger than the white light curve depth of $1.63 \pm 0.06\%$. The systematic offset is primarily attributed to wavelength-dependent stellar limb darkening, which is more pronounced in the NUV region, along with differential extinction effects in the echelle format. This offset does not impact our analysis, as our methodology focuses on the differential signal between in-band and out-of-band regions rather than absolute transit depths.

The smoothed trend line in Figure 4.2 reveals wavelength-dependent variations in the transit depth. We observe increased absorption at wavelengths below 2500 Å with prominent peaks around 2280 Å and 2380 Å where smoothed transit depths exceed 4%. Figure 4.3 shows the filtering process, with clear contrasts between the original data points (red) that were removed by our quality criteria, and the retained points (blue) that form our final transmission spectrum. This forms the foundation for our subsequent statistical analysis using the in-band/out-of-band technique to detect SiO absorption.

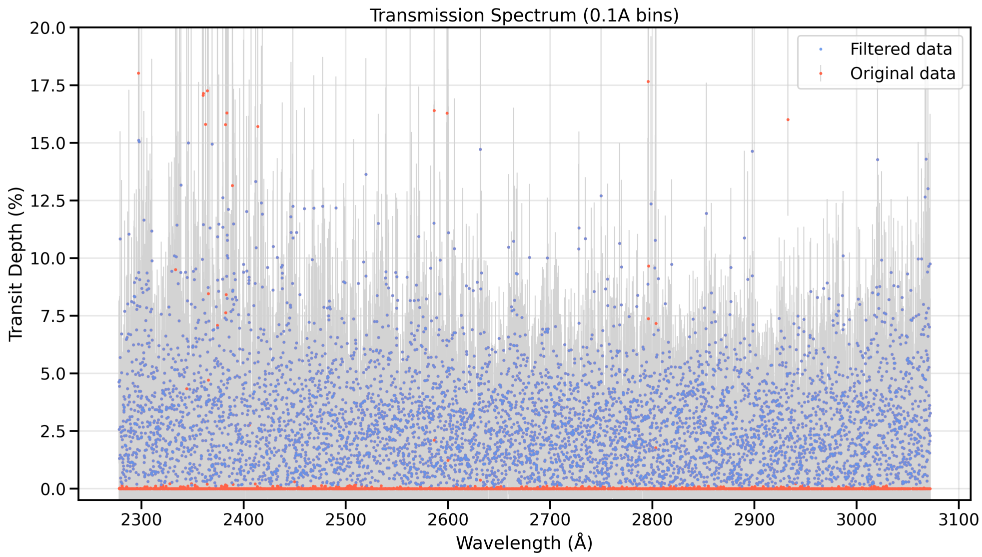

Figure 4.3: Comparison of original and filtered data points in the NUV transmission spectrum of WASP-178b at 0.1 Å resolution. Red points indicate data removed by our quality filtering criteria (transit depths outside 0.05-15.12%, errors exceeding 13.04%, or SNR below 0.05), while blue points represent measurements retained in the final analysis. The filtering process removed 2405 of 7942 original data points (30%), primarily eliminating physically implausible values with extremely low or high transit depths, while preserving the structure of spectral features.

4.2 Detection and Characterization of SiO Feature

Using our definition of SiO sub-bands outlined in Section 3.2, we categorize transit depths from the native-resolution transmission spectrum into two groups: in-band (wavelengths with expected strong SiO absorption) and out-of-band (wavelengths with minimal expected SiO absorption). This classification generates two distinct samples corresponding to different predicted absorption strengths. After removing the continuum from the observed transit depths to isolate high-resolution SiO features, we perform statistical analysis to determine whether the in-band regions show significantly deeper transit depths than out-of-band regions.

The SiO in-band sample, $\delta(\Lambda_{\text{SiO-in}})$, yields a mean transit depth of $\mu_{\text{in}} = 3.493\%$ with a standard deviation of $\sigma_{\text{in}} = 2.809\%$ across $n_{\text{in}} = 380$ wavelength bins. In contrast, the SiO out-of-band sample, $\delta(\Lambda_{\text{SiO-out}})$, produces a mean transit depth of $\mu_{\text{out}} = 2.845\%$ with a standard deviation of $\sigma_{\text{out}} = 1.977\%$ across $n_{\text{out}} = 3533$ wavelength bins. The respective standard errors of these means are $\sigma_{\text{in}}/\sqrt{n_{\text{in}}} = 0.144\%$ and $\sigma_{\text{out}}/\sqrt{n_{\text{out}}} = 0.033\%$.

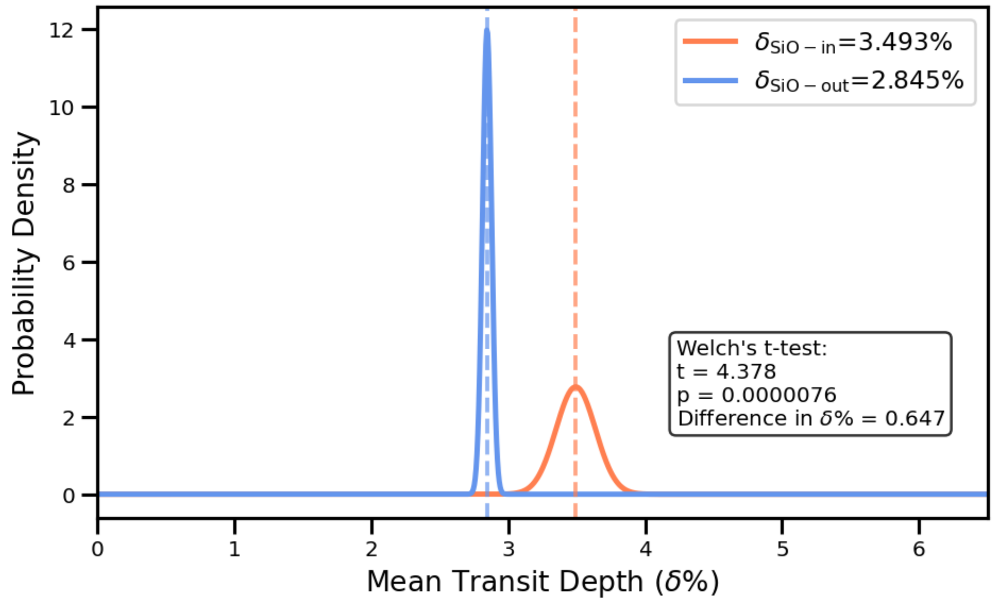

Figure 4.4: Gaussian-modeled sampling distributions of the mean transit depths for the in-band (coral) and out-of-band (blue) SiO regions. The distributions are centered on the measured means (3.493% and 2.845%, respectively), with standard deviations reflecting the observed sample uncertainty. The clear separation between these two distributions shows the statistical significance of our SiO detection.

To assess whether the in-band regions show greater SiO absorption than out-of-band regions quantitatively, we implement a one-tailed Welch's t-test (Welch, 1947) which accounts for the unequal variances and sample sizes between two groups. The test yields a t-statistic of $t = 4.378$ and a p-value of $p = 7.6 \times 10^{-6}$. This p-value indicates that if SiO were absent from WASP-178b's atmosphere (our null hypothesis), the probability of observing our measured difference between in-band and out-of-band transit depths by random chance would be approximately 0.00076%—equivalent to a detection significance exceeding 4.3σ. Given that conventional scientific standards consider results significant at 3σ ($p < 0.003$) and highly significant at 5σ ($p < 0.0000006$), our detection shows strong statistical confidence. The significant difference in sample sizes between in-band (380) and out-of-band (3533) regions leads to a much larger standard error for the in-band mean (0.144% vs. 0.033%), making our detection even more significant since we were able to identify a statistically meaningful difference despite the in-band measurements having approximately 4.4 times higher uncertainty due to the smaller sample size.

Figure 4.4 visualizes this statistical analysis, showing the sampling distributions of mean transit depths for both wavelength sets. The difference between these means ($0.647 \pm 0.148\%$) represents clear excess absorption in regions where SiO features are predicted by theoretical models. Figure 4.5 shows the light curve models of the measured difference in transit depth for in- and out-of-band data.

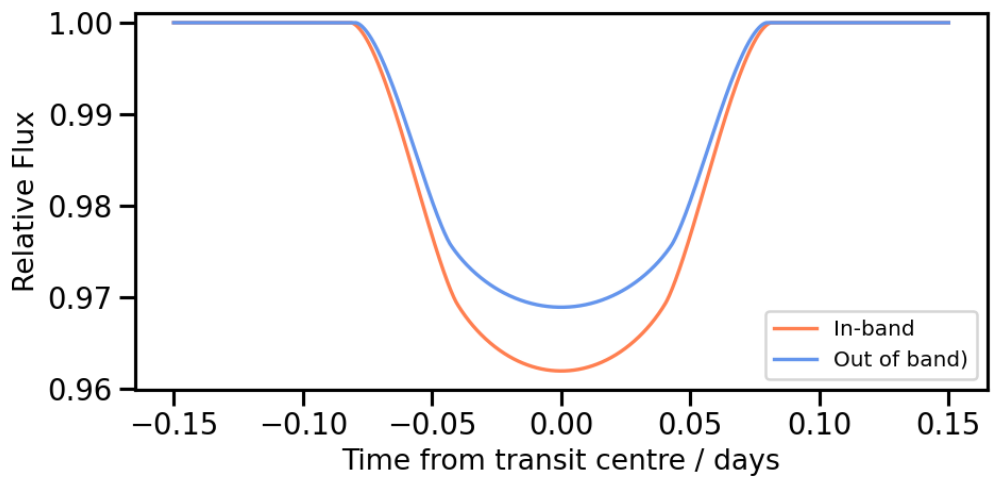

Figure 4.5: Model transit light curves for in-band (coral) and out-of-band (blue) wavelength regions. The in-band curve shows a much deeper transit compared to the out-of-band curve, consistent with stronger SiO absorption in the in-band regions.

4.2.1 Sensitivity Test for Thresholds

To assess the robustness of our detection, we conducted sensitivity tests on the two parameters defining our wavelength masks: the in-band threshold and between-band minimum threshold (Section 3.2.2). We selected an in-band threshold of 0.08 and a between-band minimum threshold of 0.05 for our primary analysis. These values were chosen to: (1) capture only the strongest and most reliable SiO absorption features while excluding weaker signals potentially contaminated by noise, (2) maintain adequate sample sizes in both in-band and out-of-band categories for robust statistical analysis, and (3) preserve the characteristic bandhead structures that provide the clearest spectroscopic signature of SiO.

As shown in Figure 4.6, we systematically varied both thresholds and analyzed the resulting statistical significance and effect size. The left panel of Figure 4.6 shows how the mean difference between in-band and out-of-band transit depths varies with threshold choices. Lower in-band thresholds generally yield larger mean differences (deeper red), indicating stronger signals. This pattern reflects that more restrictive thresholds select only the strongest SiO features, increasing contrast between in-band and out-of-band regions.

The right panel shows the inverse relationship between mean difference and p-value. Each point represents a threshold combination, with color indicating the in-band threshold value. The downward trend confirms that larger transit depth differences correspond to more significant detections (lower p-values). Notably, nearly all threshold combinations below an in-band value of 0.15 yield statistically significant results ($p < 0.05$, below the red dashed line), with many achieving high significance levels ($p < 0.001$, equivalent to $> 3.3\sigma$ confidence).

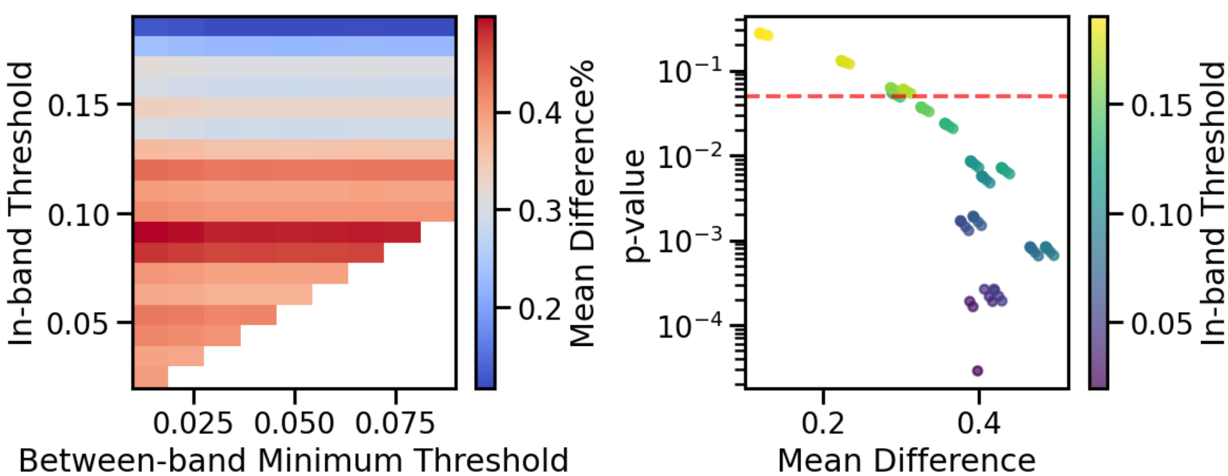

Figure 4.6: Sensitivity analysis for SiO detection across threshold combinations. **Left panel:** Mean difference between in-band and out-of-band transit depths for various combinations of in-band threshold (y-axis) and between-band minimum threshold (x-axis). Redder colors indicate larger differences (stronger signal). The trend reveals that lower in-band thresholds initially yield stronger signals as more SiO features are captured, but eventually decrease in effectiveness as weaker absorption features become included. **Right panel:** Mean transit depth difference vs. p-value (logarithmic scale). The horizontal red dashed line indicates the $p = 0.05$ significance level (2σ confidence), with points below this line representing statistically significant detections. As the mean difference increases, the statistical significance generally improves (lower p-values), confirming the robustness of our detection across multiple threshold combinations. Our adopted thresholds (in-band = 0.08, between-band minimum = 0.05) represent an optimal balance between signal strength and statistical significance.

Our chosen parameters achieve high statistical significance ($p = 7.6 \times 10^{-6}$, $> 4.3\sigma$ confidence) while remaining conservative in feature selection. Lower in-band thresholds would include progressively weaker absorption features that, while potentially real, diverge from the clear bandhead structures characteristic of SiO and could introduce systematic uncertainties.

In addition to the threshold sensitivity analysis, we conducted a bootstrap resampling analysis to further assess the robustness of our SiO detection against statistical variations in the data. Figure 4.7 presents the results of this bootstrap sensitivity test using our selected thresholds.

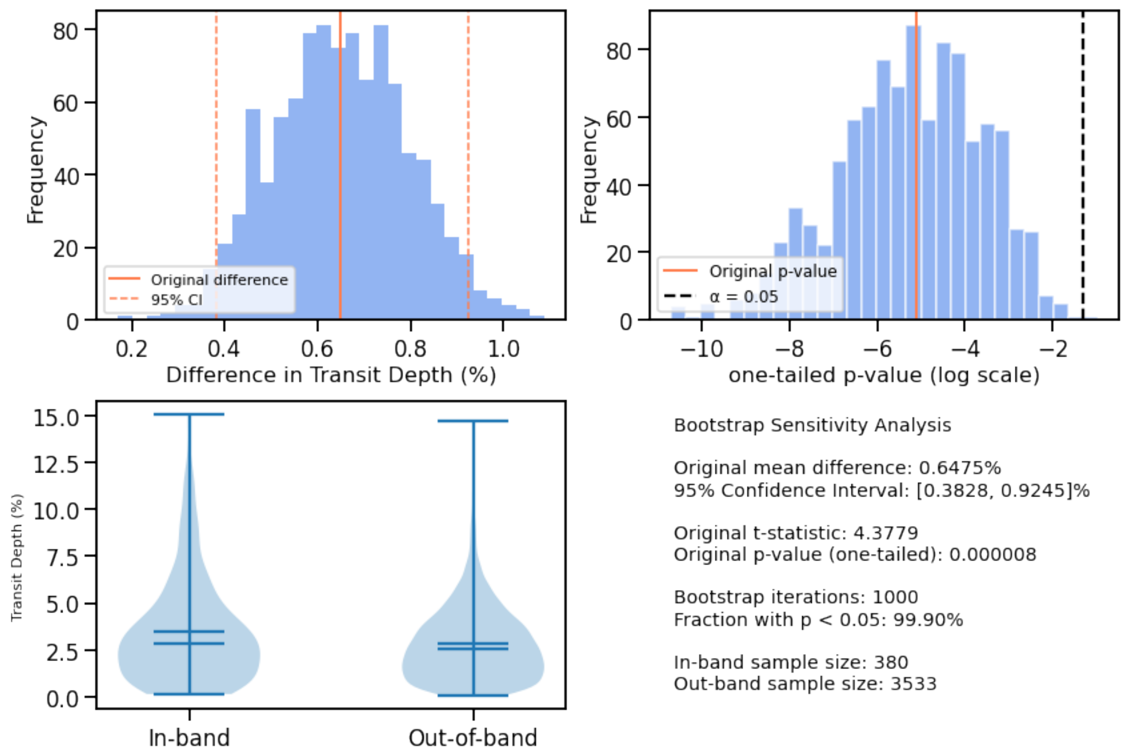

Figure 4.7: Bootstrap analysis of SiO detection robustness. **Top left:** Distribution of transit depth differences between in-band and out-of-band regions across 1000 bootstrap iterations, with original difference (solid line) and 95% confidence interval (dashed lines). **Top right:** Distribution of one-tailed p-values on logarithmic scale, with original p-value (solid line) and significance threshold (0.05, dashed line). **Bottom left:** Violin plots comparing transit depth distributions for in-band and out-of-band regions. **Bottom right:** Summary statistics showing a highly significant detection ($p = 8 \times 10^{-6}$) with 99.9% of bootstrap iterations yielding significant results.

The bootstrap analysis randomly resampled our data with replacement for 1000 iterations, which provides a distribution of possible outcomes given the inherent variability in our measurements. As shown in the top left panel of Figure 4.7, the distribution of transit depth differences is wellseparated from zero, with a mean difference of 0.6475% and a 95% confidence interval of [0.3671%, 0.9457%]. The top right panel displays the distribution of p-values on a logarithmic scale, revealing that all bootstrap iterations produced highly significant results. We can see 99.90% of iterations yielded p-values below 0.05, with the majority producing extremely significant results ($p < 10^{-4}$). The bottom left panel presents the difference in transit depth distributions between in-band and out-of-band regions through violin plots. Despite the considerable sample size difference (380 in-band versus 3533 out-of-band measurements), the separation between distributions is clear and consistent with our reported detection.

Taken together, the threshold sensitivity test and bootstrap analysis provide complementary evidence for the robustness of our SiO detection. While the threshold analysis shows that our results are not dependent on specific parameter combination choices, the bootstrap analysis confirms that the detection remains significant against random variations in the dataset.

5 Discussion

5.1 Implications of SiO Detection

SiO has long been theorized to be an important opacity source in ultra-hot Jupiters (UHJs) (Lothringer et al., 2018; Parmentier, Vivien et al., 2018), and our detection of SiO in the atmosphere of WASP-178b provides empirical confirmation of its presence. The statistically significant absorption we detect in the near-ultraviolet (NUV) region offers critical insights into the thermal structure of UHJ atmospheres.

First, SiO can serve as an efficient absorber of stellar irradiation in the upper atmospheric layers. The strong NUV absorption bands of SiO indicate that this molecule efficiently captures high-energy photons from the host star. This energy absorption in the upper atmosphere can produce localized heating effects, potentially contributing to the formation of a thermal inversion layer. Our detection thus provides direct observational evidence supporting the theoretical prediction that SiO, alongside other species such as TiO, VO, and Fe, plays an important role in establishing thermal inversions in UHJs (Fortney et al., 2008; Gandhi & Madhusudhan, 2019).

Second, the presence of SiO indicates that silicon-bearing species remain in the gas phase in the upper atmosphere of WASP-178b. With an equilibrium temperature of 2470 K, WASP-178b represents a regime where silicon chemistry transitions between condensed and gaseous phases. The detection of gaseous SiO suggests that the atmospheric temperature in the observed region exceeds the condensation threshold for silicon-bearing species, consistent with the expected vertical temperature profile exhibiting an inversion. This observation aligns with recent theoretical models by Hoeijmakers et al. (2019) and Fossati et al. (2021), which predict that silicon species remain primarily in the gas phase at the extreme temperatures characteristic of UHJs.

The abundance of SiO relative to other atmospheric constituents, while not precisely constrained by our current analysis, can provide valuable constraints for atmospheric models of UHJs. The strong absorption signal detected in our analysis suggests that SiO exists in sufficient quantities to produce observable effects in transmission spectroscopy. Given that silicon is expected to be among the more abundant heavy elements in these planets due to its cosmic abundance, our detection is consistent with a scenario where a significant fraction of atmospheric silicon exists in the form of SiO. Future quantitative abundance determinations will help refine our understanding of silicon chemistry in these extreme environments.

Finally, our detection of SiO expands the current understanding of ultra-hot Jupiter atmospheres. These planets clearly possess complex atmospheric compositions where multiple molecular and atomic species contribute to the overall opacity structure. SiO is particularly important in shaping the temperature-pressure profile through its strong NUV absorption properties. This finding has direct implications for atmospheric modeling: comprehensive models of UHJ atmospheres must now account for SiO opacity to accurately predict thermal structures. This is especially significant in the near-ultraviolet wavelength range—a spectral region where relatively few exoplanet observations have previously been conducted.

5.2 Limitations and Potential Sources of Error

While our detection of SiO in WASP-178b's atmosphere is statistically robust, several important limitations should be considered when interpreting our results and planning future investigations.

The most significant limitation stems from the substantial systematic effects in the HST/STIS E230M dataset. The instrument's lower sensitivity at NUV wavelengths results in reduced signal-to-noise ratios compared to optical and infrared observations, particularly below $\sim 2500\,\text{Å}$ where instrument efficiency decreases substantially. The observations we use in this work exhibit more than 25% variations in the normalized raw flux across the visit, creating a challenging baseline for precise transmission spectroscopy. These strong systematics, while partially corrected through jitter decorrelation technique, remain a dominant source of uncertainty in the final transmission spectrum.

At native resolution (binsize = 0.1Å), each spectral bin contains only ~ 2 detector pixels, which severely limit the achievable signal-to-noise ratio. This inherently low SNR, combined with the instrument's reduced sensitivity at NUV wavelengths, explains why our native-resolution transit depths ($2.64 \pm 2.22\%$) appear systematically higher than the white light curve measurement

(1.63 ± 0.06%). The discrepancy arises primarily from the propagation of systematic errors when analyzing extremely small wavelength bins with limited photon statistics. Despite these instrumental challenges, our comparative in-band/out-of-band methodology remains robust because it relies on the relative difference between wavelength regions rather than absolute transit depths. Through analysis of the differential signal between predicted SiO absorption features and adjacent continuum regions, we effectively mitigate many of the systematic effects that would otherwise compromise a traditional spectral analysis.

While our analysis confidently detects the presence of SiO, we cannot currently provide quantitative constraints on its abundance in WASP-178b's atmosphere. Translating our detection into a volumetric mixing ratio would require not only additional modeling but also higher spectral resolution and signal-to-noise data capable of resolving individual SiO lines or bandheads. The current medium-resolution space-telescope data, while sufficient to detect the presence of SiO through statistical methods, lacks the spectral resolution and precision necessary to break the degeneracies between abundance, temperature, and pressure in the radiative transfer problem.

In summary, the discussed limitations address the need for follow-up observations with higher sensitivity and spectral resolution. Future studies combining HST NUV observations with high-resolution ground-based spectroscopy and JWST observations at longer wavelengths would provide complementary constraints that could overcome many of these limitations, potentially lead to robust abundance measurements and more detailed characterization of SiO's role in ultra-hot Jupiter atmospheres.

5.3 Application of Methods to Other Ultra-hot Jupiters

Our in-band/out-of-band technique can be directly applied to existing HST/STIS/E230M observations of other ultra-hot Jupiters (UHJs) to search for SiO signatures. Several UHJs have already been observed in the NUV with the same instrumental configuration used for WASP-178b, making comparative analysis possible. For each target, the theoretical SiO cross-section can be recalculated at their equilibrium temperature using the ExoMol line list to reflect the expected molecular features under the specific planetary conditions.

Among the candidates, KELT-9b ($T_{eq} \sim 4050$K, GO-16270) represents the most extreme temperature regime and could reveal whether SiO remains stable or dissociates at such intense heating. WASP-189b ($T_{eq} \sim 2600$K) and WASP-121b ($T_{eq} \sim 2500$K) both have E230M spectra from PanCET and HST-SHEL legacy programs, with the latter being particularly interesting for comparison since retrievals have previously suggested SiO in its atmosphere. WASP-76b ($T_{eq} \sim 2200$K) offers data at a slightly lower temperature that approaches the expected silicate condensation threshold. Additionally, WASP-79b ($T_{eq} \sim 1800$K) has E230M observations showing a rising NUV radius potentially attributable to SiO opacity.

A systematic analysis across these temperature regimes (1800-4050 K) would establish the thermal threshold for SiO formation and persistence in exoplanet atmospheres. By applying consistent methodology across the sample, we could determine whether SiO shows a binary presence/absence pattern or exhibits a gradual transition in abundance as temperature decreases. This comparative approach would also help distinguish genuine SiO features from potential contamination by other NUV absorbers such as metal ions or photochemical products.

The technique can be extended to search for other molecular species with distinct band structures in UHJ atmospheres. For example, metal oxides like TiO and VO, when appropriate theoretical cross-sections are available, could be analyzed using the same in-band/out-of-band statistical framework. This could provide insights to the ongoing debate about whether these species contribute to thermal inversions in UHJs.

Multi-wavelength analysis combining our NUV technique with complementary observations would provide comprehensive atmospheric characterization. Many of the UHJs with E230M data also have HST WFC3 infrared spectra, allowing simultaneous constraints on both refractory and volatile species. For WASP-121b, WASP-178b, and others with JWST observations, the expanded wavelength coverage would enable complete inventory of atmospheric constituents from NUV to mid-infrared. This approach would conclusively establish the role of gaseous SiO in the atmospheric chemistry, thermal structure, and condensation processes of the hottest known exoplanets.

6 Conclusion and Future Work

We detect silicon monoxide (SiO) in the near-ultraviolet (2275–3000 Å) transmission spectrum of WASP-178b with HST/STIS E230M at $> 4.3\sigma$ significance ($t = 4.38$, $p = 7.6 \times 10^{-6}$), marking one of the first unambiguous SiO identifications in an exoplanet atmosphere. An in-band/out-of-band differential analysis based on the 2021 ExoMol SiO line list shows a difference of $0.647 \pm 0.148\%$ between mean transit depth of regions containing SiO features (in-band) compared to regions without SiO features (out-of-band). Sensitivity tests confirm the robustness of this detection to reasonable changes in window definitions and filtering thresholds.

Gas-phase SiO at the planet's equilibrium temperature of ~ 2470 K indicates that silicon remains uncondensed at these altitudes of about a microbar, supporting models in which silicate clouds form at cooler temperatures. SiO's strong NUV opacity likely contributes to upper-atmosphere heating and may drive a thermal inversion. Together with earlier detections of neutral and ionized metals, the SiO detection shows that refractory species largely stay in the gas phase in WASP-178b, providing empirical constraints for models of cloud formation, radiative balance, and vertical mixing in ultra-hot Jupiter atmospheres.

Looking ahead, future work should develop retrieval frameworks optimized for NUV molecular features. Traditional codes have focused on optical/infrared spectra; incorporating up-to-date high-temperature line lists and a comprehensive set of NUV opacity sources will allow multi-band retrievals that simultaneously fit data from NUV through infrared. Adapting existing tools (e.g., PETRA, NEMESIS, petitRADTRANS) to include SiO is needed for interpreting forthcoming observations of hot and ultra-hot Jupiters. A systematic survey of SiO across multiple UHJs would contextualize our detection and clarify temperature-dependent chemistry. Comparisons between WASP-178b and slightly cooler planets such as WASP-121b suggest a threshold where silicate species condense; targeting planets across a wide temperature range will help map the incidence of SiO, TiO, and metal ions and refine cloud-formation models.

JWST offers new opportunities to confirm and characterize SiO. Combining NUV and infrared measurements in unified retrievals will break degeneracies and yield robust abundances; recent studies show that retrievals using only UV or only IR data can diverge, suggesting the need for joint analyses. While SiO's strongest bands lie in the NUV, vibrational transitions fall within JWST/NIRSpec and MIRI coverage, enabling a multi-wavelength approach that constrains both SiO and the broader inventory of rock-forming elements.

Finally, incorporating silicon chemistry into three-dimensional global circulation models to interpret these findings would be fruitful. Current chemical networks often lack comprehensive treatment of Mg-, Ti-, Si-, and Fe-bearing species. Expanding these networks to track silicon-bearing molecules (e.g., SiO, SiH_4) and condensates (e.g., $MgSiO_3$, Mg_2SiO_4) will help quantify the silicon budget in UHJs and capture the full 3D context of cloud precursors like SiO, from day-to-night transport to their role in cloud formation.

A Planet Formation Context

A.1 Comparison of Gas Giant and Terrestrial Planet Formation

Gas giant and terrestrial planets both begin as solid cores growing through planetesimal or pebble accretion, but form under vastly different disk conditions. Terrestrial planets form in the hot inner disk where only refractory materials (rock and metal) remain solid. This limited solid inventory constrains core growth to a few Earth masses, preventing significant gas accretion before the nebular gas dissipates.

Giant planets form beyond the water snow line—the distance where water ice condenses (typically a few AU for Sun-like stars). Here, abundant ices increase the available solid mass by a factor of 2–4, enabling rapid core growth to ∼5–15 Earth masses. These massive cores can then gravitationally capture substantial H/He envelopes before gas dispersal, creating gas giants with thick atmospheres.

This snow line paradigm explains the architecture of our Solar System: Jupiter and Saturn formed beyond the ice line and incorporated ice-rich material, while Earth formed inside it and remains ice-poor. Observational evidence supports this core accretion model. Giant planet occurrence correlates strongly with host star metallicity (indicating solid-rich disks), while smaller rocky planets show weaker metallicity dependence. This suggests that high metallicity environments are crucial for massive core formation and gas giant development.

Alternative mechanisms like gravitational instability can fragment gas disks directly, but likely operate only in the outermost regions (tens of AU) under extreme conditions. Such processes cannot explain close-in planets. Overall, core accretion within compositionally stratified disks naturally accounts for the fundamental differences between gas giant and terrestrial planet formation.

A.2 Formation Pathways of Hot Jupiters

Hot Jupiters present a interesting puzzle for planet formation theory. It is widely thought that these planets did not form at their current orbits ($\sim$ 0.03–0.1 AU from their stars) because the inner disk likely lacked enough solid material and had hostile temperature conditions for giant planet formation. Two broad classes of explanations have emerged: in-situ formation versus migration (shown in Figure A.1.

In the in-situ scenario, a hot Jupiter's core forms near the present orbit (likely via local concentration of solids or inward drift of pebbles) and then accretes gas in place. Studies have shown this is possible under extreme disk conditions (very high solid surface density), but it is challenging: the feeding zone close to the star is small, so obtaining a core massive enough for gas accretion is difficult. Dynamical barriers such as orbital migration of smaller cores and competition for

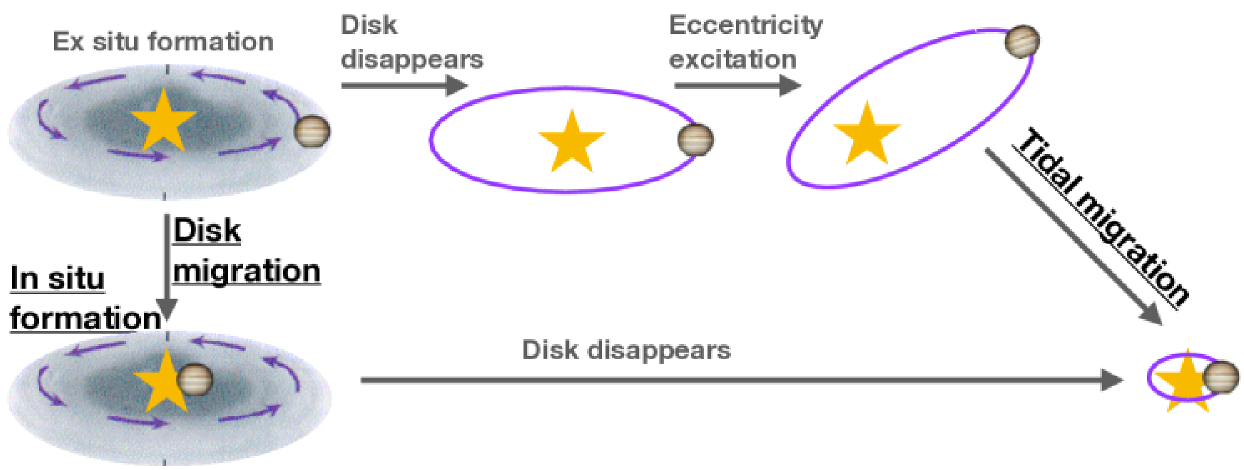

Figure A.1: Schematic depiction of hot Jupiter formation scenarios. Top: ex-situ formation followed by high-eccentricity tidal migration (after the disk disperses, a Jupiter formed at large radius is thrown onto a highly eccentric orbit which shrinks and circularizes close to the star). Middle: disk migration (the planet forms at several AU and spirals inward through the gas disk). Bottom: in-situ formation (the planet's core accretes and accumulates a gas envelope at its present close-in location). Figure adapted from Fortney et al. (2021).

material further hinder in-situ assembly. Thus, pure in-situ formation is not generally favored as the predominant channel.

The alternative is that hot Jupiters formed farther out in the disk (beyond a few AU, where conditions for giant planet formation are favorable) and then migrated inward. Disk migration occurs when a young giant planet exchanges angular momentum with the gaseous disk, causing its orbit to shrink on timescales of 10^5–10^6 years. Hydrodynamic simulations show that a Jupiter-mass planet can migrate from $\sim$5 AU to $\sim$0.05 AU within the disk's lifetime. Classical theories (Type-II migration) predict inward movement until the planet either falls into the star or the disk inner edge; however, mechanisms like a magnetospheric cavity at the inner disk or tidal interactions with the star can halt the planet's inspiral at a short-period orbit. Disk migration is efficient and is consistent with the observed population of hot Jupiters on nearly circular orbits, as migration through a gas disk damps eccentricity.

A third mechanism is high-eccentricity tidal migration. In this scenario, a giant planet forms at a wide orbit and, after the gas disk dissipates, gravitational interactions (such as planet-planet scattering or Kozai–Lidov cycles induced by a distant companion) excite a very high eccentricity. The planet's periastron drops very close to the star; tidal forces then act to circularize the orbit at a small semi-major axis. This mechanism can produce hot Jupiters on very close orbits, possibly at random orientations relative to the stellar spin axis (since the high-eccentricity pathways can scramble orbital inclination). Unlike gentle disk migration, it often leaves tell-tale signatures such as misaligned or retrograde orbits and a population of precursor highly eccentric giants. Some hot

Jupiters indeed have misaligned orbits or moderate eccentricities, suggesting such a dynamical history in certain cases.

Currently, there is no single formation pathway that explains all hot Jupiters, and multiple channels likely operate. Population studies indicate that disk migration and high-eccentricity tidal migration together can account for most hot Jupiter properties. The consensus is that many hot Jupiters formed at a few AU and migrated inward through the disk, while a fraction arrived later via tidal circularization of a highly eccentric orbit. In-situ formation may occur in rare cases (perhaps in very metal-rich disks that allow rapid core growth, but it is not thought to be the dominant route. Open debates revolve around the relative frequency of disk migration vs. high-eccentricity migration, and how to observationally distinguish them. For example, the occurrence of hot Jupiters around high-metallicity stars could hint at efficient core formation (potentially supporting in-situ or efficient formation prior to migration), whereas the spin–orbit misalignments observed for some hot Jupiters (especially around hotter stars) hint that dynamical migration played a role in those systems.

A.3 The Snow Line and Planetary Composition (C/O Ratios)

The snow line - the disk radius beyond which a volatile (e.g., H_2O) condenses into ice, links planetary formation and atmospheric composition. The position of the water snow line (typically a few AU in Sun-like star disks) has a significant effect on a planet's composition. Beyond the water snow line, solids are enriched in oxygen-bearing ices (e.g., H_2O, CO_2, etc.), while the gas is correspondingly depleted in those oxygen species (since they've condensed out). This creates a radial gradient in the elemental ratios: gas inside the H_2O snow line has a near-stellar C/O ratio ($\tilde{0}.5$ for solar composition) with abundant water vapor, whereas gas just outside the snow line can become carbon-rich (since much oxygen is locked in solid ice). Farther out, beyond the CO_2 and CO snow lines (at tens of AU), carbon-bearing gases also condense, altering the C/O ratio again.

Figure A.2 shows how disk chemistry sets the stage for planet composition. In the region between the H_2O and CO_2 snow lines (roughly a few to $\sim$10 AU in this model), the gas-phase C/O ratio rises significantly above the stellar value, approaching $\sim$1.0 (nearly equal carbon and oxygen). This is because water (and some CO_2) has condensed into ice grains, leaving the gas relatively enriched in carbon-bearing species like CO and CH_4. Any gas giant accreting the bulk of its atmosphere from this region would thus acquire a high C/O ratio in its atmosphere. Conversely, the planetesimals and ices accreted by that planet's core are oxygen-rich (low C/O) because they incorporate H_2O, CO_2, etc. Whether the final atmosphere ends up carbon-rich or oxygen-rich depends on the balance of gas vs. solid accretion during formation. If a giant planet's atmosphere is sourced mostly from disk gas outside the water snow line, the intrinsic atmospheric C/O could be

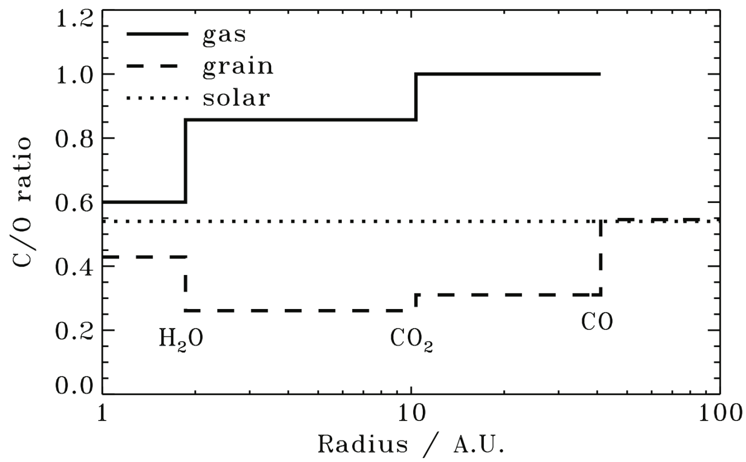

Figure A.2: Radial variation of the carbon-to-oxygen ratio (C/O) in a protoplanetary disk (solid line for gas, dashed line for grains) for a typical T Tauri star disk. H_2O, CO_2, and CO snow line positions are indicated. The dotted line marks the stellar C/O ratio (approximately solar at 0.54). Gas between the H_2O and CO snow lines becomes enriched in carbon (C/O approaching $\sim$1) as water ice removes oxygen from the gas, while solids in that region are correspondingly oxygen-rich. Figure adapted from Öberg et al. (2011).

super-stellar (C/O $\sim$ 1). If instead a large fraction of the atmosphere comes from evaporating icy planetesimals or core erosion (delivering oxygen), the C/O will be pulled back down toward the stellar value or below.

Measurements of C/O in exoplanet atmospheres provide critical clues to planet formation theories. For hot Jupiters, a high atmospheric C/O ratio could indicate formation outside the water ice line with minimal later influx of O-rich solids; a lower C/O (near stellar $\sim$0.5 or sub-stellar) might suggest formation inside the ice line or significant mixing with O-rich solids (e.g., late planetesimal delivery). Beyond water, other snow lines (e.g., for CO_2 and CO) provide additional information: formation beyond the CO_2 line ($\sim$10–20 AU in many disks) but inside the CO line could yield C/O near unity, whereas beyond CO's snow line ($\geq$ 30–50 AU) the gas and solids both tend toward the stellar C/O again. In short, the radial position of a planet's assembly and the details of its accretion history (gas vs. solids accreted) will imprint on its atmospheric elemental ratios. Studies have proposed a "main sequence" of C/O versus other elemental enrichments as a function of formation distance, and comparing measured exoplanet atmospheric C/O to these models can provide clues to a planet's origin. In the context of ultra-hot Jupiters (which are found at very small separations), we expect that they formed farther out, likely beyond the snow line, and then migrated in. Thus, we might anticipate certain C/O signatures (e.g., potentially elevated C/O if the planet migrated without too much pollution).

A.4 Challenges in Measuring Exoplanetary C/O Ratios

Determining the C/O ratio in an exoplanet's atmosphere is observationally challenging as it requires detecting and quantifying both carbon-bearing and oxygen-bearing species in the atmosphere. For hot Jupiters, the most prominent oxygen carrier is H_2O vapor (with O also in CO, CO_2), and the key carbon carriers are CO, CH_4, and CO_2. Different molecules have spectral features at different wavelengths, so a broad wavelength coverage is necessary to measure a robust C/O. Until recently, most exoplanet atmosphere spectra came from the Hubble Space Telescope (HST) in the near-infrared. This bandpass covers strong H_2O absorption bands but misses the major carbon-bearing bands (e.g., CO at 4.5 μm, CH_4 at 3.3 μm). The limited wavelength range often leads to degenerate solutions. For instance, a spectrum with a muted H_2O feature could mean the planet has a high C/O ratio (true water depletion) or simply that clouds/hazes are obscuring the water feature. Early studies sometimes reported extremely high C/O ratios ($\sim$1) for some hot Jupiters (e.g., WASP-12b) based on sparse data. However, these interpretations have been subject to debate as additional observations became available.

An illustrative example is the hot Jupiter WASP-12b, which over the past decade has been observed by many teams with conflicting results. Initial analyses of Spitzer photometry and HST broadband data by Öberg et al. (2011) inferred a carbon-rich composition (C/O $\geq$ 1), which was revolutionary at the time. But subsequent observations and reanalyses cast doubt on this. In fact, at least 17 different studies attempted to characterize WASP-12b's atmosphere, some supporting C/O > 1 and others C/O < 1. Eventually, a definitive measurement required multiple HST transit observations and improved analysis: Kreidberg et al. (2015) obtained six transits of WASP-12b with an extended wavelength range and detected a clear H_2O signal. The presence of water vapor indicated a more oxygen-rich (lower C/O) atmosphere, essentially refuting the extreme carbon-rich hypothesis for that planet. This debate shows how sensitive the inference is to data quality and wavelength coverage, and thus high-precision, broad-band data and robust retrieval techniques are required to pin down C/O ratios.

Beyond HST, new facilities are alleviating these limitations. The James Webb Space Telescope (JWST) allows simultaneous detection of H_2O, CO, CH_4, and CO_2 in exoplanet atmospheres. Early JWST results (e.g., the WASP-39b transiting planet observations) have unambiguously detected multiple molecules including CO_2, which gives the first precise C/O constraints on an exoplanet. Likewise, ground-based high-resolution spectroscopy (e.g., cross-correlation techniques at $R \sim 100,000$) can identify spectral lines of CO, H_2O, etc., by their Doppler shifts. This method has successfully detected CO in the day-side spectra of several hot Jupiters, and when combined with low-resolution data, it can help constrain relative abundances. However, methodological challenges remain: high-resolution spectra usually probe the hot day-side and may not directly give absolute abundances, and combining datasets requires careful cross-calibration.

Another major challenge is clouds and hazes in exoplanet atmospheres. Many hot Jupiters have hazy atmospheres that mute spectral features, especially in transmission (terminator line-of-sight). A flat or featureless transmission spectrum can hide the signatures of H_2O or other molecules, leading to degenerate solutions for composition. For example, a high-altitude cloud deck can mask water absorption such that one could erroneously infer a high C/O ratio (since no H_2O is seen) when in reality the H_2O is present but hidden. Advanced retrieval methods attempt to marginalize over clouds, but uncertainties remain large when data quality is limited. Furthermore, temperature structure and vertical mixing affect observable spectroscopic features. In ultra-hot Jupiters, water can thermally dissociate on the dayside while CO remains stable, which can complicate the interpretation of average spectra and thus the inferred C/O.

In summary, while the C/O ratio is an important diagnostic of planet formation history, measuring it precisely in exoplanet atmospheres is non-trivial. Factors including limited spectral coverage (in past instruments), model degeneracies, and empirical obstacles like clouds lead to significant uncertainties. With the broader wavelength coverage and improved retrievals in the JWST era, we are now beginning to obtain more reliable C/O measurements for hot Jupiters. These measurements will test formation models (e.g., core accretion + migration versus other scenarios) by checking whether the inferred chemical fingerprints (such as super-solar C/O ratios) align with expectations for formation beyond the ice line. As observational capabilities advance, we expect to strengthen the synergy between planet formation theory and atmospheric characterization to paint a more complete picture of how ultra-hot Jupiters form and evolve.

References: This appendix is written based on several sources, including the comprehensive review of hot Jupiter origins and physics by Fortney et al. (2021), the Annual Reviews article by Dawson & Johnson (2018) on hot Jupiter formation theories, and the study by Öberg et al. (2011) linking disk snow lines to atmospheric C/O ratios. Additional context on observational challenges was based on the HST results of Kreidberg et al. (2015) and discussions in Barstow & Heng (2020) regarding exoplanet atmosphere retrieval techniques. Figures adapted from Fortney et al. (2021) and Öberg et al. (2011) were included for illustration.

B Spectral Diagnostics and Atmospheric Radiative Transfer

B.1 Absorption vs. Emission Spectra

Exoplanet atmospheres can be probed via emission or absorption spectra, depending on the observational geometry. In transmission spectroscopy during a transit, some starlight filters through the planet's limb. The planet's thin atmosphere imprints absorption features on the stellar spectrum. These wavelength-dependent increases in transit depth reveal atmospheric constituents of planets.

By contrast, in thermal emission spectroscopy (e.g., during secondary eclipse or phase curve observations), we observe the planet's own radiation from its day-side. At secondary eclipse the planet is eclipsed by the star, causing a drop in the combined light; the spectrum of this drop is the planet's dayside emission spectrum. Emission spectra encode both composition (as in transmission) and the atmospheric temperature structure, which transmission spectra alone cannot easily constrain. Ultra-hot Jupiters (UHJs) are especially useful to emission measurements due to their intense thermal output. (Reflected light spectra, which are generally much weaker, are typically omitted in the context of UHJs.)

B.2 Molecular Absorption Cross-Sections and Line Broadening

The spectral features of an exoplanet atmosphere arise from wavelength-dependent opacity contributed by atoms and molecules. Each gas species has a characteristic set of absorption lines (transitions) with specific wavelengths and strengths—quantified by its absorption cross-section, $\sigma(\lambda, T)$. Modern models rely on extensive line lists (e.g., the ExoMol, HITRAN and HITEMP databases) to compute these cross-sections across the relevant temperature range, and the produced synthetic spectra depends critically on the accuracy of those data sets.

Spectral lines are not infinitesimally narrow; they are broadened by physical processes. Thermal (Doppler) broadening results from the velocity distribution of gas molecules, producing a Gaussian core whose width scales with $\sqrt{T}$. Pressure (collisional) broadening arises from inter-molecular collisions in higher-pressure layers, yielding Lorentzian wings that can extend over hundreds of Å. In dense regions of a hot-Jupiter atmosphere these wings dominate the optical opacity: the Na I and K I resonance doublets at 589 nm and 770 nm often display wings spanning several atmospheric scale heights, suppressing reflected light and lowering geometric albedo. Because Doppler and collisional mechanisms act simultaneously, the resulting line shape is a Voigt profile that must be treated self-consistently in radiative-transfer calculations.

The pressure-broadened wings of alkali lines are directly observable in high-signal transmission spectra. Figure B.1 shows the Na I D feature in the clear atmosphere of WASP-96 b: its Lorentzian wings extend over $\sim$6 scale heights, strengthening the dominance of collisional broadening in the

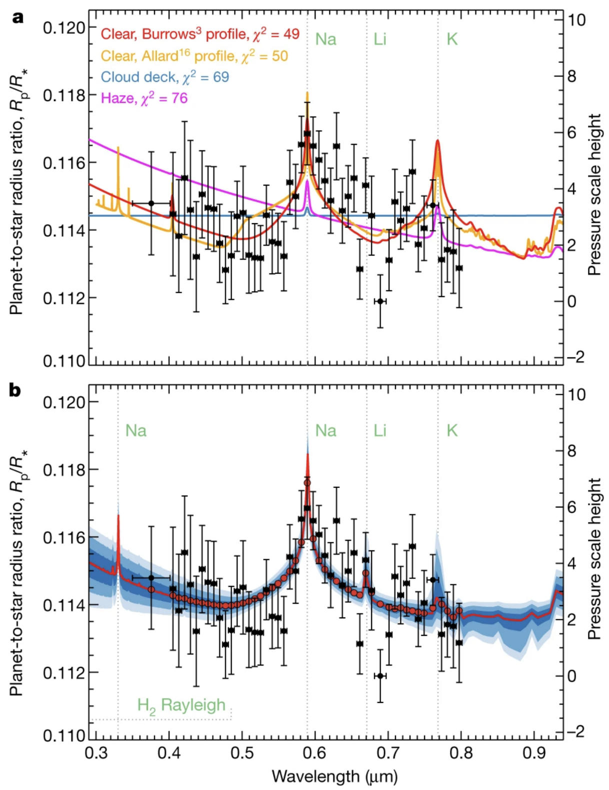

Figure B.1: Transmission spectrum of WASP-96. Black points with 1σ error bars are FORS2 transit measurements. Panel a: Clear-atmosphere forward models with two different Na/K broadening prescriptions (orange, red) match the data. Panel b: Bayesian retrieval (red curve; $1-3\sigma$ shaded bands) confirms a cloud-free atmosphere and recovers a Na line whose Lorentzian wings span ~ 6 scale heights (right axis), consistent with strong pressure broadening. Figure adapted from Nikolov et al. (2018).

lower atmosphere and the inadequacy of haze or cloud models with narrower line cores to match the data.

B.3 Radiative Transfer in a Stratified Atmosphere

Exoplanet atmospheres are typically modeled as stratified layers with pressure decreasing with altitude and a given temperature–pressure (T–P) profile. Radiative transfer through this layered atmosphere determines the emergent spectrum by governing how light is absorbed, emitted, and re-emitted by each layer. At a given wavelength, the observed flux originates from the layer where the optical depth reaches order unity (the photosphere at that wavelength). Because gas opacity varies with wavelength (due to spectral lines and continua), different wavelengths probe different altitudes. In spectral continuum regions of low opacity, we see deeper (higher-pressure) layers, whereas within an absorption line (high opacity) the photon last escapes from a higher, lower-pressure layer. If the atmosphere's temperature decreases with height (a typical non-inverted profile), a higher-altitude line-forming region will be cooler than the deeper continuum-forming region, and thus the line appears as an absorption feature (lower flux) relative to the continuum. In essence, features in molecular bands where opacity is higher appear as absorption dips in the emergent flux when the temperature falls with altitude.

B.4 Thermal Inversion and Spectral Signatures

The presence or absence of emission vs. absorption features in a planet's dayside spectrum is a direct diagnostic of the atmospheric thermal structure. In some hot exoplanets, the upper atmosphere contains an extra heating layer (a stratospheric inversion where temperature rises with altitude). In such cases, high-opacity bands that probe the hot upper layers will exhibit emission lines – the line core is formed in an inversion layer that is hotter than the deeper continuum-emitting region, yielding higher flux at line center than in the adjacent continuum. Thus, an emission line profile (line flux exceeding continuum) is unambiguous evidence of a temperature inversion in the corresponding altitude range. Conversely, if the temperature continually decreases outward (no inversion), spectral lines will appear in absorption (lower flux than continuum). Classic examples include the 1.4 μm water vapor band: in a cooler hot Jupiter like WASP-43b it appears as an absorption trough, whereas in the ultra-hot Jupiter WASP-121b the same band is observed in emission, indicating an inverted temperature profile.

Stratospheric temperature inversions in hot Jupiters was first proposed by Hubeny et al. (2003) and Fortney et al. (2008), who suggested that strong optical absorbers (TiO, VO) at high altitudes could drive such inversions. Indeed, many ultra-hot Jupiters receive such extreme stellar irradiance that species like TiO/VO, atomic metals (Fe, Ti, etc.) can absorb substantial stellar flux in the upper atmosphere, heating it enough to cause a thermal inversion. Recent high-resolution spectra have detected emission lines of neutral Fe, OH, TiO and others in the dayside spectra of UHJs, directly revealing hot inversion layers. In contrast, absence of emission features (with only absorption features or a blackbody-like featureless spectrum) suggests no strong inversion – for example, many "cooler" hot Jupiters show deep H_2O absorption bands and no sign of emission, consistent with a consistently declining T–P profile. Hence, by comparing the observed spectral line shapes with radiative transfer models, one can infer the temperature–altitude profile: emission features signal an inverted atmosphere, whereas absorption features imply a non-inverted (or even isothermal) atmosphere. Understanding whether a dayside inversion is present is important for understanding the energy balance and chemistry of these extreme worlds.

References: Core discussions of radiative-transfer formalisms and line-profile theory follow the treatments in Theory of Stellar Atmospheres by Hubeny & Mihalas (2014) and the exoplanet-focused overview by Heng (2017). The link between alkali pressure broadening and hot-Jupiter albedo is based on the forward-model analyses of Fortney et al. (2008) and the observational confirmation in Nikolov et al. (2018). Empirical diagnostics of temperature inversions are based on the seminal inversion models of Hubeny et al. (2003) and subsequent observational case studies such as Snellen et al. (2010) and Kreidberg et al. (2015). Broader context on hot-Jupiter atmospheric physics and formation is taken from the comprehensive reviews by Madhusudhan (2019) and Fortney et al. (2021).

C Brown Dwarfs and Giant Exoplanets

Brown dwarfs occupy the mass range between giant planets and low-mass stars, spanning approximately 13–75 Jupiter masses (M_J). The upper limit ($\sim$75 M_J, or 0.075 $M_\odot$) represents the minimum mass required for stable hydrogen fusion, while the lower boundary ($\sim$13 M_J) corresponds to the deuterium fusion threshold. Unlike main-sequence stars, brown dwarfs cannot sustain hydrogen fusion but may temporarily fuse deuterium during early evolution.

The effective temperatures of brown dwarfs span $\sim$250-2100 K, directly overlapping with the temperature range of giant exoplanets. Ultra-hot Jupiters can reach temperatures exceeding 2000 K, comparable to L-type brown dwarfs, while the coolest Y-type brown dwarfs (T_{eff} $\sim$250-500 K) have temperatures similar to wide-orbit giant planets. This temperature convergence results in similar atmospheric chemistry and spectral features despite different formation pathways.

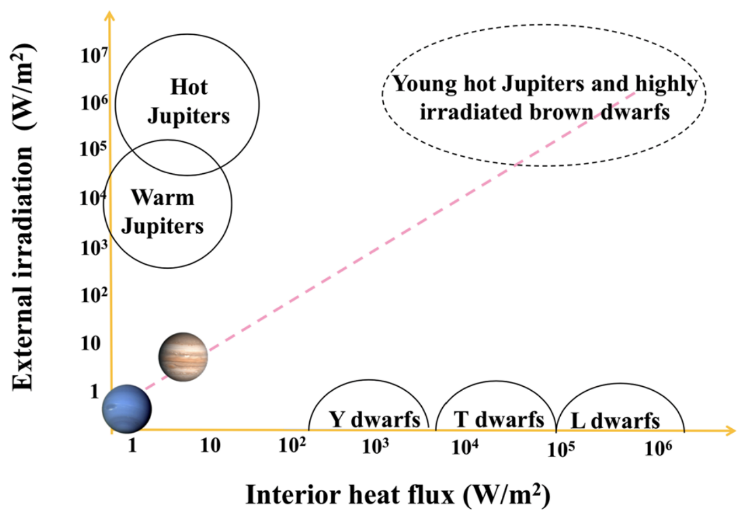

Figure C.1: Regime diagram of stellar irradiation versus interior heat flux. Solar-System giants (lower left), warm and hot Jupiters (upper left), isolated brown dwarfs (lower right), and the small sample of highly irradiated brown dwarfs/very young hot Jupiters (upper right) occupy distinct forcing regimes. The diagram shows how atmospheric circulation theories must span objects whose energy budgets differ by orders of magnitude. Figure adapted from Showman et al. (2020).

Figure C.1 places these objects in the broader forcing parameter space. The plotted global-mean stellar irradiation against interior heat flux shows four distinct regimes: Solar-System giants occupy the weak-forcing lower-left corner; hot and warm Jupiters lie at high irradiation but modest internal heat; isolated brown dwarfs cluster at high internal flux with negligible irradiation; and the emerging class of highly irradiated brown dwarfs (and very young hot Jupiters) populate the upper-right quadrant. This diagram shows the continuum from planets to brown dwarfs and how atmospheric dynamics scale across > 10 orders of magnitude in energy forcing.

Brown dwarfs are classified spectroscopically in the L-T-Y sequence. L dwarfs (1300-2100 K) show metal oxide depletion and silicate cloud formation. T dwarfs (700-1300 K) exhibit strong methane absorption and clearer atmospheres as condensates sink below the photosphere. Y dwarfs (<700 K) display ammonia features and water ice clouds. Unlike planets, brown dwarfs cool continuously throughout their lifetimes without external energy input, evolving through these spectral types sequentially.

The distinction between massive exoplanets and low-mass brown dwarfs remains challenging. While the 13 M_J deuterium-burning limit provides a theoretical boundary, several factors complicate this division:

1. Observationally, there is no clear spectroscopic difference between objects around this threshold
2. Free-floating planetary-mass objects (<13 M_J) exist independently of stars
3. Some confirmed exoplanets exceed 13 M_J yet formed in circumstellar disks

Formation mechanisms potentially offer a more fundamental distinction. Brown dwarfs form through direct gravitational collapse like stars (either in isolation or wide companions), while planets form in circumstellar disks through core accretion or disk instability. The formation-based classification better accounts for observed properties but requires context beyond mass measurements.

C.1 Cooling and Evolution of Brown Dwarfs

Brown dwarfs are born hot from the heat of gravitational contraction but inevitably cool and fade with time. Without sustained fusion to replenish core energy, a brown dwarf simply radiates away its initial thermal energy. As a result, its effective temperature and luminosity decrease steadily as it ages. This cooling causes a brown dwarf to change spectral type over time, which is a striking difference from main-sequence stars. A young brown dwarf of a given mass might begin life with a late-M or L-type spectrum (if its temperature is a few thousand Kelvin), then transition to T type as it cools through $\sim$1200 K, and eventually to a Y-type object once its temperature drops below $\sim$500 K. In other words, an individual brown dwarf will progress through the L–T–Y spectral sequence as it ages. The timescale for these changes depends on mass (more massive brown dwarfs stay warm longer), but over billions of years even the most massive brown dwarfs cool to T or Y spectral classes. This evolutionary cooling has several observable consequences. For instance, the L$\rightarrow$T transition occurs when silicate and iron clouds that dominate L-dwarf atmospheres begin to dissipate or sink below the photosphere, around 1200–1400 K. This transition is accompanied by a rapid change in near-infrared colors and often variability, as patchy cloud clearance can cause flux to emerge from deeper, hotter layers.

As the brown dwarf cools further into the T class, methane and water vapor dominate the opacity, and the object's emitted spectrum shifts to shorter infrared wavelengths. Finally, in the Y dwarf stage (below $\sim$500 K), ammonia becomes a significant absorber, and the overall luminosity is exceedingly low (comparable to a warm planet). The cooling process also drives chemical evolution: for example, the dominant carbon-bearing molecule shifts from CO in the hottest brown dwarfs to CH_4 in T dwarfs once temperatures are low enough for methane to be stable, and eventually to CO_2 and more complex hydrocarbons in the coldest Y dwarfs.

In essence, brown dwarfs can be thought of as cooling embers that gradually dim and redden, traversing a sequence of spectral changes that encapsulate a wide range of atmospheric conditions in a single object's lifetime.

C.2 Comparative Atmospheric Insights from Brown Dwarfs for Exoplanet Studies

Due to their shared characteristics, brown dwarfs provide a comparative laboratory for understanding giant exoplanet atmospheres. Brown dwarfs have been called the "bridge" between low-mass stars and gas-giant planets, and studies of their atmospheres have directly informed exoplanet research. In many cases, the same molecular species are present: brown dwarf spectra are rich in H_2O, CH_4, CO_2, Na/K, and metal hydride absorbers, analogous to the expected constituents of giant planet atmospheres.

Cloud formation is another common aspect. The silicate clouds in L dwarfs mirror the cloud decks (of sulfides, silicates, etc.) inferred in many hot Jupiter atmospheres. Moreover, both brown dwarfs and strongly irradiated exoplanets can exhibit non-equilibrium chemistry; for example, vertical mixing can dredge up CO into a methane-favored regime in T/Y dwarfs, similar to what might happen on the nightside of hot Jupiters. Despite these parallels, one key difference is external irradiation: unlike close-in exoplanets, isolated brown dwarfs lack a parent star's insolation, so their thermal structures are governed purely by internal heat. This means brown dwarf atmospheres are generally vertically well-mixed and cooling-driven, whereas hot Jupiters have intense stellar heating (often causing temperature inversions or day-night dichotomies). Still, the fundamental physics of molecular opacities, radiative transfer, and chemistry is the same, so brown dwarfs serve as excellent testbeds for models that can later be applied to exoplanets.

Observationally, the techniques used to characterize exoplanet atmospheres (near-IR spectroscopy, spectral retrievals) were first honed on brown dwarfs, which are easier to observe in isolation. For instance, high-precision spectra from JWST are now available for some of the coldest brown dwarfs, reaching regimes comparable to temperate exoplanets. A recent JWST observation of a Y0 dwarf revealed a wealth of molecules (H_2O, CH_4, CO_2, CO, NH_3), and the data confirm that brown dwarf atmospheres have a complex chemistry akin to that of giant planets. Those detections allow for validation of atmospheric models under extreme conditions of low temperature and pressure.

In summary, the study of brown dwarfs' atmospheres – their spectra, cloud dynamics, and cooling evolution, provides important context for interpreting observations of giant exoplanets. Brown dwarfs and ultra-hot Jupiters can be viewed as part of a continuum of ultra-cool to ultra-hot gaseous worlds, and insights gained from one directly enhance our understanding of the other.

References: Brown dwarf and exoplanet property comparisons are synthesized from literature including Kirkpatrick (2005); Showman et al. (2020); Saur et al. (2021); Lew et al. (2024).

D Broadband and Narrowband Spectral Analysis

Here we present the detailed light curve fits and diagnostic information for the broadband (200 Å) and narrowband (4 Å) spectral analyses of WASP-178b.

D.1 Broadband Analysis (200 Å Bins)

Figure D.1 shows an example transit light curve fit for the 2278-2478 Å bin at 200 Å resolution. The raw light curve (grey) is well represented by the fitted model, and after the removal of systematics, the corrected flux closely follows the `batman` transit model.

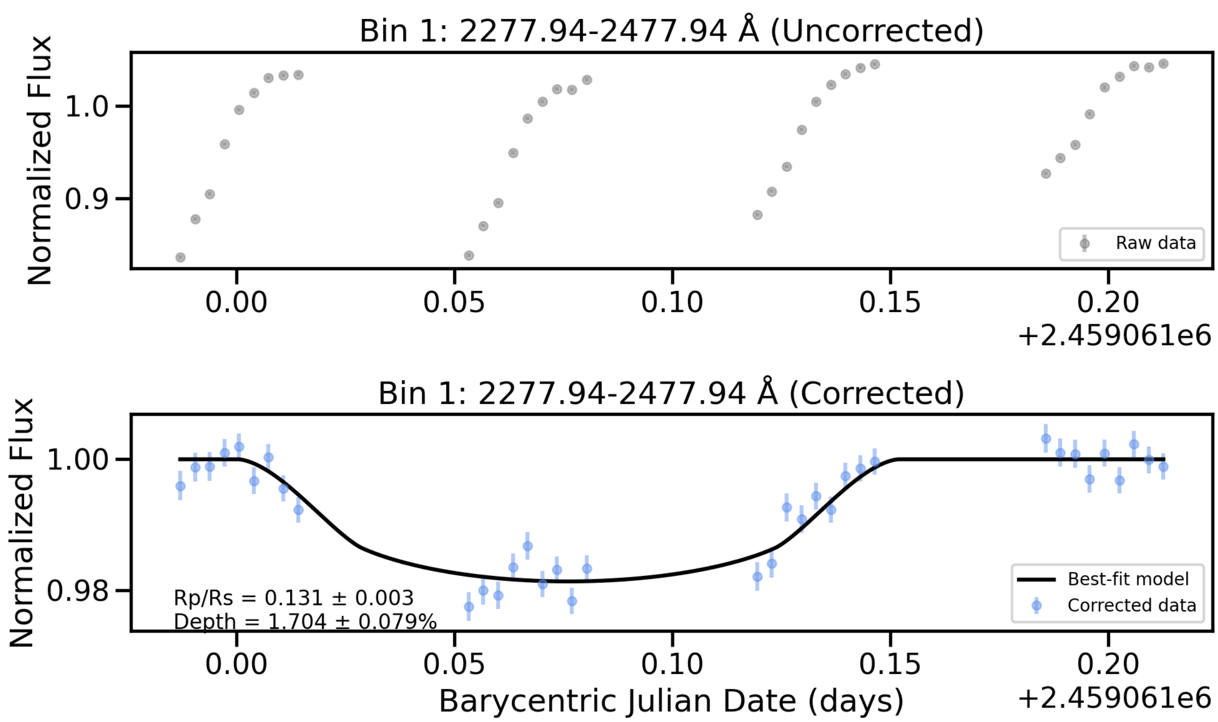

Figure D.1: Example transit light curve fit for Bin 1 (2278-2478 Å) at 200 Å resolution. The top panel shows the raw light curve and best-fit model. The middle panel displays the corrected flux after systematic removal with the transit model overlaid. The bottom panel shows the fit residuals.

The complete broadband transmission spectrum is shown in Figure D.2. While the profile appears mostly flat across most of the 2280-3100 Å range, there is a significant increase in the measured $R_p(\lambda)/R_\star$ at wavelengths shorter than 2500 Å, indicating enhanced opacity in this region.

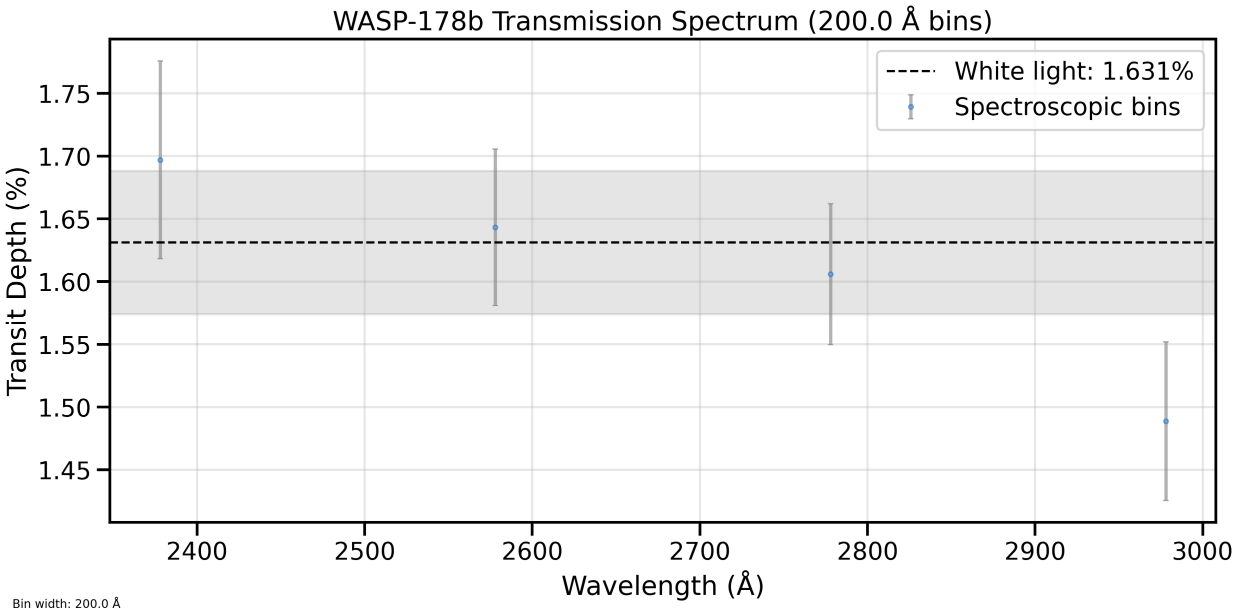

Figure D.2: Broadband (200 Å) NUV transmission spectrum of WASP-178b.

D.2 Narrowband Analysis (4 Å Bins)

Figure D.3 shows a representative transit light curve for the 2598-2602 Å bin at 4 Å resolution. The corrected flux (after applying the common-mode correction) yields a slightly deeper transit depth compared to the broadband analysis. The 4 Å binned transmission spectrum in Figure D.4 shows increased scatter relative to the 200 Å spectrum, as expected given the reduced number of photons per bin.

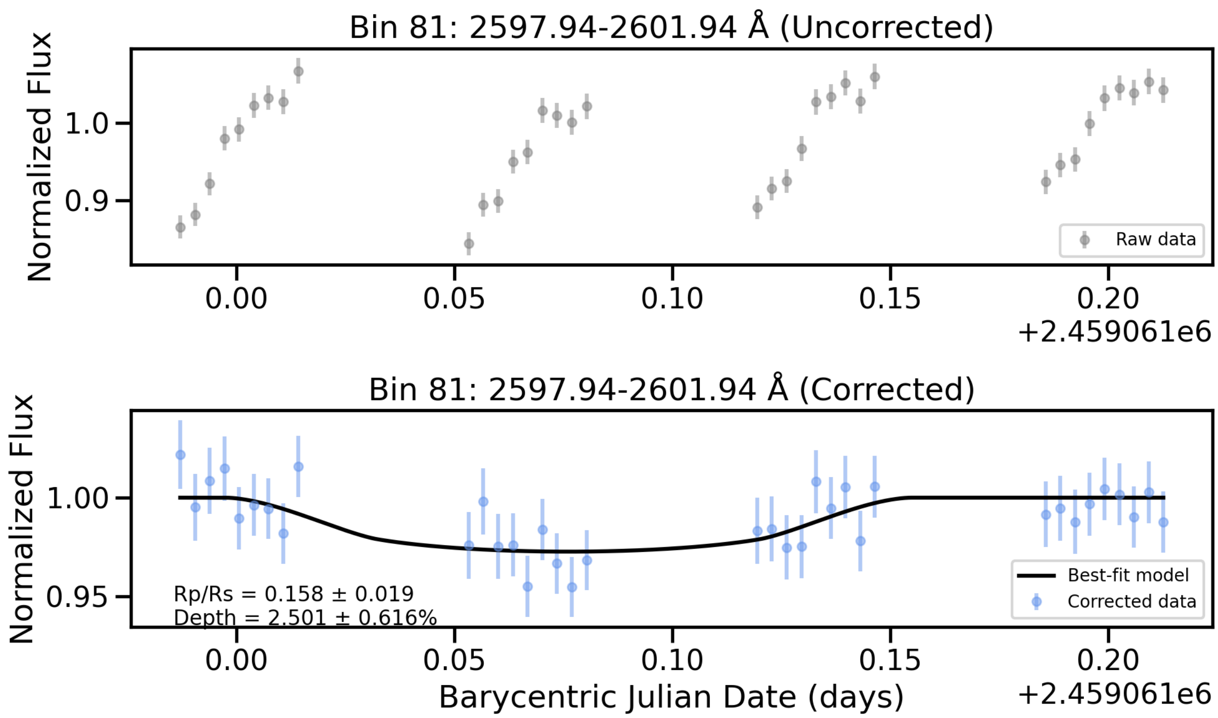

Figure D.3: Example transit light curve fit for Bin 81 (2598-2602 Å) at 4 Å resolution. The top panel shows the raw light curve and best-fit model. The middle panel displays the corrected flux after systematic removal with the transit model overlaid. The bottom panel shows the fit residuals.

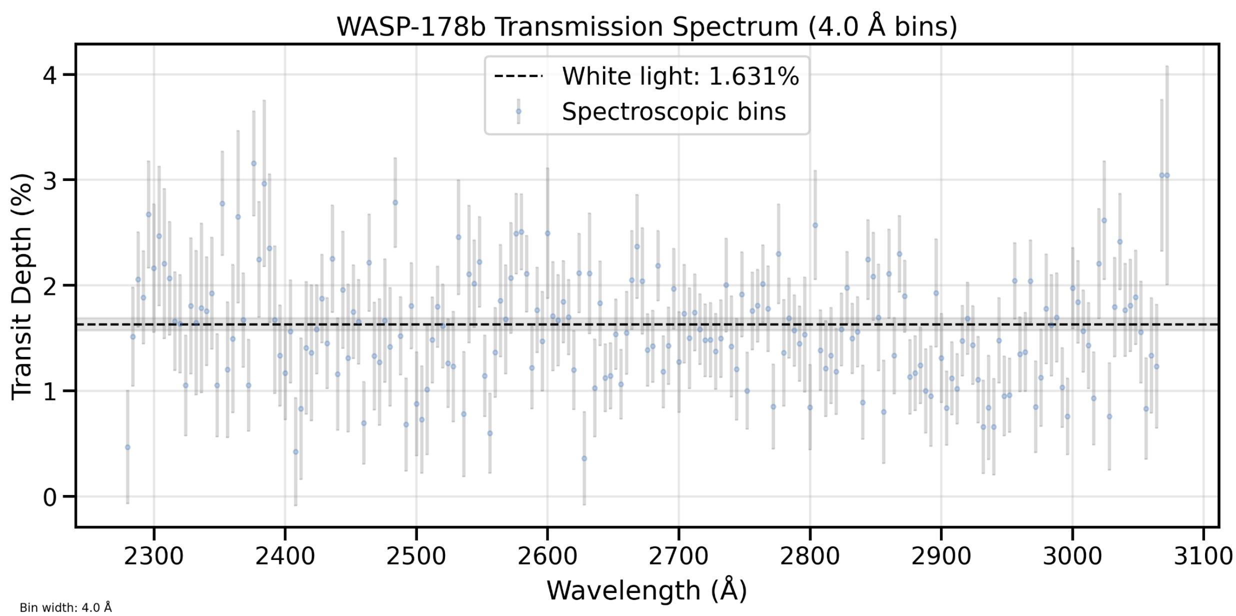

Figure D.4: Narrowband (4 Å) NUV transmission spectrum of WASP-178b. The increased resolution shows finer spectral features at the expense of larger uncertainties.

E HST/STIS Data Reduction Procedures

The raw STIS E230M data for WASP-178b were processed using version 3.4.2 of the `calstis` pipeline. These calibration steps below ensure that the output spectra are properly corrected for instrumental effects and accurately calibrated in both wavelength and flux:

- **Data Quality Initialization (DQICORR):** Flagging of known bad pixels using the bad pixel table (BPIXTAB) and checking for saturation.
- **Low-Resolution Conversion (LORSCORR):** Converting high-resolution MAMA data to low-resolution format for subsequent processing.
- **Global Linearity Correction (GLINCORR):** Correcting for detector non-linearities using the MAMA linearity table (MLINTAB).
- **Local Flagging Correction (LFLGCORR):** Flagging pixels affected by local and global non-linearities.
- **Dark Current Subtraction (DARKCORR):** Removal of detector dark current using a reference dark image (DARKFILE) with time-dependent corrections applied via the TDC table (TDCTAB).
- **Flat-Field Correction (FLATCORR):** Adjustment for pixel-to-pixel sensitivity variations using pixel flat fields (PFLTFILE) and low-order flats (LFLTFILE).
- **Doppler Correction (DOPPCORR):** Convolution of reference files with orbital Doppler shift to account for HST's orbital motion.
- **Wavelength Calibration (WAVECORR):** Using contemporaneous wavelength calibration exposures to adjust the wavelength zeropoint.
- **1D Spectral Extraction (X1DCORR):** Extraction of one-dimensional spectra using an unweighted extraction algorithm (XTRACALG='UNWEIGHTED') with parameters from the spectrum trace table (SPTRCTAB) and extraction parameters table (XTRACTAB).
- **Background Subtraction (BACKCORR):** Removal of background (sky and interorder) contamination.
- **Dispersion Correction (DISPCORR):** Application of the 2D dispersion solution using the dispersion coefficient table (DISPTAB) and incidence angle corrections (INANGTAB).

- **Heliocentric Correction (HELCORR):** Conversion to heliocentric wavelengths with a correction of 25.32 km/s.
- **Flux Calibration (FLUXCORR):** Conversion to absolute flux units using the photometric throughput table (PHOTTAB), with time-dependent sensitivity corrections applied via the TDS table (TDSTAB).
- **2D Scattered Light Correction (SC2DCORR):** Correction for scattered light using echelle scattering tables (ECHSCTAB), cross-disperser scattering tables (CDSTAB), and echelle ripple tables (RIPTAB).

F ExoCross Implementation

To generate high-resolution SiO cross-sections, we used `ExoCross` version 1.5.7. The software accepts several input formats (e.g., ExoMol, HITRAN) and supports various line profiles including Doppler, Lorentzian, and Voigt, with options for accurate Voigt profile simulations and the super-line method. Its parallelized and vectorized implementation enables efficient handling of the large datasets typical of exoplanet spectroscopy.

The Hubble Space Telescope's STIS E230M instrument has a resolving power of $R \sim 30,000$, which at a central wavelength of ~ 2707 Å translates into a resolution element of approximately 0.09 Å. In wavenumber space, this corresponds to a full width at half maximum (FWHM) of

$$\Delta\tilde{\nu} \approx \frac{0.1\,\text{Å}}{(2.707 \times 10^{-5}\,\text{cm})^2} \approx 1.23\,\text{cm}^{-1}.$$

Since ExoCross uses a Gaussian profile defined by its half-width at half-maximum (HWHM), we set

$$\text{HWHM} \approx \frac{1.23}{2} \approx 0.62\,\text{cm}^{-1}.$$

A high-resolution grid with 25001 wavenumber points was adopted to ensure that all spectral details are well sampled.

An example ExoCross input file for generating the SiO absorption cross section at $T = 2470$ K is shown below:

```
Temperature 2470.0
Range 32573.0 43860.0
Npoints 25001
absorption
Gaussian
HWHM 0.62 (cm-1)
output SiO_gauss_2470K_R30000
States 28Si-16O__SiOUVenIR.states
Transitions 28Si-16O__SiOUVenIR.trans
```

This file instructs ExoCross to:

- Compute the absorption spectrum for SiO at 2470 K.
- Cover the wavenumber interval corresponding to the 2280-3070 Å range.
- Use a grid of 25001 points for fine sampling.

- Convolve the spectrum with a Gaussian profile of HWHM 0.62 cm^{-1} (matching $R \sim 30,000$).
- Read the molecular data from the ExoMol-formatted files `28Si-16O__SiOUVenIR.states` and `28Si-16O__SiOUVenIR.trans`.

`ExoCross` is compiled via a provided makefile. Once compiled, the executable (located in the `exe` folder) is run as follows:

```
./exe/exocross.exe < SiO_gauss_2470K_R30000.inp > SiO_gauss_2470K_R30000.out
```

The output file contains the computed cross sections as a function of wavenumber, which were subsequently converted to wavelength space for analysis. Further details on ExoCross's capabilities can be found in its documentation[5].

Post-processing of the ExoCross output was performed in Python using the following procedure:

- 1. Read the output file containing wavenumbers and corresponding cross-sections
- 2. Convert wavenumbers to wavelengths in Angstroms using Equation 15
- 3. Normalize the cross-sections to the maximum value to facilitate analysis
- 4. Apply a peak-finding algorithm to identify local maxima representing strong absorption features
- 5. Apply threshold criteria to select the strongest features for the in-band/out-of-band analysis

[5] https://exocross.readthedocs.io/

G Glossary

G.1 Exoplanet Terminology

Albedo Fraction of incident stellar radiation reflected by a planet's atmosphere or surface.

Day–night contrast Temperature difference between the substellar and antistellar hemispheres of a tidally locked planet.

Eclipse Occultation of a planet by its host star (secondary eclipse), seen as a drop in combined flux.

Emission spectroscopy Measurement of a planet's thermal emission spectrum, typically during secondary eclipse.

Equilibrium temperature Temperature at which absorbed stellar flux balances emitted thermal flux, assuming blackbody emission, specified albedo, and heat redistribution.

Exoplanet Planet orbiting a star other than the Sun.

Hot Jupiter Gas giant with orbital period ≤ 10 days and equilibrium temperature ≥ 1000K.

Phase curve Variation of system brightness with orbital phase, sensitive to atmospheric circulation and heat transport.

Photometry Measurement of stellar flux versus time or wavelength to detect transits, eclipses, and phase variations.

Transit Passage of a planet across the stellar disk, causing a flux decrement.

Transit depth Relative drop in stellar flux during transit, derived as:

$$\delta = \frac{\Delta F}{F_\star} = \frac{F_\star - F_{\rm obs}}{F_\star} = \frac{\pi R_p^2}{\pi R_\star^2} = \left(\frac{R_p}{R_\star}\right)^2.$$

Transmission spectroscopy Measurement of wavelength–dependent transit depths to infer atmospheric composition via differential absorption.

Ultra-hot Jupiter (UHJ) Subclass of hot Jupiters with equilibrium temperature ≥ 2200K.

G.2 Atmospheric Chemistry and Physics

Absorption cross-section Probability per molecule of absorbing radiation at a given wavelength (cm^2/molecule).

Atmospheric scale height (H) Vertical e-folding length of an isothermal, hydrostatic atmosphere. Starting from hydrostatic balance

$$\frac{dP}{dz} = -\rho g,$$

and an ideal–gas equation of state $P = \rho R'T = \rho \frac{k_B T}{\mu m_H}$, we obtain

$$\frac{d\rho}{dz} = -\frac{\rho}{H}, \qquad \rho(z) = \rho_0 e^{-z/H}, \qquad P(z) = P_0 e^{-z/H},$$

with

$$H = \frac{R'T}{g} = \frac{RT}{Mg} = \frac{k_B T}{\mu m_H g},$$

where T is temperature, g surface gravity, R the universal gas constant, $R' = R/M$ the specific gas constant, and μm_H the mean molecular mass. Numerically

$$H = 7.5 \text{ km} \left(\frac{T}{288 \text{ K}}\right)\left(\frac{29 \text{ g mol}^{-1}}{M}\right)\left(\frac{9.81 \text{ m s}^{-2}}{g}\right).$$

Thus a 1500 K hot-Jupiter ($g \sim 20 \text{ m s}^{-2}$, $\mu \approx 2.3$) has $H \sim 55$ km ($\sim 7 H_\oplus$), while an ultra-hot Jupiter at 2500 K reaches $H \sim 90$ km ($\sim 12 H_\oplus$).

Band structure A pattern of densely spaced spectral lines appearing as a broader absorption feature.

Chemical equilibrium State in which forward and reverse chemical reaction rates are equal, yielding fixed abundances at given T, P.

Condensation Phase transition from gas to liquid or solid upon cooling below saturation.

Continuum opacity Smoothly varying background absorption or scattering, excluding discrete lines or bands.

Hydrostatic equilibrium Condition in which the vertical pressure-gradient force balances gravity, so parcel accelerations are negligible:

$$\frac{dP}{dz} = -\rho g.$$

Using the ideal-gas law, $P = \rho R'T = \rho \frac{k_B T}{\mu m_H}$, $\rho = \frac{P}{R'T}$, this can be rewritten in two equivalent forms

$$\boxed{\frac{dP}{dz} = -\frac{g}{R'T} P} \quad \text{and} \quad \boxed{\frac{d(\rho T)}{dz} = -\frac{g}{R'} \rho}.$$

For an isothermal atmosphere these integrate to the exponential profiles above; for a non-isothermal column

$$P(z) = P_0 \exp\left[-\int_0^z \frac{g}{R'T(z')} dz'\right],$$

so the lapse-rate dT/dz directly modulates the vertical pressure (and density) structure. Hydrostatic equilibrium underpins 1-D radiative–convective, retrieval, and general-circulation models of planetary atmospheres.

Line list Database of atomic or molecular transition wavelengths, strengths, and quantum data.

Local thermodynamic equilibrium (LTE) Each small parcel is "locally" in TE even if it's not in global equilibrium, holds in deeper atmosphere layers where collision rates are high.

Metallicity Abundance of elements heavier than helium, often expressed [Fe/H] relative to solar.

Mixing ratio Number density of a species divided by total number density (e.g., ppm, ppb).

Opacity The measure of a material's ability to absorb or scatter electromagnetic radiation, determining how effectively it impedes the transmission of light.

Photochemistry Photon-driven chemical processes (e.g., photolysis, where a molecule is broken down into smaller components by absorbing light), dominant in upper atmospheres.

Pressure broadening The widening of spectral lines due to collisions between atoms or molecules at higher atmospheric pressures.

Radiative (and radiative–convective) equilibrium Thermal balance in which net absorption of stellar + thermal photons = net emission of thermal photons at each layer. If a layer would become unstable, radiative heating/cooling and convective transport jointly determine the temperature–pressure profile. Typically used to compute the temperature-pressure profile ($T-P$) structure of the atmosphere, standard for 1D climate model:

$$\int \kappa_\nu \big(J_\nu - B_\nu(T)\big)\, d\nu \;=\; 0 \quad \longrightarrow \quad T(z)$$

(κ_ν: opacity, J_ν: mean intensity, B_ν: Planck function)

Refractory species High–condensation-temperature materials (e.g., silicates, metal oxides) that remain solid at elevated temperatures.

SiO (Silicon monoxide) A gaseous molecule expected to be present in the atmospheres of ultra-hot Jupiters($T_{eq} \geq 2200$K).

Temperature-pressure profile A description of how temperature varies with pressure (or altitude) in a planetary atmosphere.

Thermodynamic equilibrium (TE) Entire system has a single T, P, and uniform composition; no net flows of heat, matter, or radiation. The ideal state toward which systems relax.

Thermochemical equilibrium Rates of every forward reaction = rates of reverse. Composition is set by minimizing Gibbs free energy at each T, P. Typically used for deep hot layers when chemical timescales $\ll$ mixing timescales and to predict bulk abundances of chemical species.

Thermal dissociation Molecular bond breaking at high temperature, producing atoms or simpler molecules.

Thermal inversion Layer where temperature increases with altitude, driven by strong absorption of stellar radiation.

Volatile species Low–condensation-temperature compounds (e.g., H_2O, CH_4) that remain gaseous at moderate temperatures.

G.3 Data Analysis and Statistical Methods

AIC (Akaike Information Criterion) Model-selection statistic balancing fit and complexity:

$$\mathrm{AIC} = 2k \,-\, 2\ln\bigl(L_{\max}\bigr),$$

where k is the number of free parameters and $L_{\max}$ the maximum likelihood. Lower AIC indicates a preferred model.

AICc A corrected version of AIC adjusted for small sample sizes:

$$\mathrm{AICc} = \mathrm{AIC} \,+\, \frac{2k(k+1)}{n-k-1},$$

where n is the number of data points. Approaches AIC as $n \to \infty$.

BIC (Bayesian Information Criterion) A criterion for model selection that penalizes complex models more strongly than AIC:

$$\mathrm{BIC} = k\ln n \,-\, 2\ln\bigl(L_{\max}\bigr).$$

Binning Combine adjacent data points into m bins of width $\Delta\lambda$. For fluxes F_j in bin i:

$$F_i = \frac{1}{N_i}\sum_{j\in i} F_j, \quad \sigma_i = \frac{1}{N_i}\sqrt{\sum_{j\in i}\sigma_j^2}.$$

χ^2 statistic Goodness-of-fit measure for independent, Gaussian errors:

$$\chi^2 = \sum_{i=1}^{N} \frac{\bigl(y_i - y_i^{\text{model}}\bigr)^2}{\sigma_i^2} \;\sim\; \chi^2_\nu \quad (\nu = N-k \text{ d.o.f.}),$$

where k is the number of fitted parameters. The *reduced* chi-squared, $\chi^2_\nu = \chi^2/\nu$, should be ≈ 1 for an adequate model; values $\ll 1$ indicate over-estimated uncertainties, $\gg 1$ suggest poor model or under-estimated errors.

Gaussian distribution (Normal) Probability density

$$f(x;\mu,\sigma) = \frac{1}{\sigma\sqrt{2\pi}}\exp\Bigl[-\tfrac{(x-\mu)^2}{2\sigma^2}\Bigr].$$

Encloses 68.27% within $\pm1\sigma$, 95.45% within $\pm2\sigma$, 99.73% within $\pm3\sigma$.

In-band/Out-of-band technique A method for molecular detection that compares transit depths at wavelengths where a specific molecule is expected to absorb strongly (in-band, $\delta_{\rm in}$) versus wavelengths where it is not (out-of-band, $\delta_{\rm out}$).

Null hypothesis (H_0) The default position that there is no relationship between two measured phenomena or no difference between groups.

One-tailed test Rejection region in only one tail of the distribution (e.g. testing for an increase only).

p-value Probability, under the null hypothesis H_0, of obtaining a test statistic at least as extreme as the observed one:

$$p = P\left(T \geq T_{\rm obs} \,\middle|\, H_0\right).$$

Interpreting the strength of evidence usually relies on the Gaussian-equivalent significance level, Z (in "σ" units). For a *two-sided* test in a normal distribution, the most common pairs are

$$\begin{aligned} Z = 1\sigma &\quad \Rightarrow\ p \simeq 0.3173 \\ Z = 2\sigma &\quad \Rightarrow\ p \simeq 4.55 \times 10^{-2} \\ Z = 3\sigma &\quad \Rightarrow\ p \simeq 2.70 \times 10^{-3} \\ Z = 4\sigma &\quad \Rightarrow\ p \simeq 6.33 \times 10^{-5} \\ Z = 5\sigma &\quad \Rightarrow\ p \simeq 5.73 \times 10^{-7} \end{aligned}$$

An often used threshold for "statistical significance" in many fields is $p < 0.05$ ($\approx 2\sigma$).

Root-mean-square (rms) Quadrature average of a set—or of residuals:

$$\text{rms} = \sqrt{\frac{1}{n}\sum_{i=1}^{n} x_i^2}, \qquad \text{rms}_{\rm res} = \sqrt{\frac{1}{n}\sum_i (y_i - y_i^{\rm model})^2}.$$

The rms of residuals offers an alternative (units-consistent) measure of overall fit quality, complementing χ^2_ν.

Savitzky–Golay filter Local polynomial-regression smoother that fits a degree-p polynomial to each sliding window of $2M+1$ points and replaces the centre point with the value (or derivative) of that polynomial. Preserves peaks and higher-order moments better than boxcar or Gaussian smoothing provided the window half-width M is $\gtrsim$ the feature width.

Sensitivity analysis Set of techniques that deliberately vary model inputs to quantify their influence on chosen outputs.

Signal-to-noise ratio (SNR) Ratio of a signal's coherent amplitude to the standard deviation of the uncorrelated noise:

$$\text{SNR}_{\rm linear} = \frac{\mu_{\rm signal}}{\sigma_{\rm noise}}$$

In photon counting, SNR $\approx \sqrt{N_\gamma}$ when the noise is dominated by Poisson statistics.

Standard deviation (σ) Unbiased estimator of a sample's dispersion,

$$\sigma = \sqrt{\frac{1}{n-1}\sum_{i=1}^{n}(x_i - \bar{x})^2},$$

equal to the square root of the second central moment.

Standard error of the mean (SEM) Standard deviation of the sampling distribution of $\bar{x}$; quantifies the precision on the population mean:

$$\text{SEM} = \frac{\sigma}{\sqrt{n}}.$$

***t*-statistic** Measures how many *standard errors* an estimate $\hat{\theta}$ lies from a null value θ_0:

$$t = \frac{\hat{\theta} - \theta_0}{\text{SEM}} \sim t_\nu \quad (\text{under } H_0),$$

where t_ν is Student's t distribution with $\nu = n - 1$ (one-sample case) degrees of freedom.

- $|t| \approx 2$ ($\nu \gtrsim 30$) $\Rightarrow$ two-sided $p \simeq 0.05$ ($\sim 2\sigma$).
- $|t| \approx 3 \Rightarrow p \simeq 0.003$ ($\sim 3\sigma$).
- In practice one compares $|t|$ to critical values or converts to a p-value; if $p < \alpha$ (e.g. 0.05) the null hypothesis that $\hat{\theta} = \theta_0$ is rejected at significance level α.

Welch's *t*-test Two-sample test allowing unequal variances:

$$t = \frac{\bar{x}_1 - \bar{x}_2}{\sqrt{\frac{s_1^2}{n_1} + \frac{s_2^2}{n_2}}}, \qquad \nu = \frac{\left(\frac{s_1^2}{n_1} + \frac{s_2^2}{n_2}\right)^2}{\frac{s_1^4}{n_1^2(n_1-1)} + \frac{s_2^4}{n_2^2(n_2-1)}}.$$

G.4 Computational Modeling and Simulations

Atmospheric retrieval Bayesian inference of deriving atmospheric properties (e.g. composition, pressure–temperature profile, clouds) by fitting forward models to observed spectra. Widely used codes include TauREx (Waldmann et al., 2015), petitRADTRANS (Mollière et al., 2019), HELIOS-R (Lavie et al., 2017) and HELIOS-R2 (Kitzmann et al., 2020).

Cross-correlation Measures similarity between an observed spectrum $F(\lambda)$ and a Doppler-shifted template $T(\lambda)$:

$$C(v) = \sum_i F(\lambda_i)\, T\big(\lambda_i(1 + v/c)\big),$$

where the correlation peak at v indicates the planet's radial velocity; the method is fundamental to high-resolution molecular detections.

Detrending Removal of instrumental and astrophysical systematics (e.g. HST "ramp" and pointing jitter) by regressing residual flux against auxiliary variables (time, orbital phase, engineering telemetry).

ExoCross Fortran 2003 program to compute pressure- and temperature-dependent molecular cross-sections from ExoMol or HITRAN line lists, optimized for billions of transitions via efficient Voigt profile algorithms.

ExoMol Database of comprehensive high-temperature molecular line lists for exoplanet and stellar atmospheres, computed via variational quantum methods and empirical tuning.

Forward model Predicts observables (transmission/emission spectra) from a parameterized atmosphere (composition, P–T profile, clouds, limb darkening) using radiative transfer. Integral part of retrieval algorithms.

General circulation model (GCM) Three-dimensional computational framework that simulates the complete atmospheric physics of a planet, incorporating both fluid dynamics and radiative processes. Unlike simpler 1D models, GCMs can represent asymmetric features like equatorial jets, vortices, and day-night contrasts, making them particularly useful for interpreting phase-resolved observations of tidally-locked exoplanets.

Limb darkening Wavelength-dependent stellar intensity drop from disk center ($\mu = 1$) to limb ($\mu = 0$); commonly used laws include:

$$\frac{I(\mu)}{I(1)} = 1 - u\,(1-\mu) \quad \text{(linear)},$$

$$\frac{I(\mu)}{I(1)} = 1 - a\,(1-\mu) - b\,(1-\mu)^2 \quad \text{(quadratic)},$$

$$\frac{I(\mu)}{I(1)} = 1 - \sum_{i=1}^{4} c_i\big(1-\mu^{i/2}\big) \quad \text{(Claret 4-parameter)},$$

with biases at high precision; fitting or fixing these coefficients impacts transit-depth inference.

petitRADTRANS Python package (with Fortran core) for fast computation of transmission and emission spectra via correlated-k (low resolution) and line-by-line (high resolution) methods; supports clouds, scattering and nested-sampling retrievals.

PHOENIX General-purpose stellar and planetary atmosphere code solving radiative transfer (LTE, NLTE) in 1D spherical or 3D geometries; produces synthetic spectra for stars, brown dwarfs and exoplanets.

Radiative transfer Describes change in specific intensity I_ν along a path s:

$$\frac{dI_\nu}{ds} = -\alpha_\nu I_\nu + j_\nu = \alpha_\nu\big[B_\nu(T) - I_\nu\big],$$

where α_ν is absorption coefficient, j_ν emission coefficient, and B_ν the Planck function under LTE.

G.5 Molecular Spectroscopy and Line List

A–X band Electronic transition $A^1\Pi \to X^1\Sigma^+$ in SiO, producing strong ultraviolet absorption between roughly 2140 Å and 2818 Å, with multiple vibrational–rotational sub-bands converging into bandheads.

E–X band Electronic transition $E^1\Sigma^+ \to X^1\Sigma^+$ in SiO, with measured radiative lifetimes $\tau \approx 10.5 \pm 1.1\,\mathrm{ns}$ for vibrational levels $v' = 1$–7.

Electronic state Discrete energy level of a molecule specified by a term symbol ${}^{2S+1}\Lambda^{\pm}_{g/u}$ (e.g. X, A, B, C...), arising from quantized electronic configurations along the internuclear axis.

Electronic transition Change between electronic states $i \to f$ upon absorption or emission of a photon of energy $h\nu = E_f - E_i$, governed by Einstein coefficients A_{if}, B_{if} and selection rules $\Delta\Lambda = 0, \pm 1$.

Fundamental band Vibrational transition $v = 0 \to 1$ in a diatomic molecule(molecules composed of two atoms), with band center wavenumber approximately $\tilde{\nu} \approx \omega_e(1 - 2x_e)$; appears in the infrared.

HWHM (Half-Width at Half-Maximum) Half of the full width at half maximum (FWHM) for a symmetric line shape. For a Lorentzian profile

$$L(\nu) = \frac{1}{\pi}\frac{\gamma}{(\nu - \nu_0)^2 + \gamma^2}, \quad \mathrm{HWHM} = \gamma$$

where γ is the half-width parameter.

MARVEL (Measured Active Rotational–Vibrational Energy Levels) Inversion algorithm that converts experimentally assigned line positions into a self-consistent set of empirical energy levels via least-squares fitting across multiple vibronic bands.

Ro-vibrational transition Combined change in vibrational ($\Delta v \neq 0$) and rotational ($\Delta J = \pm 1$) quantum numbers, producing P- and R-branch lines in the infrared.

Rotational transition Pure rotational change ($\Delta v = 0$, $\Delta J = \pm 1$) yielding microwave or far-infrared lines.

Sub-band Subset of lines within a band.

Vibrational transition Change in vibrational quantum number ($\Delta v = \pm 1, \pm 2, \ldots$), yielding infrared lines.

Vibronic transition Simultaneous electronic and vibrational change ($\Delta\Lambda \neq 0$, $\Delta v \neq 0$), forming band systems (e.g. A–X, E–X) with sub-bands and bandheads.

G.6 Observational Instruments and Techniques

Background subtraction Removal of sky glow, detector dark current, scattered light, and other additive signals to recover the target spectrum's true counts. Modern pipelines employ two-dimensional modelling or off-source nods before optimal extraction to minimise residuals.

COS (Cosmic Origins Spectrograph) HST ultraviolet spectrograph with separate FUV (115–205 nm) and NUV (170–320 nm) channels; medium-resolution modes reach $R \sim 24\,000$ and maximise throughput via single-bounce optics, enabling sub-magnitude fainter targets than STIS at comparable resolution.

E230M STIS NUV echelle grating delivering $R \sim 30\,000$ over 1607–3129 Å; the 2707 Å setting (used here) yields 23 orders spanning 2280–3070 Å with ≈0.10 Å pixel^{-1} dispersion and a 0.2 slit.

Echelle format Two-dimensional spectral format produced by high-blaze-angle echelle gratings: wavelength disperses along each order and decreases step-wise between adjacent orders, giving high spectral coverage at constant resolving power.

Echelle grating Diffraction grating operated at high incidence angle ($m \gg 1$) to achieve large path-length differences and hence high resolving power; cross-dispersed by a secondary element to separate overlapping orders.

ESPRESSO Fibre-fed, thermally stabilised échelle spectrograph on the VLT. HR mode ($R \sim 140\,000$) and UHR mode ($R \sim 190\,000$) target cm s^{-1} radial-velocity precision for terrestrial-planet searches; MR mode combines light from all four 8.2 m Unit Telescopes.

Extraction aperture Detector region (in pixels or arcseconds) summed during spectral extraction. A trade-off between maximising signal and excluding scattered light; optimal extraction weights pixels by their variance profile.

Flat fielding Division by a normalised flat-field frame to correct pixel-to-pixel sensitivity variations and illumination gradients, preserving relative spectrophotometry across orders.

Flux calibration Conversion from counts s^{-1} to physical flux units (erg s^{-1} cm^{-2} Å^{-1}) via standard stars and instrument throughput curves; corrects for blaze function in echelle data.

HST (Hubble Space Telescope) 2.4 m Earth-orbiting observatory operating since 1990; instruments cover 0.1–2.5 µm, deliver spectroscopy up to $R \sim 114\,000$ (STIS E140H).

JWST (James Webb Space Telescope) 6.6 m infrared observatory at L2 (launched 2021). Instruments collectively span 0.6–28.5 µm; NIRSpec offers multi-object $R \sim 100, 1000, 2700$, while MIRI provides imaging and IFU spectroscopy out to 28 µm.

NUV (Near-ultraviolet) Electromagnetic window from 200–400 nm (2000–4000 Å); overlaps the short-wavelength end of WFC3/UVIS and the long-wavelength end of STIS/COS UV capability.

Order merging Post-extraction process that stitches overlapping echelle orders into a single continuous 1-D spectrum, typically by blaze-correcting and signal-weighted averaging in overlap regions.

Spectral resolution (R) Resolving power $R = \lambda/\Delta\lambda$; defines the smallest separable wavelength interval. High-resolution spectroscopy ($R > 10,000$) resolves thermal and dynamical line broadening in exoplanet atmospheres.

STIS (Space Telescope Imaging Spectrograph) HST instrument offering long-slit spectroscopy from 115 nm–1.03 μm, UV echelle modes up to $R \sim 114\,000$, time-tagged photon counting, solar-blind imaging, and coronagraphy.

Wavelength calibration Establishes pixel-to-wavelength solution using arc lamps (UV/optical) or atmospheric night-sky lines (near-IR); typical residuals are <0.5 pix, equivalent to <1 km s^{-1} at high resolution.

WFC3 (Wide Field Camera 3) HST third-generation imager/spectrograph with UVIS (200–1000 nm) and IR (0.8–1.7 μm) channels; provides low-resolution slitless grism spectroscopy (UVIS G280, IR G102/G141) and high-precision spatial-scanning photometry.

References

Ahrer E.-M., et al., 2022, Identification of carbon dioxide in an exoplanet atmosphere, doi:10.1038/s41586-022-05269-w, http://dx.doi.org/10.1038/s41586-022-05269-w

Ahrer E.-M., et al., 2023, Early Release Science of the exoplanet WASP-39b with JWST NIRCam, doi:10.1038/s41586-022-05590-4, http://dx.doi.org/10.1038/s41586-022-05590-4

Amundsen D. S., et al., 2016, The UK Met Office global circulation model with a sophisticated radiation scheme applied to the hot Jupiter HD 209458b (arXiv:1608.08593), doi:10.1051/0004-6361/201629183

Azevedo J., et al., 2022, Detection of barium in the atmospheres of the ultra-hot Jupiters WASP-76b and WASP-121b using ESPRESSO, doi:10.1051/0004-6361/202243800

Baliunas S. L., Henry G. W., Donahue R. A., Fekel F. C., Soon W. H., 1997, Properties of Sun-like Stars with Planets: ρ^1 Cancri, τ Bootis, and υ Andromedae, doi:10.1086/310442

Barstow J. K., Heng K., 2020, Outstanding Challenges of Exoplanet Atmospheric Retrievals, doi:10.1007/s11214-020-00666-x, http://dx.doi.org/10.1007/s11214-020-00666-x

Barstow J. K., Aigrain S., Irwin P. G. J., Sing D. K., 2017, A Consistent Retrieval Analysis of 10 Hot Jupiters Observed in Transmission (arXiv:1610.01841), doi:10.3847/1538-4357/834/1/50

Barton E. J., Yurchenko S. N., Tennyson J., 2013, ExoMol line lists – II. The ro-vibrational spectrum of SiO (https://academic.oup.com/mnras/article-pdf/434/2/1469/18497122/stt1105.pdf), doi:10.1093/mnras/stt1105, https://doi.org/10.1093/mnras/stt1105

Bell T. J., et al., 2023, Methane Throughout the Atmosphere of the Warm Exoplanet WASP-80b (arXiv:2309.04042), https://arxiv.org/abs/2309.04042

Ben-Yami M., Madhusudhan N., Cabot S., Constantinou S., Piette A. A. A., Gandhi S., Welbanks L., 2020, Neutral Cr and V in the Atmosphere of Ultra-hot Jupiter WASP-121 b, doi:10.3847/2041-8213/ab94aa

Birkby J. L., de Kok R. J., Brogi M., de Mooij E. J. W., Schwarz H., Albrecht S., Snellen I. A. G., 2013, Detection of water absorption in the day side atmosphere of HD 189733 b using ground-based high-resolution spectroscopy at 3.2 m, doi:10.1093/mnrasl/slt107, http://dx.doi.org/10.1093/mnrasl/slt107

Bohn A. J., et al., 2020, The Young Suns Exoplanet Survey: Detection of a wide-orbit planetary-mass companion to a solar-type Sco-Cen member (arXiv:1912.04284), doi:10.1093/mnras/stz3462

Borsato N., Hoeijmakers H. J., Prinoth B., Thorsbro B., Forsberg R., Kitzmann D., Jones K., Heng K., 2023, The Mantis Network. III. Expanding the limits of chemical searches within ultra-hot Jupiters: New detections of Ca I, VI, Ti I, Cr I, Ni I, Sr II, Ba II, and Tb II in KELT-9 b, doi:10.1051/0004-6361/202245121

Brogi M., Line M. R., 2019, Retrieving Temperatures and Abundances of Exoplanet Atmospheres with High-resolution Cross-correlation Spectroscopy, doi:10.3847/1538-3881/aaffd3, http://dx.doi.org/10.3847/1538-3881/aaffd3

Brogi M., de Kok R. J., Albrecht S., Snellen I. A. G., Birkby J. L., Schwarz H., 2016, Rotation and Winds of Exoplanet HD 189733 b Measured with High-dispersion Transmission Spectroscopy (arXiv:1512.05175), doi:10.3847/0004-637X/817/2/106

Brown T. M., 2001, Transmission Spectra as Diagnostics of Extrasolar Giant Planet Atmospheres (arXiv:astro-ph/0101307), doi:10.1086/320950

Brown T. M., Charbonneau D., Gilliland R. L., Noyes R. W., Burrows A., 2001, Hubble Space Telescope Time-Series Photometry of the Transiting Planet of HD 209458 (arXiv:astro-ph/0101336), doi:10.1086/320580

Cabot S. H. C., Madhusudhan N., Hawker G. A., Gandhi S., 2018, On the robustness of analysis techniques for molecular detections using high-resolution exoplanet spectroscopy (https://academic.oup.com/mnras/article-pdf/482/4/4422/26779174/sty2994.pdf), doi:10.1093/mnras/sty2994, https://doi.org/10.1093/mnras/sty2994

Carter A. L., et al., 2020, Detection of Na, K, and H2O in the hazy atmosphere of WASP-6b, doi:10.1093/mnras/staa1078, http://dx.doi.org/10.1093/mnras/staa1078

Cauley P. W., Kuckein C., Redfield S., Shkolnik E. L., Denker C., Llama J., Verma M., 2018, The Effects of Stellar Activity on Optical High-resolution Exoplanet Transmission Spectra (arXiv:1808.09558), doi:10.3847/1538-3881/aaddf9

Charbonneau D., Brown T. M., Noyes R. W., Gilliland R. L., 2002, Detection of an Extrasolar Planet Atmosphere (arXiv:astro-ph/0111544), doi:10.1086/338770

Charbonneau D., Knutson H. A., Barman T., Allen L. E., Mayor M., Megeath S. T., Queloz D., Udry S., 2008, The Broadband Infrared Emission Spectrum of the Exoplanet HD 189733b (arXiv:0802.0845), doi:10.1086/591635

Chauvin G., et al., 2017, Discovery of a warm, dusty giant planet around HIP 65426 (arXiv:1707.01413), doi:10.1051/0004-6361/201731152

Cho J. Y. K., Polichtchouk I., Thrastarson H. T., 2015, Sensitivity and variability redux in hot-Jupiter flow simulations, doi:10.1093/mnras/stv1947

Cont D., et al., 2021, Silicon in the dayside atmospheres of two ultra-hot Jupiters, doi:10.1051/0004-6361/202142776

Coulombe L.-P., et al., 2023, A broadband thermal emission spectrum of the ultra-hot Jupiter WASP-18b, doi:10.1038/s41586-023-06230-1, http://dx.doi.org/10.1038/s41586-023-06230-1

Coursimault F., Motret O., Viladrosa R., Pouvesle J.-M., 2003, Mesure de la concentration absolue de SiO par spectroscopie d'absorption UV, doi:10.1051/jp4:20030613, https://hal.science/hal-02179060

Crossfield I. J. M., Kreidberg L., 2017, Trends in Atmospheric Properties of Neptune-size Exoplanets (arXiv:1708.00016), doi:10.3847/1538-3881/aa9279

Damasceno Y. C., et al., 2024, The atmospheric composition of the ultra-hot Jupiter WASP-178 b observed with ESPRESSO (arXiv:2406.08348), doi:10.1051/0004-6361/202450119

Dawson R. I., Johnson J. A., 2018, Origins of Hot Jupiters, doi:10.1146/annurev-astro-081817-051853

Deming D., et al., 2013, Infrared Transmission Spectroscopy of the Exoplanets HD 209458b and XO-1b Using the Wide Field Camera-3 on the Hubble Space Telescope (arXiv:1302.1141), doi:10.1088/0004-637X/774/2/95

Diamond-Lowe H., Stevenson K. B., Bean J. L., Line M. R., Fortney J. J., 2014, NEW ANALYSIS INDICATES NO THERMAL INVERSION IN THE ATMOSPHERE OF HD 209458b, doi:10.1088/0004-637X/796/1/66, https://dx.doi.org/10.1088/0004-637X/796/1/66

Désert J.-M., Vidal-Madjar A., Lecavelier des Etangs A., Sing D., Ehrenreich D., Hébrard G., Ferlet R., 2008, TiO and VO broad band absorption features in the optical spectrum of the atmosphere of the hot-Jupiter HD 209458b, doi:10.1051/0004-6361:200810355, http://dx.doi.org/10.1051/0004-6361:200810355

Edwards B., Mugnai L., Tinetti G., Pascale E., Sarkar S., 2019, An Updated Study of Potential Targets for Ariel (arXiv:1905.04959), doi:10.3847/1538-3881/ab1cb9

Ehrenreich D., et al., 2015, A giant comet-like cloud of hydrogen escaping the warm Neptune-mass exoplanet GJ 436b (arXiv:1506.07541), doi:10.1038/nature14501

Ehrenreich D., et al., 2020, Nightside condensation of iron in an ultrahot giant exoplanet, doi:10.1038/s41586-020-2107-1, http://dx.doi.org/10.1038/s41586-020-2107-1

Evans T. M., et al., 2016, Detection of H_2O and Evidence for TiO/VO in an Ultra-hot Exoplanet Atmosphere (arXiv:1604.02310), doi:10.3847/2041-8205/822/1/L4

Evans T. M., et al., 2018, An Optical Transmission Spectrum for the Ultra-hot Jupiter WASP-121b Measured with the Hubble Space Telescope (arXiv:1810.10969), doi:10.3847/1538-3881/aaebff

Feinstein A. D., et al., 2023, Early Release Science of the exoplanet WASP-39b with JWST NIRISS (arXiv:2211.10493), doi:10.1038/s41586-022-05674-1

Fortney J. J., Lodders K., Marley M. S., Freedman R. S., 2008, A Unified Theory for the Atmospheres of the Hot and Very Hot Jupiters: Two Classes of Irradiated Atmospheres (arXiv:0710.2558), doi:10.1086/528370

Fortney J. J., Dawson R. I., Komacek T. D., 2021, Hot Jupiters: Origins, Structure, Atmospheres (https://agupubs.onlinelibrary.wiley.com/doi/pdf/10.1029/2020JE006629), doi:https://doi.org/10.1029/2020JE006629, https://agupubs.onlinelibrary.wiley.com/doi/abs/10.1029/2020JE006629

Fossati L., et al., 2010, Metals in the exosphere of the highly irradiated planet wasp-12b, doi:10.1088/2041-8205/714/2/l222

Fossati L., Young M. E., Shulyak D., Koskinen T., Huang C., Cubillos P. E., France K., Sreejith A. G., 2021, Non-local thermodynamic equilibrium effects determine the upper atmospheric temperature structure of the ultra-hot Jupiter KELT-9b (arXiv:2106.11263), doi:10.1051/0004-6361/202140813

France K., et al., 2013, The Ultraviolet Radiation Environment around M dwarf Exoplanet Host Stars (arXiv:1212.4833), doi:10.1088/0004-637X/763/2/149

Fu G., et al., 2021, The Hubble PanCET Program: Transit and Eclipse Spectroscopy of the Strongly Irradiated Giant Exoplanet WASP-76b (arXiv:2005.02568), doi:10.3847/1538-3881/ac1200

Fu G., et al., 2024, Hydrogen sulfide and metal-enriched atmosphere for a Jupiter-mass exoplanet (arXiv:2407.06163), https://arxiv.org/abs/2407.06163

Gandhi S., Madhusudhan N., 2019, New avenues for thermal inversions in atmospheres of hot Jupiters (https://academic.oup.com/mnras/article-pdf/485/4/5817/28271799/stz751.pdf), doi:10.1093/mnras/stz751, https://doi.org/10.1093/mnras/stz751

Gao P., Benneke B., 2018, Microphysics of KCl and ZnS Clouds on GJ 1214 b (arXiv:1807.04924), doi:10.3847/1538-4357/aad461

Gao P., et al., 2020, Aerosol composition of hot giant exoplanets dominated by silicates and hydrocarbon hazes (arXiv:2005.11939), doi:10.1038/s41550-020-1114-3

Gao P., Wakeford H. R., Moran S. E., Parmentier V., 2021, Aerosols in Exoplanet Atmospheres (https://agupubs.onlinelibrary.wiley.com/doi/pdf/10.1029/2020JE006655), doi:https://doi.org/10.1029/2020JE006655, https://agupubs.onlinelibrary.wiley.com/doi/abs/10.1029/2020JE006655

Gaudi B. S., et al., 2017, A giant planet undergoing extreme-ultraviolet irradiation by its hot massive-star host (arXiv:1706.06723), doi:10.1038/nature22392

Grant D., et al., 2023, Detection of Carbon Monoxide's 4.6 Micron Fundamental Band Structure in WASP-39b's Atmosphere with JWST NIRSpec G395H

Green J. C., et al., 2012, The Cosmic Origins Spectrograph (arXiv:1110.0462), doi:10.1088/0004-637X/744/1/6010.1086/141956

Greene T. P., Line M. R., Montero C., Fortney J. J., Lustig-Yaeger J., Luther K., 2016, Characterizing Transiting Exoplanet Atmospheres with JWST (arXiv:1511.05528), doi:10.3847/0004-637X/817/1/17

Gressier A., 2022, Theses, Université Paris-Saclay, https://theses.hal.science/tel-04029295

Hellier C., et al., 2019, WASP-South hot Jupiters: WASP-178b, WASP-184b, WASP-185b, and WASP-192b (arXiv:1907.11667), doi:10.1093/mnras/stz2713

Helling C., Casewell S., 2014, Atmospheres of brown dwarfs, doi:10.1007/s00159-014-0080-0, http://dx.doi.org/10.1007/s00159-014-0080-0

Helling C., Gourbin P., Woitke P., Parmentier V., 2019, Sparkling nights and very hot days on WASP-18b: the formation of clouds and the emergence of an ionosphere (arXiv:1901.08640), doi:10.1051/0004-6361/201834085

Helling C., et al., 2021, Cloud property trends in hot and ultra-hot giant gas planets (WASP-43b, WASP-103b, WASP-121b, HAT-P-7b, and WASP-18b)

Heng K., 2017, Exoplanetary Atmospheres: Theoretical Concepts and Foundations

Heng K., Menou K., Phillipps P. J., 2011, Atmospheric circulation of tidally locked exoplanets: a suite of benchmark tests for dynamical solvers (arXiv:1010.1257), doi:10.1111/j.1365-2966.2011.18315.x

Hoeijmakers J., et al., 2018, Atomic iron and titanium in the atmosphere of the exoplanet KELT-9b, doi:10.1038/s41586-018-0401-y

Hoeijmakers H. J., et al., 2019, A spectral survey of the dayside atmosphere of KELT-9b with HARPS-N, doi:10.1051/0004-6361/201935329

Hubeny I., Mihalas D., 2014, Theory of Stellar Atmospheres

Hubeny I., Burrows A., Sudarsky D., 2003, A Possible Bifurcation in Atmospheres of Strongly Irradiated Stars and Planets (arXiv:astro-ph/0305349), doi:10.1086/377080

Huitson C. M., et al., 2013, An HST optical-to-near-IR transmission spectrum of the hot Jupiter WASP-19b: detection of atmospheric water and likely absence of TiO, doi:10.1093/mnras/stt1243, http://dx.doi.org/10.1093/mnras/stt1243

Johns M., et al., 2012, in Stepp L. M., Gilmozzi R., Hall H. J., eds, Society of Photo-Optical Instrumentation Engineers (SPIE) Conference Series Vol. 8444, Ground-based and Airborne Telescopes IV. p. 84441H, doi:10.1117/12.926716

Johnson M. C., et al., 2022, The PEPSI Exoplanet Transit Survey (PETS). II. A Deep Search for Thermal Inversion Agents in KELT-20 b/MASCARA-2 b with Emission and Transmission Spectroscopy, doi:10.3847/1538-3881/acb7e2

Kirkpatrick J. D., 2005, New Spectral Types L and T, doi:10.1146/annurev.astro.42.053102.134017

Kitzmann D., et al., 2018, The Peculiar Atmospheric Chemistry of KELT-9b (arXiv:1804.07137), doi:10.3847/1538-4357/aace5a

Kitzmann D., Heng K., Oreshenko M., Grimm S. L., Apai D., Bowler B. P., Burgasser A. J., Marley M. S., 2020, Helios-r2: A New Bayesian, Open-source Retrieval Model for Brown Dwarfs and Exoplanet Atmospheres (arXiv:1910.01070), doi:10.3847/1538-4357/ab6d71

Knutson H. A., et al., 2007, A map of the day–night contrast of the extrasolar planet HD 189733b, doi:10.1038/nature05782, http://dx.doi.org/10.1038/nature05782

Knutson H. A., Charbonneau D., Allen L. E., Burrows A., Megeath S. T., 2008, The 3.6-8.0 μm Broadband Emission Spectrum of HD 209458b: Evidence for an Atmospheric Temperature Inversion (arXiv:0709.3984), doi:10.1086/523894

Komacek T. D., Showman A. P., Tan X., 2017, Atmospheric Circulation of Hot Jupiters: Dayside–Nightside Temperature Differences. II. Comparison with Observations, doi:10.3847/1538-4357/835/2/198, http://dx.doi.org/10.3847/1538-4357/835/2/198

Kreidberg L., 2015, batman: BAsic Transit Model cAlculatioN in Python (arXiv:1507.08285), doi:10.1086/683602

Kreidberg L., 2018, Exoplanet Atmosphere Measurements from Transmission Spectroscopy and Other Planet Star Combined Light Observations. Springer International Publishing, p. 2083–2105, doi:10.1007/978-3-319-55333-7_100, http://dx.doi.org/10.1007/978-3-319-55333-7_100

Kreidberg L., et al., 2014a, Clouds in the atmosphere of the super-Earth exoplanet GJ1214b (arXiv:1401.0022), doi:10.1038/nature12888

Kreidberg L., et al., 2014b, A PRECISE WATER ABUNDANCE MEASUREMENT FOR THE HOT JUPITER WASP-43b, doi:10.1088/2041-8205/793/2/l27, http://dx.doi.org/10.1088/2041-8205/793/2/L27

Kreidberg L., et al., 2015, A Detection of Water in the Transmission Spectrum of the Hot Jupiter WASP-12b and Implications for Its Atmospheric Composition (arXiv:1504.05586), doi:10.1088/0004-637X/814/1/66

Kurucz R. L., 2011, Including all the lines1This article is part of a Special Issue on the 10th International Colloquium on Atomic Spectra and Oscillator Strengths for Astrophysical and Laboratory Plasmas. (https://doi.org/10.1139/p10-104), doi:10.1139/p10-104, https://doi.org/10.1139/p10-104

Lagrange A. M., et al., 2010, A Giant Planet Imaged in the Disk of the Young Star β Pictoris (arXiv:1006.3314), doi:10.1126/science.1187187

Lavie B., et al., 2017, HELIOS–RETRIEVAL: An Open-source, Nested Sampling Atmospheric Retrieval Code; Application to the HR 8799 Exoplanets and Inferred Constraints for Planet Formation, doi:10.3847/1538-3881/aa7ed8, http://dx.doi.org/10.3847/1538-3881/aa7ed8

Lecavelier Des Etangs A., Vidal-Madjar A., Désert J. M., Sing D., 2008, Rayleigh scattering by H_2 in the extrasolar planet HD 209458b (arXiv:0805.0595), doi:10.1051/0004-6361:200809704

Lee E. K. H., Prinoth B., Kitzmann D., min Tsai S., Hoeijmakers J., Borsato N., Heng K., 2022, The Mantis Network II: Examining the 3D high-resolution observable properties of the UHJs WASP-121b and WASP-189b through GCM modelling, doi:10.1093/mnras/stac2246 10.1093/mnras/stac2246

Lendl M., Cubillos P. E., Hagelberg J., Müller A., Juvan I., Fossati L., 2017, Signs of strong Na and K absorption in the transmission spectrum of WASP-103b (arXiv:1708.05737), doi:10.1051/0004-6361/201731242

Lew B. W. P., et al., 2024, High-precision atmospheric characterization of a Y dwarf with JWST NIRSpec G395H spectroscopy: isotopologue, C/O ratio, metallicity, and the abundances of six molecular species (arXiv:2402.05900), https://arxiv.org/abs/2402.05900

Linsky J. L., Yang H., France K., Froning C. S., Green J. C., Stocke J. T., Osterman S. N., 2010, OBSERVATIONS OF MASS LOSS FROM THE TRANSITING EXOPLANET HD 209458b, doi:10.1088/0004-637x/717/2/1291, http://dx.doi.org/10.1088/0004-637X/717/2/1291

Lopez-Morales M., et al., 2019, Detecting Earth-like Biosignatures on Rocky Exoplanets around Nearby Stars with Ground-based Extremely Large Telescopes (arXiv:1903.09523), doi:10.48550/arXiv.1903.09523

Lothringer J., Barman T., Koskinen T., 2018, Extremely Irradiated Hot Jupiters: Non-oxide Inversions, H- Opacity, and Thermal Dissociation of Molecules, doi:10.3847/1538-4357/aadd9e

Lothringer J. D., Fu G., Sing D. K., Barman T. S., 2020, UV Exoplanet Transmission Spectral Features as Probes of Metals and Rainout, doi:10.3847/2041-8213/aba265, https://dx.doi.org/10.3847/2041-8213/aba265

Lothringer J. D., et al., 2021, UV Absorption by Silicate Cloud Precursors in Ultra-hot Jupiter WASP-178b, doi:10.21203/rs.3.rs-923439/v1, http://arxiv.org/abs/2204.03639

Lothringer J. D., et al., 2025, Refractory and Volatile Species in the UV-to-IR Transmission Spectrum of Ultra-hot Jupiter WASP-178b with HST and JWST (arXiv:2503.15472)

Louden T., Wheatley P. J., 2015, SPATIALLY RESOLVED EASTWARD WINDS AND ROTATION OF HD 189733b, doi:10.1088/2041-8205/814/2/l24, http://dx.doi.org/10.1088/2041-8205/814/2/L24

Madhusudhan N., 2012, C/O Ratio as a Dimension for Characterizing Exoplanetary Atmospheres (arXiv:1209.2412), doi:10.1088/0004-637X/758/1/36

Madhusudhan N., 2019, Exoplanetary Atmospheres: Key Insights, Challenges, and Prospects, doi:https://doi.org/10.1146/annurev-astro-081817-051846, https://www.annualreviews.org/content/journals/10.1146/annurev-astro-081817-051846

Madhusudhan N., Seager S., 2009, A Temperature and Abundance Retrieval Method for Exoplanet Atmospheres (arXiv:0910.1347), doi:10.1088/0004-637X/707/1/24

Marcy G. W., Butler R. P., 1998, Detection of Extrasolar Giant Planets, doi:10.1146/annurev.astro.36.1.57

Marcy G. W., Butler R. P., Vogt S. S., Fischer D., Lissauer J. J., 1998, A Planetary Companion to a Nearby M4 Dwarf, Gliese 876 (arXiv:astro-ph/9807307), doi:10.1086/311623

Markwardt C. B., 2009, Non-linear Least-squares Fitting in IDL with MPFIT (arXiv:0902.2850), doi:10.48550/arXiv.0902.2850

Marois C., Macintosh B., Barman T., Zuckerman B., Song I., Patience J., Lafrenière D., Doyon R., 2008, Direct Imaging of Multiple Planets Orbiting the Star HR 8799 (https://www.science.org/doi/pdf/10.1126/science.1166585), doi:10.1126/science.1166585, https://www.science.org/doi/abs/10.1126/science.1166585

Martínez R. R., et al., 2020, KELT-25 b and KELT-26 b: A Hot Jupiter and a Substellar Companion Transiting Young A Stars Observed by TESS*, doi:10.3847/1538-3881/ab9f2d, https://dx.doi.org/10.3847/1538-3881/ab9f2d

Mayor M., Queloz D., 1995, A Jupiter-mass companion to a solar-type star, doi:10.1038/378355a0

Mayor M., et al., 2003, Setting New Standards with HARPS

Meier R. R., 1991, Ultraviolet spectroscopy and remote sensing of the upper atmosphere, doi:10.1007/BF01206000

Mendonça J. M., Malik M., Demory B.-O., Heng K., 2018, Revisiting the Phase Curves of WASP-43b: Confronting Re-analyzed Spitzer Data with Cloudy Atmospheres (arXiv:1802.03047), doi:10.3847/1538-3881/aaaebc

Merritt S., et al., 2021, An inventory of atomic species in the atmosphere of WASP-121b using UVES high-resolution spectroscopy, doi:10.1093/mnras/stab1878

Mikal-Evans T., et al., 2019, An emission spectrum for WASP-121b measured across the 0.8–1.1 m wavelength range using the Hubble Space Telescope, doi:10.1093/mnras/stz1753, http://dx.doi.org/10.1093/mnras/stz1753

Mollière P., Snellen I. A. G., 2019, Detecting isotopologues in exoplanet atmospheres using ground-based high-dispersion spectroscopy, doi:10.1051/0004-6361/201834169, http://dx.doi.org/10.1051/0004-6361/201834169

Mollière P., Wardenier J. P., van Boekel R., Henning T., Molaverdikhani K., Snellen I. A. G., 2019, petitRADTRANS: A Python radiative transfer package for exoplanet characterization and retrieval, doi:10.1051/0004-6361/201935470, http://dx.doi.org/10.1051/0004-6361/201935470

Mollière P., et al., 2022, Interpreting the Atmospheric Composition of Exoplanets: Sensitivity to Planet Formation Assumptions, doi:10.3847/1538-4357/ac6a56

Moses J. I., Madhusudhan N., Visscher C., Freedman R. S., 2012, CHEMICAL CONSEQUENCES OF THE C/O RATIO ON HOT JUPITERS: EXAMPLES FROM WASP-12b, CoRoT-2b, XO-1b, AND HD 189733b, doi:10.1088/0004-637x/763/1/25, http://dx.doi.org/10.1088/0004-637X/763/1/25

Nikolov N., et al., 2018, An absolute sodium abundance for a cloud-free 'hot Saturn'exoplanet

Nugroho S. K., Kawahara H., Masuda K., Hirano T., Kotani T., Tajitsu A., 2017, High-resolution Spectroscopic Detection of TiO and a Stratosphere in the Day-side of WASP-33b, doi:10.3847/1538-3881/aa9433, http://dx.doi.org/10.3847/1538-3881/aa9433

Nugroho S. K., Gibson N., de Mooij E. D., Watson C., Kawahara H., Merritt S., 2020, Searching for thermal inversion agents in the transmission spectrum of KELT-20b/MASCARA-2b: detection of neutral iron and ionised calcium H&K lines, doi:10.1093/MNRAS/STAA1459

Öberg K. I., Murray-Clay R., Bergin E. A., 2011, The Effects of Snowlines on C/O in Planetary Atmospheres (arXiv:1110.5567), doi:10.1088/2041-8205/743/1/L16

Park C., Arnold J., 1978, A shock-tube determination of the SiO(A1-X1+) transition moment, doi:https://doi.org/10.1016/0022-4073(78)90037-7, https://www.sciencedirect.com/science/article/pii/0022407378900377

Parmentier, Vivien et al., 2018, From thermal dissociation to condensation in the atmospheres of ultra hot Jupiters: WASP-121b in context, doi:10.1051/0004-6361/201833059, https://doi.org/10.1051/0004-6361/201833059

Parmentier V., Fortney J. J., Showman A. P., Morley C., Marley M. S., 2016, Transitions in the Cloud Composition of Hot Jupiters (arXiv:1602.03088), doi:10.3847/0004-637X/828/1/22

Parmentier V., Showman A. P., Fortney J. J., 2021, The cloudy shape of hot Jupiter thermal phase curves (arXiv:2010.06934), doi:10.1093/mnras/staa3418

Pascale E., et al., 2018, in Lystrup M., MacEwen H. A., Fazio G. G., Batalha N., Siegler N., Tong E. C., eds, Society of Photo-Optical Instrumentation Engineers (SPIE) Conference Series Vol. 10698, Space Telescopes and Instrumentation 2018: Optical, Infrared, and Millimeter Wave. p. 106980H, doi:10.1117/12.2311838

Pepe F., et al., 2021, ESPRESSO at VLT. On-sky performance and first results (arXiv:2010.00316), doi:10.1051/0004-6361/202038306

Pepper J., et al., 2007, The Kilodegree Extremely Little Telescope (KELT): A Small Robotic Telescope for Large-Area Synoptic Surveys (arXiv:0704.0460), doi:10.1086/521836

Pinhas A., Madhusudhan N., Gandhi S., MacDonald R., 2019, H_2O abundances and cloud properties in ten hot giant exoplanets (arXiv:1811.00011), doi:10.1093/mnras/sty2544

Pollacco D. L., et al., 2006, The WASP Project and the SuperWASP Cameras (arXiv:astro-ph/0608454), doi:10.1086/508556

Pont F., Sing D. K., Gibson N. P., Aigrain S., Henry G., Husnoo N., 2013, The prevalence of dust on the exoplanet HD 189733b from Hubble and Spitzer observations (arXiv:1210.4163), doi:10.1093/mnras/stt651

Powell D., Zhang X., Gao P., Parmentier V., 2018, Formation of Silicate and Titanium Clouds on Hot Jupiters, doi:10.3847/1538-4357/aac215, https://dx.doi.org/10.3847/1538-4357/aac215

Powell D., Louden T., Kreidberg L., Zhang X., Gao P., Parmentier V., 2019, Transit Signatures of Inhomogeneous Clouds on Hot Jupiters: Insights from Microphysical Cloud Modeling, doi:10.3847/1538-4357/ab55d9, https://dx.doi.org/10.3847/1538-4357/ab55d9

Quanz S. P., Amara A., Meyer M. R., Girard J. H., Kenworthy M. A., Kasper M., 2015, Astrophys. J., 807, 64

Rauscher E., Kempton E. M. R., 2014, THE ATMOSPHERIC CIRCULATION AND OBSERVABLE PROPERTIES OF NON-SYNCHRONOUSLY ROTATING HOT JUPITERS, doi:10.1088/0004-637x/790/1/79, http://dx.doi.org/10.1088/0004-637X/790/1/79

Rauscher E., Menou K., 2010, Three-dimensional Modeling of Hot Jupiter Atmospheric Flows (arXiv:0907.2692), doi:10.1088/0004-637X/714/2/1334

Rauscher E., Menou K., 2012, The Role of Drag in the Energetics of Strongly Forced Exoplanet Atmospheres (arXiv:1105.2321), doi:10.1088/0004-637X/745/1/78

Redfield S., Endl M., Cochran W. D., Koesterke L., 2008, Sodium Absorption from the Exoplanetary Atmosphere of HD 189733b Detected in the Optical Transmission Spectrum (arXiv:0712.0761), doi:10.1086/527475

Roman M. T., Kempton E. M. R., Rauscher E., Harada C. K., Bean J. L., Stevenson K. B., 2021, Clouds in Three-dimensional Models of Hot Jupiters over a Wide Range of Temperatures. I. Thermal Structures and Broadband Phase-curve Predictions (arXiv:2010.06936), doi:10.3847/1538-4357/abd549

Rukdee S., Ben-Ami S., Szentgyorgyi A., López-Morales M., Charbonneau D., García-Mejía J., 2020, Characterization of a multi-etalon array for ultra-high resolution spectroscopy (arXiv:2012.04007), https://arxiv.org/abs/2012.04007

Rustamkulov Z., et al., 2023, Early Release Science of the exoplanet WASP-39b with JWST NIRSpec PRISM, doi:10.1038/s41586-022-05677-y, http://dx.doi.org/10.1038/s41586-022-05677-y

Saur J., Willmes C., Fischer C., Wennmacher A., Roth L., Youngblood A., Strobel D. F., Reiners A., 2021, Brown dwarfs as ideal candidates for detecting UV aurora outside the Solar System: Hubble Space Telescope observations of 2MASS J1237+6526 (arXiv:2109.00827), doi:10.1051/0004-6361/202040230

Schwab C., et al., 2016, in Evans C. J., Simard L., Takami H., eds, Society of Photo-Optical Instrumentation Engineers (SPIE) Conference Series Vol. 9908, Ground-based and Airborne Instrumentation for Astronomy VI. p. 99087H, doi:10.1117/12.2234411

Schwartz J. C., Kashner Z., Jovmir D., Cowan N. B., 2017, Phase Offsets and the Energy Budgets of Hot Jupiters (arXiv:1707.05790), doi:10.3847/1538-4357/aa9567

Schwarz H., Brogi M., de Kok R., Birkby J., Snellen I., 2015, Evidence against a strong thermal inversion in HD 209458b from high-dispersion spectroscopy (arXiv:1502.04713), doi:10.1051/0004-6361/201425170

Seager S., Sasselov D. D., 2000, Theoretical Transmission Spectra during Extrasolar Giant Planet Transits, doi:10.1086/309088, http://dx.doi.org/10.1086/309088

Sharp C. M., Burrows A., 2007, Atomic and Molecular Opacities for Brown Dwarf and Giant Planet Atmospheres (arXiv:astro-ph/0607211), doi:10.1086/508708

Showman A. P., Guillot T., 2002, Atmospheric circulation and tides of “51 Pegasus b-like” planets (arXiv:astro-ph/0202236), doi:10.1051/0004-6361:20020101

Showman A. P., Fortney J. J., Lian Y., Marley M. S., Freedman R. S., Knutson H. A., Charbonneau D., 2009, Atmospheric Circulation of Hot Jupiters: Coupled Radiative-Dynamical General Circulation Model Simulations of HD 189733b and HD 209458b (arXiv:0809.2089), doi:10.1088/0004-637X/699/1/564

Showman A. P., Tan X., Parmentier V., 2020, Atmospheric Dynamics of Hot Giant Planets and Brown Dwarfs (arXiv:2007.15363), doi:10.1007/s11214-020-00758-8

Silva T. A., et al., 2022, Detection of barium in the atmospheres of the ultra-hot gas giants WASP-76b and WASP-121b, doi:10.1051/0004-6361/202244489

Sing D. K., et al., 2011a, Hubble Space Telescope transmission spectroscopy of the exoplanet HD 189733b: high-altitude atmospheric haze in the optical and near-ultraviolet with STIS (arXiv:1103.0026), doi:10.1111/j.1365-2966.2011.19142.x

Sing D. K., et al., 2011b, Gran Telescopio Canarias OSIRIS transiting exoplanet atmospheric survey: detection of potassium in XO-2b from narrowband spectrophotometry (arXiv:1008.4795), doi:10.1051/0004-6361/201015579

Sing D. K., et al., 2013, HST hot-Jupiter transmission spectral survey: evidence for aerosols and lack of TiO in the atmosphere of WASP-12b (arXiv:1309.5261), doi:10.1093/mnras/stt1782

Sing D. K., et al., 2015, A continuum from clear to cloudy hot-Jupiter exoplanets without primordial water depletion, doi:10.1038/nature16068, http://dx.doi.org/10.1038/nature16068

Sing D., et al., 2019, The Hubble Space Telescope PanCET Program: Exospheric Mg ii and Fe ii in the Near-ultraviolet Transmission Spectrum of WASP-121b Using Jitter Decorrelation, doi:10.3847/1538-3881/ab2986

Skidmore W., TMT International Science Development Teams Science Advisory Committee T., 2015, Thirty Meter Telescope Detailed Science Case: 2015 (arXiv:1505.01195), doi:10.1088/1674-4527/15/12/001

Snellen I. A. G., Albrecht S., de Mooij E. J. W., Le Poole R. S., 2008, Ground-based detection of sodium in the transmission spectrum of exoplanet HD 209458b, doi:10.1051/0004-6361:200809762, http://dx.doi.org/10.1051/0004-6361:200809762

Snellen I., Kok R., Mooij E., Albrecht S., 2010, The orbital motion, absolute mass and high-altitude winds of exoplanet hd 209458b, doi:10.1038/nature09111

Snellen I., et al., 2015, Combining high-dispersion spectroscopy with high contrast imaging: Probing rocky planets around our nearest neighbors (arXiv:1503.01136), doi:10.1051/0004-6361/201425018

Stangret M., Casasayas-Barris N., Pallé E., Yan F., S'anchez-L'opez A., López-Puertas M., 2020, Detection of FeI and FeII in the atmosphere of MASCARA-2b using a cross-correlation method, doi:10.1051/0004-6361/202037541

Stevenson K. B., Bean J. L., Madhusudhan N., Harrington J., 2014, Deciphering the Atmospheric Composition of WASP-12b: A Comprehensive Analysis of its Dayside Emission (arXiv:1406.7567), doi:10.1088/0004-637X/791/1/36

Stevenson K. B., Bean J. L., Seifahrt A., Gilbert G. J., Line M. R., Désert J.-M., Fortney J. J., 2016, A SEARCH FOR WATER IN THE ATMOSPHERE OF HAT-P-26b USING LDSS-3C, doi:10.3847/0004-637x/817/2/141, http://dx.doi.org/10.3847/0004-637X/817/2/141

Swain M. R., Vasisht G., Tinetti G., 2008, Methane present in an extrasolar planet atmosphere (arXiv:0802.1030), doi:10.48550/arXiv.0802.1030

Tamai R., Cirasuolo M., González J. C., Koehler B., Tuti M., 2016, in Hall H. J., Gilmozzi R., Marshall H. K., eds, Society of Photo-Optical Instrumentation Engineers (SPIE) Conference Series Vol. 9906, Ground-based and Airborne Telescopes VI. p. 99060W, doi:10.1117/12.2232690

Tinetti G., et al., 2007, Water vapour in the atmosphere of a transiting extrasolar planet, doi:10.1038/nature06002

Tinetti G., et al., 2018, A chemical survey of exoplanets with ARIEL, doi:10.1007/s10686-018-9598-x

Todorov K., Deming D., Harrington J., Stevenson K. B., Bowman W. C., Nymeyer S., Fortney J. J., Bakos G. A., 2010, Spitzer IRAC Secondary Eclipse Photometry of the Transiting Extrasolar Planet HAT-P-1b (arXiv:0911.2218), doi:10.1088/0004-637X/708/1/498

Tsai S.-M., et al., 2023, Photochemically produced SO2 in the atmosphere of WASP-39b, doi:10.1038/s41586-023-05902-2, http://dx.doi.org/10.1038/s41586-023-05902-2

Visscher C., Lodders K., Fegley Jr. B., 2010, Atmospheric Chemistry in Giant Planets, Brown Dwarfs, and Low-mass Dwarf Stars. III. Iron, Magnesium, and Silicon (arXiv:1001.3639), doi:10.1088/0004-637X/716/2/1060

Wakeford H. R., Sing D. K., Evans T., Deming D., Mandell A., 2016, Marginalizing Instrument Systematics in HST WFC3 Transit Light Curves (arXiv:1601.02587), doi:10.3847/0004-637X/819/1/10

Wakeford H. R., et al., 2018, The Complete Transmission Spectrum of WASP-39b with a Precise Water Constraint (arXiv:1711.10529), doi:10.3847/1538-3881/aa9e4e

Waldmann I. P., Tinetti G., Rocchetto M., Barton E. J., Yurchenko S. N., Tennyson J., 2015, TAU-REX I: A NEXT GENERATION RETRIEVAL CODE FOR EXOPLANETARY ATMOSPHERES, doi:10.1088/0004-637x/802/2/107, http://dx.doi.org/10.1088/0004-637X/802/2/107

Welch B. L., 1947, THE GENERALIZATION OF 'STUDENT'S' PROBLEM WHEN SEVERAL DIFFERENT POPULATION VARLANCES ARE INVOLVED, doi:10.1093/biomet/34.1-2.28, https://doi.org/10.1093/biomet/34.1-2.28

Woodgate B. E., et al., 1998, The Space Telescope Imaging Spectrograph Design, doi:10.1086/316243

Wyttenbach A., Ehrenreich D., Lovis C., Udry S., Pepe F., 2015, Spectrally resolved detection of sodium in the atmosphere of HD 189733b with the HARPS spectrograph (arXiv:1503.05581), doi:10.1051/0004-6361/201525729

Wyttenbach A., et al., 2017, Hot Exoplanet Atmospheres Resolved with Transit Spectroscopy (HEARTS): I. Detection of hot neutral sodium at high altitudes on WASP-49b, doi:10.1051/0004-6361/201630063, http://dx.doi.org/10.1051/0004-6361/201630063

Yan F., et al., 2022, Detection of CO emission lines in the dayside atmospheres of WASP-33b and WASP-189b with GIANO (arXiv:2204.10158), doi:10.1051/0004-6361/202243503

Yang Y., G. C., Wang S., F. Y., 2023, High-resolution Transmission Spectroscopy of Ultrahot Jupiter WASP–33b with NEID, doi:10.3847/1538-3881/ad10a3

Yurchenko S. N., Al-Refaie A. F., Tennyson J., 2018, EXOCROSS: a general program for generating spectra from molecular line lists, doi:10.1051/0004-6361/201732531, http://dx.doi.org/10.1051/0004-6361/201732531

Yurchenko S. N., et al., 2021, ExoMol line lists – XLIV. Infrared and ultraviolet line list for silicon monoxide (28Si16O), doi:10.1093/mnras/stab3267, http://dx.doi.org/10.1093/mnras/stab3267

van Sluijs L., et al., 2023, Carbon monoxide emission lines reveal an inverted atmosphere in the ultra hot Jupiter WASP-33 b consistent with an eastward hot spot, doi:10.1093/mnras/stad1103, http://dx.doi.org/10.1093/mnras/stad1103

von Essen, C. Mallonn, M. Hermansen, S. Nixon, M. C. Madhusudhan, N. Kjeldsen, H. Tautvaišienė, G. 2020, HST/STIS transmission spectrum of the ultra-hot Jupiter WASP-76 b confirms the presence of sodium in its atmosphere, doi:10.1051/0004-6361/201937169, https://doi.org/10.1051/0004-6361/201937169